

Carbon nitride in peroxide-coupled photocatalysis for aqueous organic pollutants destruction: Engineered active sites and electron transfer regimes

Peihan Chen^a, Menghan Zhou^a, Ya Liu^b, Bofeng Li^a, Chunmao Chen^{a,*}, Xiaoguang Duan^{b,*}, Yuxian Wang^{a,*}

^a State Key Laboratory of Heavy Oil Processing, State Key Laboratory of Petroleum Pollution Control, China University of Petroleum-Beijing, Beijing 102249, China

^b School of Chemical Engineering, The University of Adelaide, Adelaide, SA 5005, Australia

ARTICLE INFO

Keywords:

Peroxides
Photocatalysis
Carbon nitride
Electron transfer
Wastewater treatment

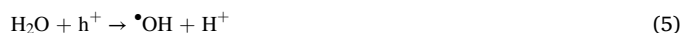
ABSTRACT

Heterogeneous Fenton-like photocatalytic reactions are potent in environmental remediations because of the synergisms of highly active photoelectrons for sustainable activation of peroxides. Such high energy electrons can stimulate the breakage of the peroxy bond (O-O) to evolve reactive oxygen species (ROS) and improve the photocatalytic efficiency. Graphitic carbon nitride (g-C₃N₄) has received broad research attention in wastewater decontamination owing to its high intrinsic photocatalytic activity and strong interactions with peroxides. This review summarizes the recent research progress of the applications of g-C₃N₄-based catalysts in peroxide-coupled photocatalytic reactions. Photo-induced electron transfer regimes for peroxides activation towards ROS generation are scrutinized and categorized. And the engineered strategies to optimize the physio-chemical properties and electronic states of g-C₃N₄ to efficiently drive photo-Fenton catalysis are outlined. Challenges and future research opportunities are also proposed for the photocatalysts design, mechanisms exploration, and practical implementation possibilities.

1. Introduction

The increasing scarcity of fresh water inducing by incontinently usage and the unbridled pollution imposes great threats to construct the sustainable future of human beings [1]. Apart from limiting water usage, recovering fresh water by *in situ* remediating and advanced purification technologies have been implemented to alleviate this crisis [2,3]. Traditional remediation methods such as physical adsorption, chemical oxidation, and biodegradation suffer from problems of low treatment efficiency, high energy consumption, and large investment in infrastructure. As a potent branch of advanced oxidation processes (AOPs), photocatalysis relying on photo-excited holes and electrons from the semiconductors can degrade the aqueous pollutants in an effective and sustainable manner [4-8]. Depending on their redox capacities, the oxidative photo-excited valence band holes (VB-h⁺) can activate water molecules to form hydroxyl radical (•OH) or directly oxidize the pollutants, while the reductive photo-excited conduction band electrons (CB-e⁻) can evolve into superoxide radicals (O₂^{•-}), •OH, and other reactive oxygen species via electron transfer processes (Eqs. 1-5) [9,10]. Meanwhile, the photo-excited electrons can also reduce the toxic

oxidative cations such as Cr⁶⁺ and As^{5+/3+} [11]. These features endow photocatalytic process with broader applications possibilities such as in clean energy production and high-value chemicals generation besides environmental remediations [12-14].



To exploit the inexhaustible solar energy and improve the quantum yield, research attentions have pivoted from ultraviolet-activated photocatalysis to solar/visible light-activated photocatalysis because of the low proportion of ultraviolet light in the solar spectrum (~4%) [15]. Additionally, LED lamps have replaced conventional halide lamps to further decrease energy loss [16]. Although productive efforts have been devoted to enhancing the efficiency of photocatalysis in aqueous

* Corresponding authors.

E-mail addresses: c.chen@cup.edu.cn (C. Chen), xiaoguang.duan@adelaide.edu.au (X. Duan), yuxian.wang@cup.edu.cn (Y. Wang).

<https://doi.org/10.1016/j.apcatb.2024.123767>

Received 11 December 2023; Received in revised form 9 January 2024; Accepted 19 January 2024

Available online 24 January 2024

0926-3373/© 2024 Elsevier B.V. All rights reserved.

pollutants abatement, the intrinsic reactive oxygen species (ROS) production routes in photocatalytic reaction still suffer from low utilizing efficiency of CB-e^- . A (two plus one)-electron-transfer regime between O_2 and CB-e^- will enable the successive generation of H_2O_2 as the electron mediator to further convert to $\cdot\text{OH}$. Furthermore, the limited aqueously dissolved O_2 as the key precursor hinders the reaction kinetics [17,18].

Substituting O_2 by peroxide species with activated peroxy bond (O-O) such as H_2O_2 , persulfates, and ozone can tremendously increase both reaction kinetics and thermodynamics. The high solubilities of these peroxides in the reaction solution ensure fast mass transfer rates. In addition, the peroxy bonds within these peroxides are more facile to be activated by the external physical/chemical fields than the double bond between two oxygen atoms within O_2 because of their lower bonding energies (101–213 kJ/mol vs. 493.8 kJ/mol). The highly oxidative electron-rich peroxy bonds are ready to receive free electrons generated in photocatalytic reactions to dissociate into ROS. This process in turn promotes the production and separation of the photo-excited charge carriers. More importantly, the participation of these peroxides can fundamentally alter ROS generation pathways by affecting the reaction thermodynamics. The highly reactive ROS can be directly produced with a single-electron transfer process between the surface-adsorbed peroxide species and CB-e^- or generated by indirect electron transfer processes. As a result, the synergism between photo-excited charge carriers and peroxides remarkably boosts the yield of ROS and thus the treatment efficiency [19].

Graphitic carbon nitride ($\text{g-C}_3\text{N}_4$)-based materials have aroused intensive research interests as the efficient catalysts in peroxide-coupled photocatalysis. The special two-dimensional graphite-like layered structure composed of conjugated tri-s-triazine units endows $\text{g-C}_3\text{N}_4$ with merits such as strong visible light absorption ability, maneuverable physicochemical structures (Fig. 1) [20,21]. The merits such as low price, non-toxic properties, and tunable surface physicochemical properties endow carbon nitride as the promising catalysts in environmental catalysis [22]. Till now, several reviews have highlighted the applications of $\text{g-C}_3\text{N}_4$ -based materials in photocatalytic and coupled-photocatalytic wastewater treatments [23–25]. However, there is still a lack of a comprehensive summary of photocatalytic treatments coupled with various peroxides. Moreover, the involvement of peroxides not only requires the structural modifications of $\text{g-C}_3\text{N}_4$ to enhance their interactions, the direct/indirect electron transfer regimes for peroxides activation at the reaction interfaces and the subsequent ROS generation/evolution processes further increase the complexity for deciphering the underlying mechanisms. On this basis, this review begins with the regulation rules of $\text{g-C}_3\text{N}_4$ towards the efficient photocatalyst and peroxide activators. The modification/engineering approaches to optimize the band structure, electronic states, mass transfer rate, and physio-chemical properties are systematically summarized.

Furthermore, the activation pathways of the peroxides by the photo-excited charge carriers for ROS generation and pollutants removal are critically outlined and categorized. Finally, we propose the challenges and perspectives for the further research opportunities in peroxides-coupled photocatalysis using $\text{g-C}_3\text{N}_4$ -based semiconductors.

2. Engineering $\text{g-C}_3\text{N}_4$ toward efficient photocatalysis and peroxide activation

In peroxides coupled photocatalytic systems, the typical elementary reactions for ROS production mainly involve: excitation of the charge carriers under light irradiation (generation), migration of the photo-excited charge carriers to the surface of the semiconductors (separation and transfer), and surface reactions between photoexcited charge carriers and the peroxides and ambient water molecules for ROS generation (surface redox reactions) (Fig. 2). Based on the above reactions, engineered rules for activity enhancement of $\text{g-C}_3\text{N}_4$ can be enlightened from

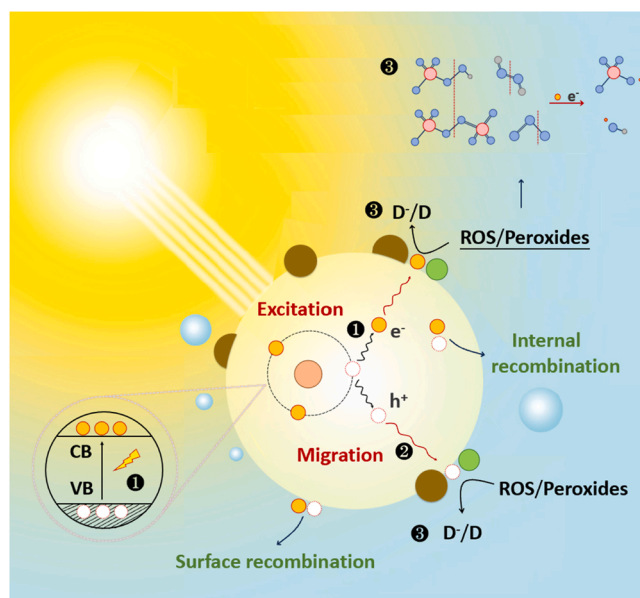


Fig. 2. Elementary reactions for ROS production in peroxides coupled photocatalysis: (1) Generation of photo-excited charge carriers under light irradiation. The orange and white spheres represent photoexcited electrons and holes, respectively; (2) Migration of photo-excited charge carriers to the catalyst surface; (3) Reaction between photo-excited charge carriers with peroxides adsorbed on the catalyst surface to produce ROS, which subsequently attack contaminants adsorbed on/near the catalyst surface. The green spheres represent peroxides.

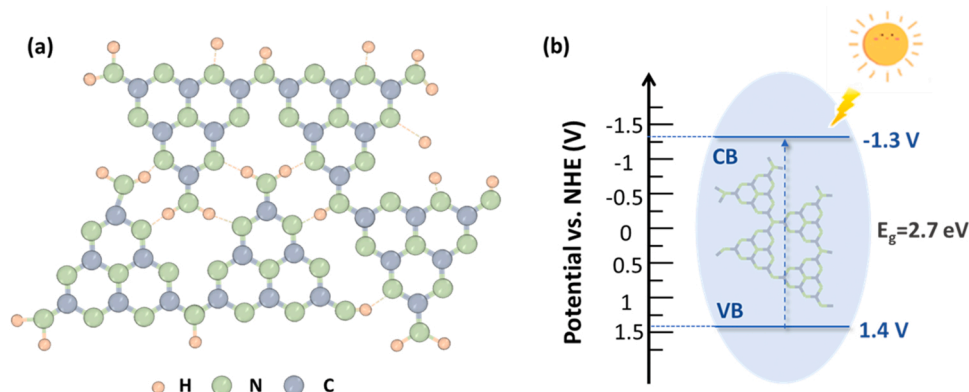


Fig. 1. (a) Atomic structure of tri-s-triazine-based pristine $\text{g-C}_3\text{N}_4$; (b) Typical energy band structure of pristine $\text{g-C}_3\text{N}_4$.

three aspects: (1) optimization of physical structure and band structure to enhance mass transfer rate and light absorption efficiency; (2) increment of the separation efficiency of the photoexcited charge carriers to boost their produced amounts; (3) regulation of the redox potentials of photoexcited charge carriers and intensification of the surface affinity to peroxides to lower the thermodynamic barriers and accelerate the surface reaction kinetics. The followings summarize the detailed modification strategies of g-C₃N₄.

2.1. Structure regulation

2.1.1. Morphology control

Carbon nitride is quite simple to prepare, and can be prepared by thermal polycondensation, solid phase synthesis, and hot solvent methods using melamine, urea, and dicyandiamide as precursors [10]. Pristine g-C₃N₄ obtains a relatively small specific surface area (SSA) because of the layered stacking of the tri-s-triazine units by the strong π - π interactions. The limited exposure of the active sites arising from the small surface area hinders the mass transfer between the photo-excited charge carriers and the reactant molecules [26]. Exfoliation by elevated temperature [27] or by liquid phase [28,29] has been recognized as an effective method to break the π - π interactions between g-C₃N₄ layers and enhance the surface area (Fig. 3a). The exfoliated two-dimensional (2D) layer shortens the diffusion length of the charge carriers and improves their separation efficiency [30,31]. Additionally, the confined charge carriers within the 2D surface accelerate the in-plane charge mobility and thus improve the reactivity. On the other hand, exfoliation can also fine-tune the band structure of g-C₃N₄ [28,29]. It has been reported that the conduction band (CB) of the exfoliated g-C₃N₄ was upshifted compared to the pristine one to produce more electronegative CB-e⁻ and thus increased the reaction thermodynamics with the peroxides for ROS generation [32]. Nevertheless, high annealing temperature or extended heat treatment duration can affect the stability of g-C₃N₄. Liquid-phase exfoliation is an alternative exfoliation method to high temperature

annealing, and it normally requires a mild heating temperature, a strong acidic anhydrous environment, and an extended treatment time for large-scale synthesis [33].

Pore construction is another strategy to improve the photocatalytic performance of g-C₃N₄ by increasing the population of active sites and enhancing the mass transfer [34,35]. Recently, inspiring micro-environment engineering has been applied to develop pore-rich g-C₃N₄-based semiconductors, especially for ordered micro- and meso-pores [36,37]. Apart from enriching the reactants within the confined pores, the formed confined space in pore-rich g-C₃N₄ increased nominal flow speed of the reaction solution, which enhanced the diffusion coefficients of the reactants and facilitated the adsorption-desorption cycle of the peroxides and the pollutants at the solid-liquid interface (Fig. 3b) [38]. Furthermore, the built-in electric field (BIEF) by the negatively charged groups within the pore structures is also conducive to improving the separation efficiency of photoinduced charge carriers. These features collectively enhanced the reactivity of the g-C₃N₄-based catalysts in peroxide-coupled photocatalytic process [38].

SiO₂-based hard-template method has been widely employed to construct ordered porous structures [39,40]. The structural stable ordered SiO₂ arrays provide a robust framework for the growth of the g-C₃N₄ as well as the anchored metal crystals [10,41]. However, the highly corrosive hydrogen fluoride or high concentration alkaline solution is required to completely remove the SiO₂ template, which increases the complexity and risk of operations. The use of organic soft templates such as ordered polymethylmethacrylate (PMMA) and polystyrene (PS) [42] microspheres successfully evades the above issues because of their thermal instability behavior (Fig. 3c) [43]. However, the blackish coking products arising from the incomplete decomposition of the organic template might adhere to the semiconductor surface and significantly reduce its reactivity by hindering the light absorption ability and surface reactions. Recently, template-free method relying on the phase transition differences between the precursors has been used

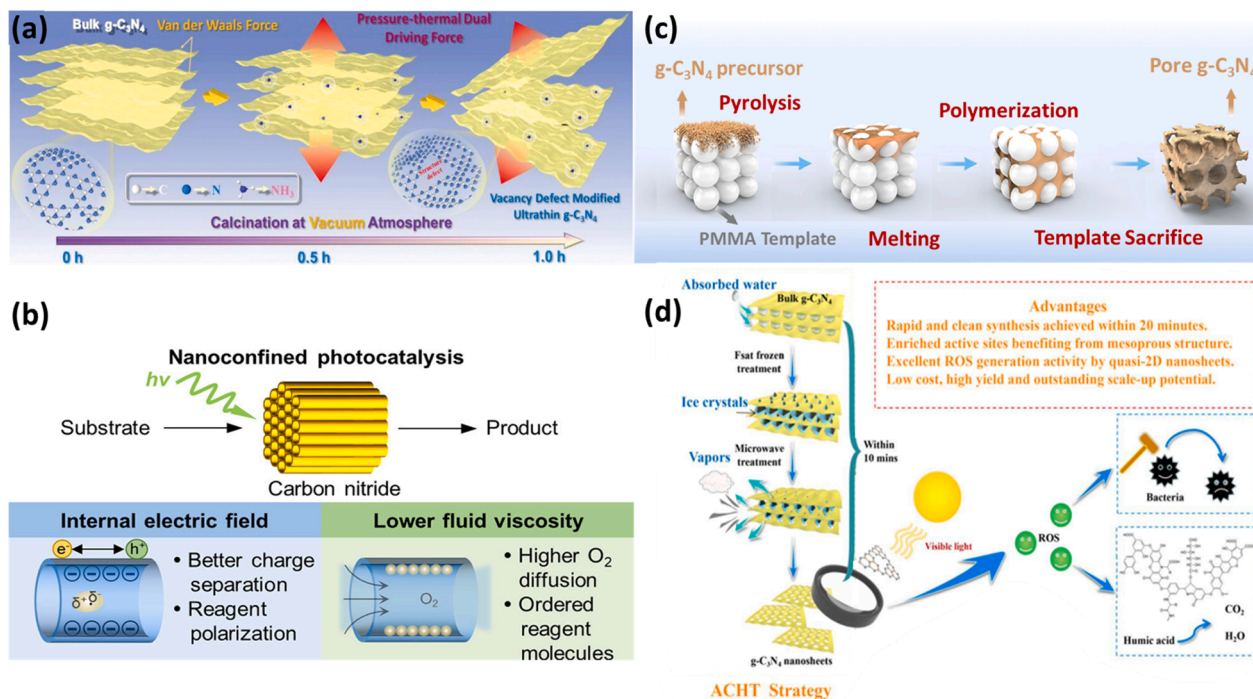


Fig. 3. (a) Schematic illustration for the formation of g-C₃N₄ with vacancy defect and ultrathin structure. Cited with permission from ref. [27]. Copyright 2023, Wiley-VCH; (b) Enhanced organic photocatalysis in confined flow through a carbon nitride nanotube membrane. Cited with permission from ref. [38]. Copyright 2021, American Chemical Society; (c) Schematic illustration of sacrificial template preparation of porous g-C₃N₄; (d) Schematic illustration of template-free preparation of porous g-C₃N₄. Cited with permission from ref. [44]. Copyright 2018, Elsevier.

for efficiently synthesizing ordered porous g-C₃N₄. Kang et al. synthesized ordered mesoporous g-C₃N₄ by alternated cooling and heating of the water-rinsed bulk g-C₃N₄ (Fig. 3d) [44]. In this process, liquid nitrogen and microwave power were used as the cooling and heating source, respectively. The drastic volume change within the g-C₃N₄ resulted from the rapid phase transform of the water molecules within g-C₃N₄ layers was responsible for the mesoporous structure formation.

Although exfoliation and pore construction can considerably enlarge SSA and maximize the exposure of active sites, photocatalytic activity does not always improve because of the increased band gap, which hinders the migration of the photo-excited charge carriers to the catalyst surface. Balancing surface area and band gap during the morphology regulation is critical for rational design of high-performance photocatalysts [45]. In addition, the agglomeration of the exfoliated layered structures and the collapse of pore structures in the actual catalytic reactions can lead to a sharp decrease in SSA, resulting in the dramatically declined activity. During the exfoliation process, the selection of a solution with higher polarity and suitable surface energy can avoid the occurrence of large agglomeration of the lamellar structure [46]. At the same time, by adjusting the pH of the solution, the surface charge of the material can be changed, thus affecting the stability of the lamellar structure suspended in water [28]. Balancing the mass ratio between carbon nitride precursors and the template is also critical to successfully construct the ordered porous structures without the collapse of the pores [47].

2.1.2. Defects control

Defective sites within the semiconductor structure play a crucial role in promoting reactivity [48]. The regulated electron distribution near the defects not only promotes the segregation of the photoexcited charge carriers and light absorption ability by altering the band structure [49], but also enhances the interaction with peroxides for their further activation because the electron-rich peroxy bond favored the adsorption at the electron-deficient sites on the defect structures [50]. Point defects such as N and C vacancies are conventional defective sites in g-C₃N₄

[51]. According to the local bonding environments, these point defects can be classified into the N atoms connected with three tris-triazines (N1), N atoms at the edge (N2) and center (N3), C atoms connected with three tris-triazines (C1), and C atoms at the edge (C2) (Fig. 4a) [50]. Among these vacancies, C2, N2 and N3 obtained relatively small formation energies and became the prevailing defective structures within g-C₃N₄ [52].

Thermal polymerization of N-containing precursors or adding reducing agents during the post treatment can create N vacancies. Amine groups within the C-N backbones of thiourea are more likely to experience incomplete condensation than those in melamine, and thus a higher amount of N vacancies was expected for thermal annealing of thiourea than melamine [53]. N vacancies can also be generated by reducing the doubly coordinated N₂ atoms under H₂ atmosphere [54, 55]. The presence of N vacancies regulated the electronic state around them by generating electron-rich regions that may become new adsorption-activation centers for peroxides [56]. Additionally, new defect energy levels emerged by the formation of N vacancies within the pristine g-C₃N₄, which enhanced the separation of the photoexcited charge carriers (Fig. 4b) [57]. Heat treatment of g-C₃N₄ can lead to the production of C vacancies. Compared to the N atoms, C atoms have a larger atomic radius and a smaller molecular weight that can receive a greater amount of kinetic energy of the inert gas molecules under elevated temperature, making them easier to escape from the g-C₃N₄ surface (Fig. 4c) [58].

In addition, irradiating catalysts with low-energy gas ions (e.g., Ar⁺, He⁺, E < 2 keV) is also an effective means of introducing surface defects [59]. Wang et al. successfully tuned the concentrations of C and N vacancies on g-C₃N₄ surface by controlling the He⁺ ion irradiation fluence [60]. However, the excessive defects hindered the yield of the photo-excited charge carriers, because the positions of the formed defective levels within the band structures also affected the trapping ability of photo-excited charge carriers (Fig. 4d) [56]. The photo-excited charge carriers can be trapped within vacancies and their energy is released in the form of phonons, rather than being transported to the

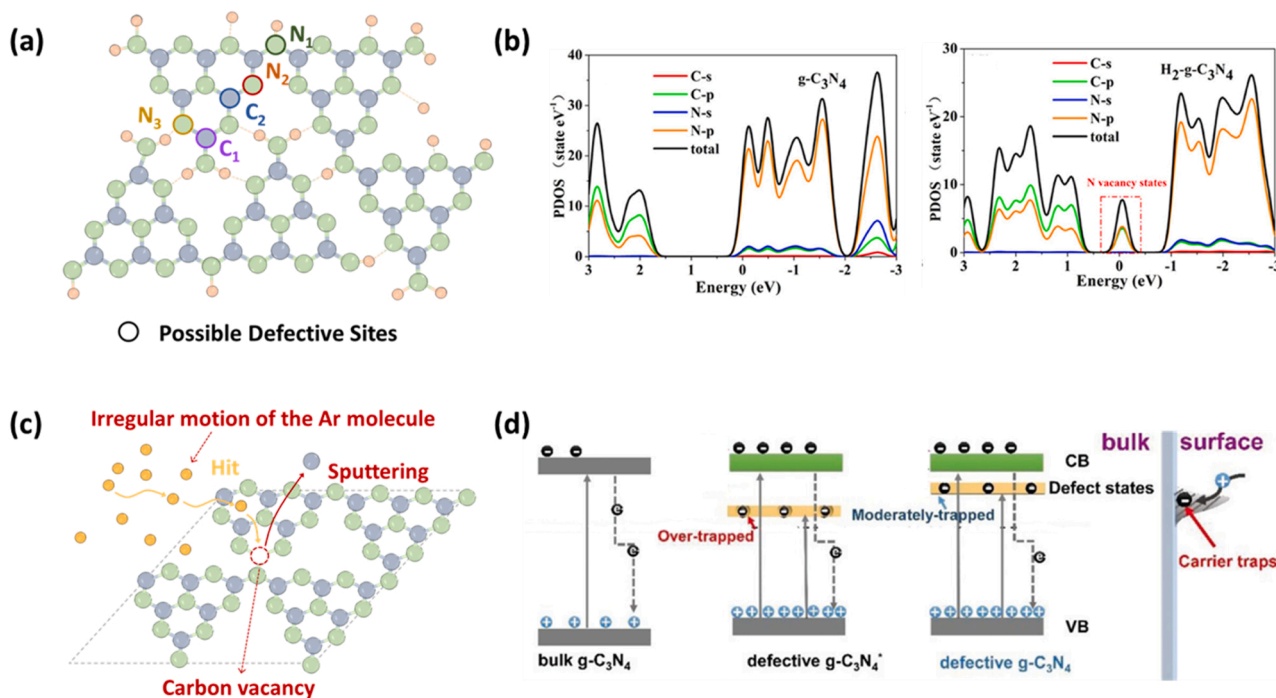


Fig. 4. (a) Illustration of possible defective sites on g-C₃N₄; (b) Calculated DOS for g-C₃N₄ and hydrogen-induced crystalline carbon nitride with vacancy defects (H₂-g-C₃N₄). (yellow: losing electrons, green: gaining electrons). Cited with permission from ref. 57. Copyright 2023, American Chemical Society. (c) Formation of C vacancies by low energy ion irradiation. Adapted with permission from ref. 58. Copyright 2016, Elsevier; (d) Electron-trapping ability of defect states with different positions. Cited with permission from ref. 56. Copyright 2023, Wiley-VCH.

surface of g-C₃N₄ for further reactions [61].

2.2. Heteroatom doping

2.2.1. Non-metal doping

Doping non-metal atoms (e.g., B, O, F, P, and S) into g-C₃N₄ framework is also a common strategy to enhance the reactivity of g-C₃N₄-based semiconductors [62,63]. The band structure and electronic properties of g-C₃N₄ can be fine-tuned by the doped metal-free heteroatoms owing to the electronegativity differences between doped heteroatoms and skeleton C/N atoms [64]. Doping highly electronegative non-metal atoms promotes the migration of electrons from the adjacent C atoms to the doping sites, favoring the adsorption of peroxides and/or pollutants [65]. The possible doping sites and the doping configurations are shown in Fig. 5a. B dopants strengthen the positive electrostatic potential on the g-C₃N₄ surface due to the electronegativity differences. This facilitates the electrostatic interactions with the negatively charged persulfate molecules. For example, the adsorbed persulfate molecules could be easily activated by B-doping sites on g-C₃N₄ via an electron transfer process to generate ROS (Fig. 5b) [66]. Meanwhile, B doping resulted in the migration of the electrons from adjacent N in the heptazine ring to the empty orbitals of B atoms and the formation of electron-rich regions near the B-N bond. The generated large molecular dipole enhanced charge separation and transfer [67]. O doping leads to a decrease in the electron density of neighboring C atoms and an increase in the electron density of N atoms because of the differences in electronegativities [68]. The doped O atoms can act as electron donors to reduce PMS into [•]OH and SO₄^{•-}, while the adjacent electron-deficient C atoms as electron acceptors can transform PMS into SO₅^{•-} and ultimately ¹O₂ [69]. In addition, the resulted lattice strain and the electronic

polarization effect caused by the charge redistribution around the O dopants generates an internal electric field which facilitates the separation of charge carriers while the lone pair electrons of O atoms delocalized into the g-C₃N₄ backbones increase the carrier density and mobility [49,70]. It has been reported O-doped g-C₃N₄ resulted in a 30-fold increase imidacloprid degradation compared with pristine g-C₃N₄ in photo-PMS coupled system [71]. Meanwhile, introduction of O atoms into g-C₃N₄ can induce the formation of oxygen-containing functional groups with electron-withdrawing abilities, which play an important role in both photo-excited carrier separation and peroxide adsorption [72].

In P-doped microenvironment, the delocalized lone electron from the P atom to the π -conjugated triazine ring and the intrinsic P-N bond polarization create the P⁺ center, which can act as the Lewis acidic sites for adsorbing peroxides and accelerating the separation of photo-excited charge carriers [73]. Projected density of states (PDOS) analysis revealed that P doping resulted in an elevated CB position (Fig. 5c) [64]. In the S-doped system, the S element participates in the formation of VB and CB orbitals in g-C₃N₄ and causes the appearance of new energy levels, which improves the carrier separation efficiency (Fig. 5d) [2]. Meanwhile, sulfur atom possesses a slightly higher electronegativity than C atom (2.58 vs. 2.55 eV). The replacement of N atoms by S atoms led to the transfer of the extra valence electrons from sulfur to neighboring carbon atoms in the g-C₃N₄ skeleton, resulting in the generation of nitrogen-vacancy state below the conduction band minimum (CBM) [74]. The formation of nitrogen-vacancy state together with positive charge density of the neighboring C atoms shrunk the bandgap and elevated the work function (Fig. 5d), which contributed to the production and separation of charge carriers and electron transfer between the surface-adsorbed peroxide species [2,75].

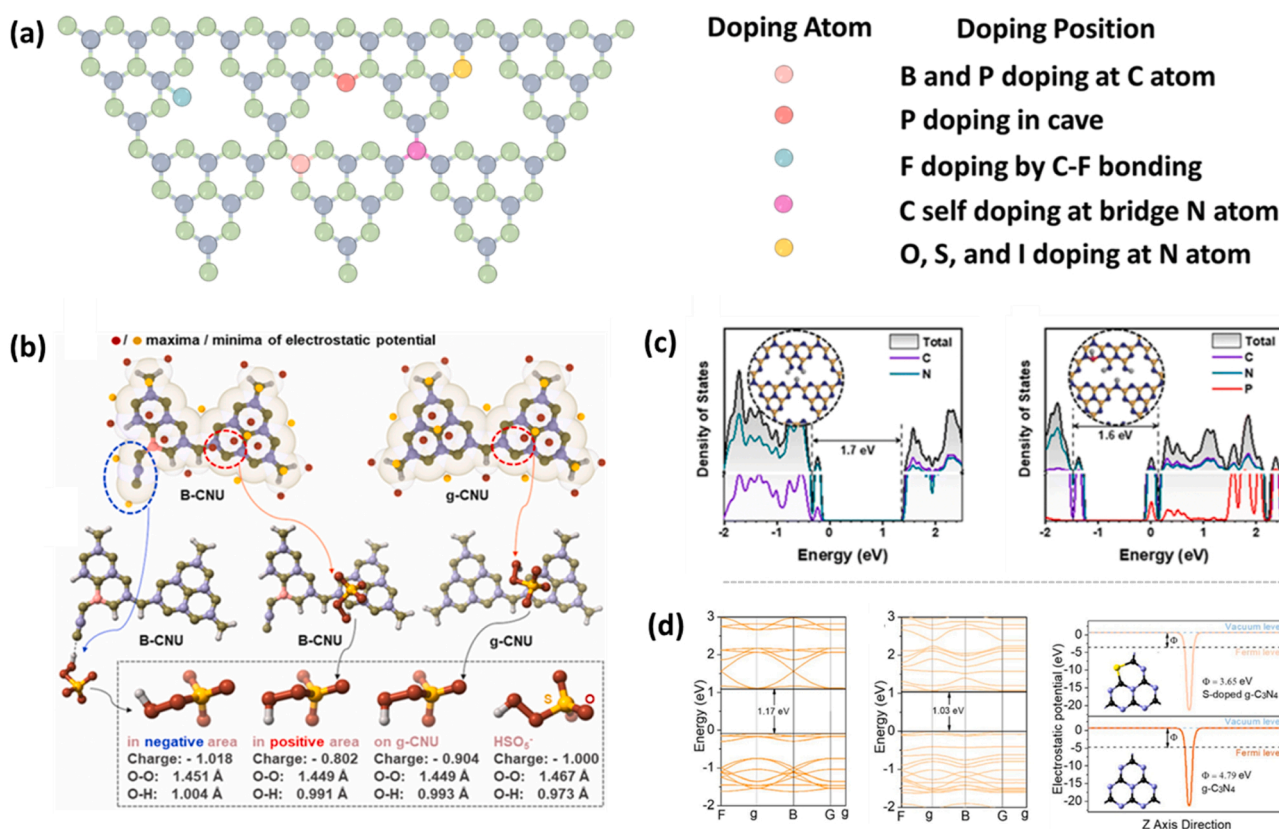


Fig. 5. (a) Possible doping sites of different non-metal elements in g-C₃N₄; (b) Extrema of electrostatic potential and optimized interaction patterns of HSO₅⁻ and positive/negative areas on catalyst surface. Cited with permission from ref. 66. Copyright 2021, Elsevier; (c) Variations in density of states (DOS) for holey g-C_{3-x}N₄ with/without P-doping. Cited with permission from ref. 64. Copyright 2023, Royal Society of Chemistry; (d) Variations in work functions and band structures for g-C₃N₄ with/without S-doping. Cited with permission from ref. 2. Copyright 2021, Elsevier.

Halogen atoms doping can tune the band structure and electronic states of g-C₃N₄ [76]. Formation of C-F, C-Cl and C-I bonds decrease the VB edge potential of g-C₃N₄ while C-Br bond narrows the band gap. The enhanced electronegativity of halogen atoms with the increase of their atomic numbers favors electrons transfer between the g-C₃N₄ skeleton. The upshifted Fermi level of g-C₃N₄ by halogen doping enables the facile escape of the surface electrons for peroxide activation. Moreover, the improved hydrophobicity by halogen atom doping further enhances the interaction with peroxide [77].

2.2.2. Metal doping

The central void position formed by three adjacent triazine units within the g-C₃N₄ structure provides an inviting microenvironment to accommodate the metal atoms, in which the lone pair electrons of pyridinic N atoms from the triazine units can hybridize with the d orbital electrons of the metal atoms [78]. This strong electron hybridization (or strong electronic metal-support interactions) robustly anchors the metal atom [79] and regulates the local electronic structures of g-C₃N₄. In previous studies, noble metals such as Pt and Ag have been broadly used to incorporate into g-C₃N₄ to enhance the reactivity [40,80-82]. The high work function of the doped noble metals could induce the migration of photo-excited charge carriers to them and thus prevent the recombination of charge carriers. Recently, research interests have

pivoted to doping or anchoring of 3d transition metals (e.g. Fe, Co, Ni and Cu) into the central void position or multidentate coordination sites of g-C₃N₄ because of their low price and high reactivity [83-86]. The single-atom dispersion maximizes the utilization efficiency of the 3d transition metal atoms and optimizes their intrinsic activity and selectivity [87,88]. The hybridization between the 3d orbital electrons of transition metal and the lone pair electrons of pyridinic N narrowed the bandgap of g-C₃N₄ [89]. The single-atom doped 3d transition metals can act as the electron-transfer bridges to assist the in-plane and inter-layer migration of charge carriers (Fig. 6a) [89]. Additionally, the redox cycle ($M^{(n+1)+} \leftrightarrow M^{n+}$) of the doped transition metal facilitates the activation of the peroxides (Fig. 6b) [90]. Taking the application of single-atom doped Fe-g-C₃N₄ in photo-Fenton system as an example, the reactive Fe²⁺ could be continuously provided as the H₂O₂ activator via the reduction of Fe³⁺ by photoexcited electrons, while the Fe-N_x sites acted as a bridge to promote charge carrier separation [91-93].

Alkali metals can be doped in the interlayer positions or the conjugated planes of g-C₃N₄ to alter the electron density and promote the electron transfer. Xiong et al. prepared K-doped and Na-doped g-C₃N₄ by thermal polymerization of thiourea and XBr (X = K, Na) [94]. It was found that K atoms could be more easily doped in the g-C₃N₄ interlayer bridging positions than Na atoms, which accelerated the carrier migration efficiency while Na atoms tended to be integrated into central void

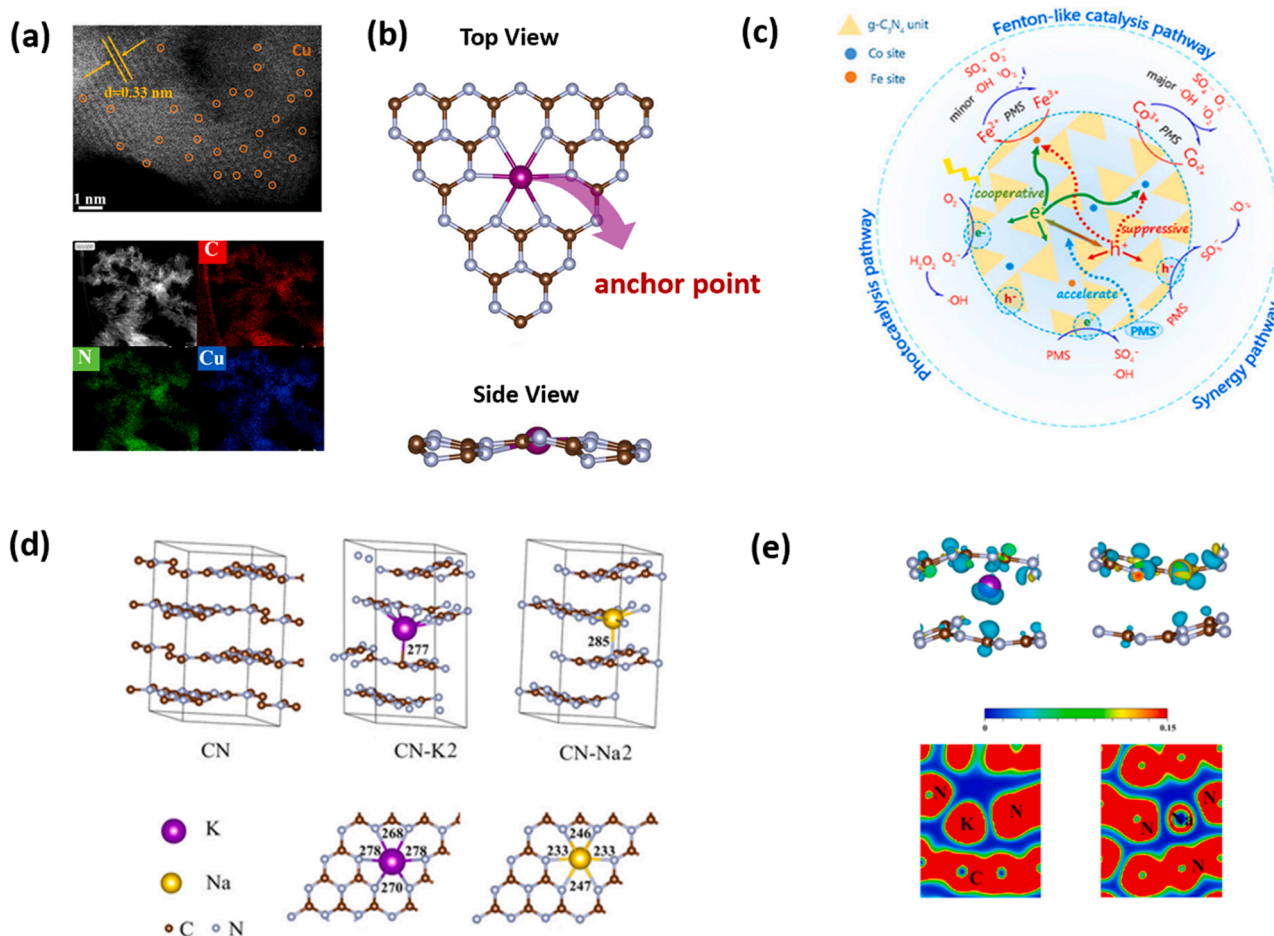


Fig. 6. (a) HAADF-STEM image and the corresponding energy-dispersive spectroscopy (EDS) mapping of single Cu atoms/crystalline g-C₃N₄ samples. Adapted with permission from ref. 86. Copyright 2020, American Chemical Society; (b) Schematic illustration of metal anchor points on carbon nitride. Cited with permission from ref. 79. Copyright 2023, American Chemical Society. (c) Synergy mechanism between photocatalysis and peroxymonosulfate activation on a Co/Fe bimetal-doped carbon nitride. Cited with permission from ref. 90. Copyright 2023, American Chemical Society; (d) Calculated crystal structures of CN, CN-K2 and CN-Na2 and topviews of the doped layer in CN-K2 and CN-Na2, correspondingly. Selected distances are marked in pm. Cited with permission from ref. 94. Copyright 2016, American Chemical Society; (e) Charge difference distribution of CN-K2 and CN-Na2, and ELF analysis of CN-K2 and CN-Na2. The yellow region denotes charge depletion while the blue region denotes accumulation. Cited with permission from ref. 94. Copyright 2016, American Chemical Society.

position by forming ionic bonds with the pyridinic N atoms (Fig. 6c). Doping of K and Na ions leads to charge rearrangement of g-C₃N₄. K ions can chemically bond with atoms in two neighboring layers to form charge transfer channels and bridge these layers, facilitating carrier separation and transfer. However, the presence of Na atoms in the CN planar cavities increases the in-plane electron density and induces high carrier recombination (Fig. 6d) [94].

Nevertheless, high metal loading concentration will disrupt the conjugated g-C₃N₄ structure which in turn decreases mobility of the charge carriers and thus reduces the reactivity. Moreover, the excessive metal atoms might agglomerate on g-C₃N₄ surface and become the recombination center of the charge carriers, resulting in a decrease in quantum efficiency and photocatalytic performance [95]. Therefore, it

is crucial to consider the optimization the heteroatom doping species, position, and amount, which collectively affects conductivity, band structure, and generation/separation of charge carriers.

2.3. Heterojunction engineering

In peroxide-coupled photocatalytic systems, redox potentials and the separation efficiency of the charge carriers are important factors in determining the ROS generation rate and population. Although heteroatom doping can reduce the bandgap of g-C₃N₄ and enhance the generation of charge carriers, the reduced bandgap often leads to the production of charge carriers with decreased redox potentials which affects the reaction kinetics for ROS generation [96]. Additionally, the

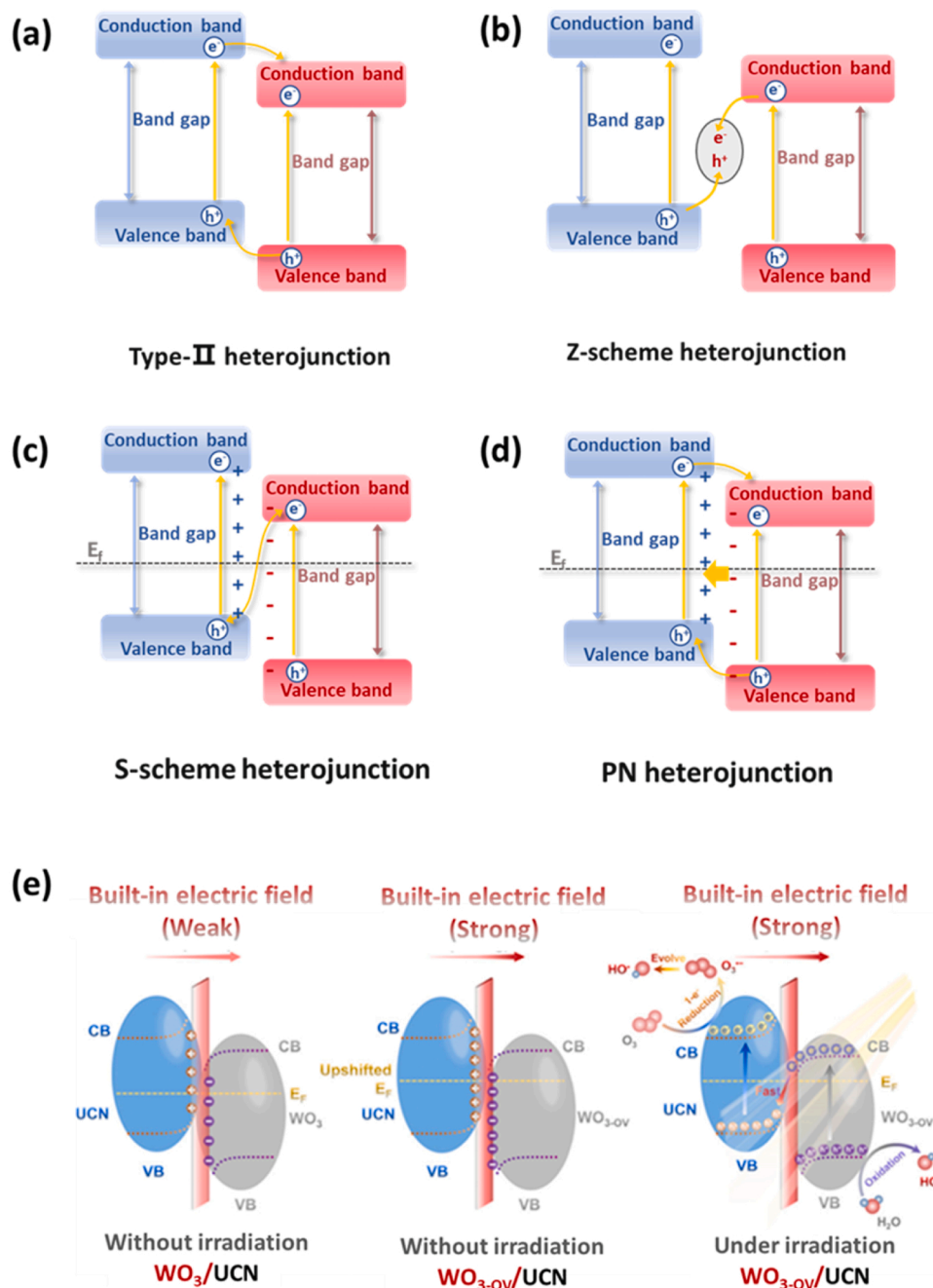


Fig. 7. Schematic illustrations of the charge carriers transfer pathways in Type II (a), Z-scheme (b), S-scheme (c), and p-n type (d) heterojunctions; (e) Illustration of the produced BIEF with the band edge bending near the interface of WO₃/urea-modified g-C₃N₄ (UCN) and defective WO₃/UCN (WO_{3-OV}/UCN). Cited with permission from ref. 17. Copyright 2022, American Chemical Society.

photo-excited charge carriers still suffer from a fast recombination rate. These as-mentioned issues can be solved by combining g-C₃N₄ with other semiconductors to form heterojunction structures [97,98]. According to different charge transfer mechanisms between the g-C₃N₄ and combined semiconductors, common heterojunctions can be classified as type I, type II, Z-type, S-type (direct Z-type), and p-n heterojunctions. Among them, type II, Z-type, S-type, and p-n heterojunctions are widely adopted (Fig. 7a-d) [99-101]. Type II heterojunctions achieve the spatial separation of charge carriers by transferring them onto the band structures with low redox potentials, which sacrifices the reaction kinetics (Fig. 7a) [102]. In Z-type heterojunctions, the unique transfer route of the charge carriers between the semiconductors guarantees both the spatial separation and the high redox potentials of the charge carriers (Fig. 7b) and an electron mediator is usually required for transportation of the charge carriers in Z-type heterojunctions [103]. As a special form of Z-type heterojunction, S-scheme heterojunction, also known as the direct Z-type heterojunction, can achieve fast generation and efficient separation of charge carriers without a mediator (Fig. 7c). Fermi levels of the semiconductors within the S-scheme heterojunction will realign under light irradiation which results in the bending of their band structures. The bent band structures will generate the BIEF at the interface of semiconductors, which accelerates the transfer of charge carriers to the band structures with high redox potentials and prevents their recombination (Fig. 7e) [17]. Similarly, an internal electric field is also expected in the p-n type heterojunction by diffusion of the carriers to the oppositely charged semiconductors. This electric field forces the migration of the photoexcited charge carriers to CB of the n-type semiconductor and VB of the p-type semiconductor to achieve the spatial separation (Fig. 7d) [104].

Selection of semiconductors with suitable band structures and construction of advantageous heterojunction type is the key to promoting the reactivity of the peroxide-coupled photocatalytic system. Compared to most of the semiconductors, g-C₃N₄ obtains a more negative CB and the photo-excited CB-e⁻ from g-C₃N₄ can induce a fast reaction thermodynamics with the peroxides for ROS generation [105]. To make the full use of these highly reductive CB-e⁻ in g-C₃N₄, it is preferable to construct Z- or S-scheme heterojunctions. Various metal oxides, metal sulfide, and metal-free semiconductors have been successfully used to construct Z- or S-scheme heterojunction systems with g-C₃N₄ [106]. Construction of efficient heterojunction structures relies not only on the matching of band structures, but also on the intimate contact between the composed semiconductors. Increasing SSA of semiconductors is a simple method to enhance the contact, which is beneficial to construct the heterojunction structures. Manipulating the surface charge of the composed semiconductors is another approach to intensify the interactions between the composed semiconductors via electrostatic attractions. Moreover, migration of the charge carriers can also be improved by strong electrostatic force. Additionally, the degree of lattice matching is another critical factor that affects the formation of heterojunctions. The dangling bond generated by a mismatch of the lattices at the composed interfaces will become the recombination centers for the photoexcited charge carriers, which reduces the quantum yield efficiency [107]. Although heterojunction engineering can achieve the separation of the photo-excited charge carriers and maintain the charge carriers with high redox potentials, the complexity and the high cost in heterojunction preparation process are the problems that need to be overcome in the future.

Elucidating the transfer pathways of the charge carriers between the hybridized semiconductors is of great significance in differentiating the type of heterojunction and designing the reactive photocatalysts. The two intrinsic factors within the semiconductors that govern the transfer of charge carriers are their work functions and band-edge potentials which determine the ability for CB-e⁻ production and the transfer trend of CB-e⁻, respectively. The combined spectroscopy and DFT analysis are often employed to examine the band structures of the semiconductors and the distribution of the electrons at their contact interface [108,109].

UV-visible diffuse reflection spectroscopy (UV-Vis DRS) and ultraviolet photo-electron spectroscopy (UPS) can be used to analyze the bandgap and the valence band/work function of the semiconductor accordingly [110,111]. The DFT-based calculations further determine the theoretical work functions of the semiconductors [112]. Moreover, the band-edge potentials of the composed semiconductors can be acquired by scrutinizing the realignment trend of their Fermi levels as well as the electron distribution at the contact interface. Free radical detection is also an indirect method to determine the type of the heterojunction because •OH and O₂^{•-} are produced only when the redox potentials of the charge carriers surmount the formation potentials of these ROS [113]. Electron paramagnetic resonance (EPR) combined with spin trapping agents can *in situ* detect and differentiate different ROS, which can collaborate with competitive quenching tests for ROS determination. Recently, some *in situ* examination techniques such as *in situ* irradiation X-ray photoelectron spectroscopy (ISIXPS) and Kelvin probe force microscopy (KPFM) have also developed to directly monitor surface potential distribution and the movement of the charge carriers [113-115]. It should be noted that these *in situ/operando* techniques usually obtain the local electronic details within the examination area and might not reflect the features of the bulk heterojunction composites. Therefore, multiple characterization techniques are still required to acquire the overall chemical, electronic and band information [113].

2.4. Hybridizing organic compounds

The highly electronegative sp³ N atoms connecting each melem unit within the g-C₃N₄ structure affect delocalization of the photoexcited charge carriers [116]. Regulating the electronegativity of the melem units via copolymerization reactions at molecular level is another strategy to improve the activity of g-C₃N₄. Pyromellitic dianhydride (PMDA) is a highly electron-deficient molecule with two electron-withdrawing anhydride groups which can be facilely hybridized with g-C₃N₄. In PMDA decorated g-C₃N₄, the melem units and PMDA act as the active sites for oxidative and reductive reactions accordingly, which promote the separation of the photoexcited charge carriers and advance the subsequent peroxide activation for ROS generation [117]. Similarly, malonamide (MLD) has been copolymerized with melamine and urea to tune the conductivity and the delocalization ability of the charge carriers [118]. After loaded with Fe₃O₄, the obtained hybrid catalyst demonstrated a high reactivity in photo-Fenton system for aqueous tetracycline treatment, which can degrade more than 95% tetracycline (20 mg/L) with 80 min.

In light of the above discussions, the activity of the g-C₃N₄ in peroxide-coupled photocatalytic system can be engineered by a series of modifications such as exfoliation, pore engineering, doping, and compositing. Nevertheless, it remains essential to consider some issues associated with modification and engineering processes. Although g-C₃N₄ can be successfully exfoliated to increase its SSA and provide more active sites, the generation of excessive structural defects may hamper the electron transfer rate and acts as the recombination center. Thus, balancing SSA and population of structural defects is of paramount significance. Doping/compositing metal components on g-C₃N₄ can inevitably result in metal leaching issues within the reaction process. Development of single-atom metal doping, metal-free doping, and enhancing the stability of the anchored metal components are the solutions to alleviate the leaching issue. Heterojunction engineering can tailor the band structures of the semiconductor composites, which improves light absorption ability and the separation of the photo-excited charge carriers at the contact interfaces. Formation of heterojunction structures with the g-C₃N₄ can also increase the number of active sites for the adsorption of peroxides or aqueous contaminants by promoting the delocalization of π -conjugated structures. Nevertheless, most of the structures are specific for the adsorption of only one or a few substances which limits the real application. It is imperative to construct the active sites that are favorable for adsorption of a broad range of reactants.

Additionally, designing g-C₃N₄ heterojunctions that can adsorb the peroxides on the CB-e⁻-rich region is promising to enhance the reaction kinetics.

3. Electron transfer regimes in peroxide-coupled photocatalytic processes

For most peroxides, light from visible band fails to directly activate the peroxy bonds because of the insufficient energy stimulation, thus making the high-energy ultraviolet (UV) band as the only option for cleaving the peroxide O-O bond towards ROS production. However, the scarcity of UV bands in the solar spectrum (~5%) hinders the exploitation of the solar light. The limited propagating rate and penetration depth of UV light in water further hinder the photon utilization efficiency [119]. Therefore, breaking the peroxy bonds by accepting the electrons from the added heterogenous photocatalysts and/or photo-sensitive matters is an alternative to passively receiving the photons with high energy. In peroxide-coupled photocatalytic, three possible electron transfer regimes exist for peroxide activation towards ROS production depending on the transportation pathways and the sources of the photo-excited electrons.

3.1. Direct electron transfer regime

Direct electron transfer is considered as one of the most efficient pathways to trigger the cleavage of the peroxy bonds and the subsequent ROS generation because the electrons in the unsaturated peroxy single bonds are quite electrophilic and ready to accept electrons for activation. Recent studies on direct electron transfer mechanisms are summarized in Table 1. Upon light irradiation, g-C₃N₄-based semiconductors can convert the photon energy and excite the electrons from ground states to high-energy levels, generating the photo-excited charge carriers. The photo-excited electrons migrate onto the catalyst surface and then induce activation of the surface-adsorbed peroxides. Furthermore, the rapid reactions between the reductive photo-excited electrons and the oxidative peroxides enhance the separation and production of the charge carriers which thus promote the photocatalytic activity. Therefore, the treatment efficiency of the coupled systems can be governed by the following two factors (i) surface affinities to the peroxides, in which the strong surface interaction is favorable for the intensive electron transfer; (ii) band structure of semiconductors, in which the high valence band position thermodynamically advances the peroxide activation.

Table 1

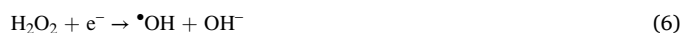
Summary of direct electron transfer regime in carbon nitride-triggered photocatalysis coupled with peroxides.

Catalysts name	Main active species	Target pollutant	Peroxide dose	degradation efficiency	Activation system	Ref
Fe-g-C ₃ N ₄ /Bi ₂ WO ₆	O ₂ ^{•-} , ¹ O ₂	tetracycline 10 mg/L	1 mM	120 min 93.9%	Vis/H ₂ O ₂ /g-C ₃ N ₄	[108]
Zn _{1-1.5x} Fe _x S/g-C ₃ N ₄	•OH	p-nitrophenol 10 mg/L	1 mM	60 min 96%	Vis/H ₂ O ₂ /g-C ₃ N ₄	[109]
PKCN	•OH	methylene blue 10 mg/L	35 mM	60 min ~90%	Vis/H ₂ O ₂ /g-C ₃ N ₄	[120]
TiO ₂ -P/g-C ₃ N ₄	O ₂ ^{•-} , •OH	Tetracycline 100 mg/L	-	100 min ~80%	Vis/H ₂ O ₂ /g-C ₃ N ₄	[121]
H ₂ -g-C ₃ N ₄	SO ₄ ^{•-} , O ₂ ^{•-}	bisphenol A 50 mg/L	25 mg	15 min 100%	Vis/PMS/g-C ₃ N ₄	[57]
PI-g-C ₃ N ₄	¹ O ₂ , O ₂ ^{•-} , h ⁺	bisphenol A 1 mg/L	5 mM	60 min 96%	Vis/PMS/g-C ₃ N ₄	[122]
CO-C ₃ N ₄	SO ₄ ^{•-} , O ₂ ^{•-} , ¹ O ₂ , h ⁺	tetracycline hydrochloride 10 mg/L	200 mg/L	40 min 97.77%	Vis/PMS/g-C ₃ N ₄	[72]
TiO ₂ /g-C ₃ N ₄	SO ₄ ^{•-} , O ₂ ^{•-} , h ⁺	acetaminophen 5 mg/L	2 mM	30 min ~100%	Vis/PMS/g-C ₃ N ₄	[123]
B-CNU	¹ O ₂	2,4-dichlorophenol 0.06 mM	0.5 mM	90 min 100%	Vis/PMS/g-C ₃ N ₄	[66]
g-C ₃ N ₄	SO ₄ ^{•-} , O ₂ ^{•-} , •OH	carbamazepine 2.0 μM	0.5 mM	90 min ~70%	Vis/PMS/g-C ₃ N ₄	[124]
ECN	SO ₄ ^{•-}	bisphenol A 20 mg/L	40 mg/L	20 min 100%	Vis/PMS/g-C ₃ N ₄	[125]
CTF-SDs	¹ O ₂	bisphenol A 0.1 mM	0.3 mM	90 min 100%	Vis/PMS/g-C ₃ N ₄	[126]
MCN	¹ O ₂ , O ₂ ^{•-} , h ⁺	2,4,6-trichlorophenol 10 mg/L	0.4 mmol/L	150 min 100%	Vis/PDS/g-C ₃ N ₄	[127]
MCN	¹ O ₂	β-lactam antibiotics 2 mg/L	0.01 mM	60 min 99%	Vis/PDS/g-C ₃ N ₄	[128]
CuFe ₂ O ₄ /g-C ₃ N ₄	•OH, O ₂ ^{•-} , SO ₄ ^{•-} , h ⁺	propranolol 0.02 mM	0.2 mM	120 min 56.5%	Vis/PDS/g-C ₃ N ₄	[129]
g-C ₃ N ₄ /Fe-MCM-48	•OH, h ⁺	azithromycin 50 mg/L	50 mg/L	11 min 98.8%	Vis/O ₃ /g-C ₃ N ₄	[111]
Cl/S-CN	¹ O ₂ , O ₂ ^{•-} , •OH	tetracycline 100 mg/L	10 mg/L	10 min 90.1%	Vis/O ₃ /g-C ₃ N ₄	[112]
WUCN	•OH	oxalic acid 100 mg/L	25 mg/L	20 min 100%	Vis/O ₃ /g-C ₃ N ₄	[17]
F/Cl/Br/I-CN	•OH, h ⁺	atrazine 10 mg/L	20 mg/h	15 min 66.5%/57.1%/49.8%/61.2%	Vis/O ₃ /g-C ₃ N ₄	[77]
g-C ₃ N ₄	•OH, h ⁺ , O ₂ ^{•-}	methylene blue 20 mg/L	20 mg/L	30 min ~90%	Vis/SPC/g-C ₃ N ₄	[130]

3.1.1. Photo-Fenton reaction

The covalency nature of the peroxy bond in H₂O₂ (O-O bond length 1.453 Å, bond energy 213.1 kJ/mol) advances its affinity towards accepting electrons for evolving into highly oxidative free radicals [7]. In a conventional Fenton process, H₂O₂ captures electrons from Fe²⁺ to generate •OH and Fe²⁺ is subsequently oxidized into Fe³⁺ [23]. However, the reduction kinetic from Fe³⁺ to Fe²⁺ can be quick slow (0.02 M⁻¹S⁻¹), and this sluggish reduction becomes the rate-determining step for the continuous H₂O₂ activation and thus reduces the efficiency for Fenton reaction [131]. Additionally, a large amount of sludge will be produced by Fe-induced agglomeration, resulting in loss of the iron species and the decrease in catalytic activity. On the other hand, H₂O₂ can be directly activated by ultraviolet light with a band length of less than 300 nm, yet the low absorbance coefficient (ε, 18.6 M⁻¹cm⁻¹ at 254 nm) hinders its effective conversion for hydroxyl radical production [132]. The integration of photocatalysis with the Fenton reaction can significantly enhances the H₂O₂ activation efficiency relying on the direct electron transfer from the semiconductor produced CB-e⁻ to H₂O₂ (Eq. 6) [108]. Additionally, this CB-e⁻-induced H₂O₂ activation pathway circumvents the participation of Fe species which broadens the effective working pH window and avoids sludge production (Fig. 8) [109,121]. In direct electron transfer regime, the number and the reduction potential of the photo-induced CB-e⁻ decide the kinetics and the thermodynamics of the H₂O₂ activation process, respectively. Furthermore, the high affinity of the semiconductor surface towards H₂O₂ and the fast migration of the CB-e⁻ within the semiconductor are also of great importance to guarantee the reaction proceeding. For example, Sharma et al. synthesized CuO/g-C₃N₄ Z-scheme heterojunction for degradation of 2, 4-dimethyl phenol [133]. The Z-scheme heterojunction successfully achieved the separation of charge carriers with high redox potentials and the high reductive CB-e⁻ from the g-C₃N₄ can active H₂O₂ for •OH production.

Noted that in g-C₃N₄ induced photocatalytic reactions, H₂O₂ can be *in situ* generated because of the high reductive potential of the CB of g-C₃N₄. Recent years, fruitful researches have taken the advantage of this *in situ* generated H₂O₂ to reduce or avoid the addition of external H₂O₂ [134,135]. Compared with the conventional Fenton process, the H₂O₂ utilization efficiency can be greatly enhanced. The detailed discussion of the relative mechanisms will be provided in the peroxide-coupled photocatalytic reaction dominated by indirect electron transfer regime section.



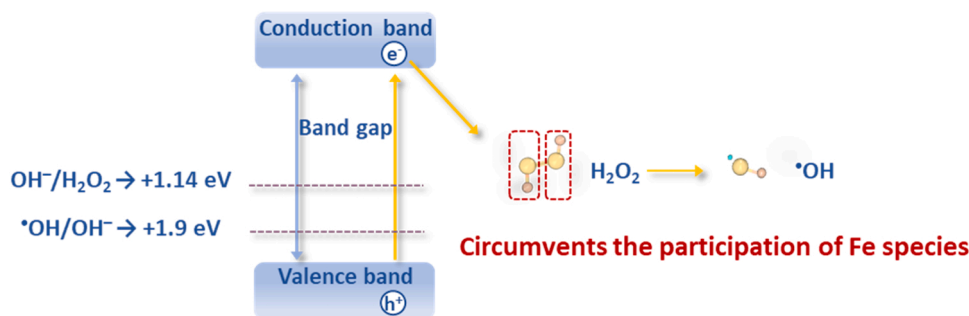
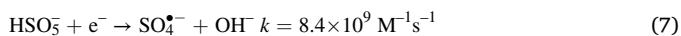


Fig. 8. Schematic illustration of direct electron transfer regime in the photo-Fenton reaction.

3.1.2. Photo-persulfate reaction

As the derivatives of H_2O_2 , PMS and PDS molecules are quite structurally similar to H_2O_2 , in which either one or both of the terminal H atoms of the H_2O_2 were substituted by the sulfite groups ($-\text{SO}_3$). Consequently, the length of peroxide bonds within the PMS (1.460 Å) and PDS (1.497 Å) molecules is longer than that of H_2O_2 (1.453 Å) [7]. The extended peroxy bond lengths with the persulfates facilitates the activation by the photo-excited CB-e^- via the direct electron transfer regime. Although persulfates can be directly activated by ultraviolet light, they fail to be activated by visible light with low photon energy of 1.63–3.26 eV [7]. Radical-dominated oxidation pathway is prevalent in photo-persulfate system induced by direct electron transfer regime [57, 122]. The persulfate molecules can act as the electron acceptors to receive photo-excited CB-e^- from the semiconductors, leading to the cleavage of the peroxy bond for generating $\text{SO}_4^{\bullet-}$ and/or $\bullet\text{OH}$ (Fig. 9 and Eq. 7–9) [124,125,127]. Moreover, VB-h^+ can also participate the radical formation even when its oxidation potential cannot surpass the direct water oxidation for $\bullet\text{OH}$ generation (2.4–2.7 V_{NHE}). In this scenario, VB-h^+ can oxidize HSO_5^- to form $\text{SO}_5^{\bullet-}$ (1.12 V_{NHE}), which can further evolve into $^1\text{O}_2$ or be directly used for contaminant decontamination (Fig. 9, Eqs. 10–11) [136]. The efficient usage of VB-h^+ promotes the separation of the charge carriers and simultaneously enhances production of photo-excited CB-e^- and free radicals. Compared to the $\bullet\text{OH}$ produced in the photo-Fenton reaction, the $\text{SO}_4^{\bullet-}$ generated in the photo-persulfate systems has a higher oxidation potential (2.5–3.1 V_{NHE} of $\text{SO}_4^{\bullet-}$ vs. 2.3–2.7 V_{NHE} of $\bullet\text{OH}$) and a much longer lifespan (30–40 μs of $\text{SO}_4^{\bullet-}$ vs. 20 ns of $\bullet\text{OH}$), which ensure a stronger oxidation capacity and longer diffusion distance to attach the contaminants [8].



In $\text{g-C}_3\text{N}_4$ -triggered direct electron transfer regime for photo-persulfate systems, it has been reported that introducing strong

electron withdrawing groups such as $-\text{C}\equiv\text{N}$ and $-\text{C-OH}$ onto $\text{g-C}_3\text{N}_4$ can achieve effective separation photo-generated charge carriers [137]. High persulfate utilization efficiency can be attained by transferring the photo-excited CB-e^- from these electron withdrawing groups to the persulfates due to the strong binding with the electrophilic persulfates. Defect engineering and metal-atom doping can also increase the charge transfer rates and promote persulfate activation. Liu et al. used a molten salt-assisted thermal polymerization method to insert Li^+ and K^+ into $\text{g-C}_3\text{N}_4$ [138]. Li^+/K^+ insertion created the cyano- defects which facilitated the PMS adsorption. Upon light irradiation, the photo-excited CB-e^- tended to transfer from the catalyst surface to the adsorbed PMS for $\text{SO}_4^{\bullet-}$ formation. Meanwhile, the metal dopants increased the interaction between the catalyst surface and PMS by the strong electrostatic attraction which abstracted electrons from PMS to the metal sites. The electron-deficient PMS could be then activated into $^1\text{O}_2$. Compared to the pristine $\text{g-C}_3\text{N}_4$, the Li^+/K^+ modified $\text{g-C}_3\text{N}_4$ resulted in a 13-fold increase in acetaminophen degradation kinetic because of the massively generated $\text{SO}_4^{\bullet-}$ and $^1\text{O}_2$. Apart from hybridizing inorganic semiconductors with $\text{g-C}_3\text{N}_4$, perylene tetracarboxylic dianhydride (PTCDA) as an organic semiconductor was also integrated with $\text{g-C}_3\text{N}_4$ via the amidation reaction and an all-solid Z-scheme heterojunction was achieved. The BIEF within the heterojunction resulted in a more effective separation of photo-excited charge carriers and obtained a higher conductivity than PTCDA and $\text{g-C}_3\text{N}_4$ counterparts, thus promoting the PMS activation via the direct electron transfer regime [122].

Besides reacting with photo-excited CB-e^- to produce free radicals, persulfate molecules can also adsorb on vacancies, defects, or electron deficient sites of the $\text{g-C}_3\text{N}_4$ -based catalysts without dissociation, on which persulfates can be transformed into the surface-adsorbed metastable activated intermediates ($\text{PMS}^*/\text{PDS}^*$) for direct oxidation of the contaminants via an electron transfer process [139]. Compared with PMS, PDS has a higher oxidation potential and is more likely to adsorb on electron deficient sites, forming the PDS^* structure [140]. This structure elevates the surface potential of the catalyst, favoring the electrophilic reactions with pollutant molecules that are also adsorbed on the catalyst surface. During this reaction, the oxidation ability of this nonradical system depends on the half wave potential ($\phi_{1/2}$) of the organic pollutants. Pollutants with low $\phi_{1/2}$ values are more conducive to losing electrons, thereby facilitating the electron transfer process from

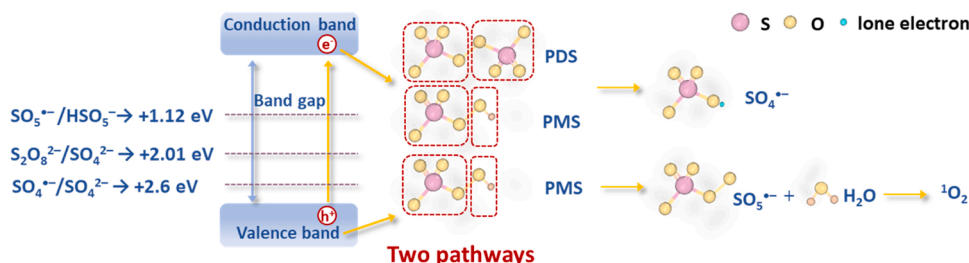


Fig. 9. Schematic illustration of direct electron transfer regime in the photo PMS/PDS reaction.

PDS* to pollutants. On the contrary, contaminants with high $\phi_{1/2}$ values (such as nitrophenol, hydroxyacetophenone, and methyl p-hydroxybenzoate) are resistant to the electron transfer process and thus retard the reaction [141].

3.1.3. Photo- O_3 reaction

O_3 molecules can be directly activated by ultraviolet irradiation with a wavelength less than 300 nm, especially at 254 nm (with an absorbance coefficient of $3300 \text{ M}^{-1}\text{cm}^{-1}$), however, the UV light utilization efficiency together with the O_3 activation efficiency is still low [142]. Meanwhile, direct activation by UV light also undergoes the as-mentioned drawbacks for application of ultraviolet light. Photocatalytic ozonation induced by g- C_3N_4 -based photocatalysts can harness visible light from the solar irradiation [111,112]. The reductive photo-excited $CB-e^-$ rapidly reacts with the oxidative O_3 for $\cdot OH$ evolution. Compared to the conventional photocatalytic process where a three-electron transfer pathway is required for $\cdot OH$ generation, this single-electron transfer pathway synergistically improves the utilization efficiencies of both charge carriers and O_3 towards $\cdot OH$ formation (Fig. 10a). Additionally, the higher oxidation potential (2.1 vs. 1.23 V_{NHE}) and the greater solubility of O_3 than those of O_2 further enhance the reaction rate.

Xiao et al. correlated the structure of the g- C_3N_4 with the amount of the photo-excited $CB-e^-$ with the aid of *in situ* electron paramagnetic resonance (EPR) technique. Bulk g- C_3N_4 was calcined in Ar/air at different temperatures to alter the band structures [24]. It was found that the conduction band edge potential (CBEP) is a decisive descriptor for $CB-e^-$ production amount and thus the reaction kinetics. Compared to the bulk g- C_3N_4 , the Ar treated samples obtained decreased CBEPs, which hindered the photocatalytic ozonation rates. In contrast, the upshifts of CBEPs enhanced the reductive potentials of $CB-e^-$, and improved the ability of bulk g- C_3N_4 surface to capture the O_3 molecules. Moreover, the upshifted CBEPs also resulted in enlarged band gaps, which in turn reduced the total amount of the photo-excited $CB-e^-$ and

the treatment efficiency. Therefore, the rational design of an efficient photocatalyst needs to fulfill the optimal balance between the reductive ability of $CB-e^-$ (governed by CBEP) and their quantity (governed by band gap) (Fig. 10b) [24]. Additionally, it has been also found that g- C_3N_4 nanosheet with exfoliated layers demonstrated a higher reactivity in photocatalytic ozonation than the bulk one, which was mainly ascribed to the large SSA and upshifted CBEP [24,37,143].

Exfoliation can increase the amount of surface active sites by enlarging the surface area, yet it fails to fundamentally increase the surface reactive sites with ozone. Wang et al. fabricated the g- C_3N_4 loaded with defective WO_3 heterojunction catalyst using melamine and tungsten acid as the precursors. The BIEF within this S-scheme heterojunction enhanced the production and separation of the photo-generated charge carriers and reserved the carriers with high redox potentials. The oxygen vacancies on WO_3 promoted the amount of the photo-excited $CB-e^-$ by elevating the work function WO_3 and thus creating an intensified BIEF. In addition, the surface defective sites on WO_3 also facilitated the adsorption of O_3 molecules for their subsequent evolution into $\cdot OH$. As the result, this g- C_3N_4 / WO_3 -induced photocatalytic ozonation increased the effective utilization rate of ozone to 80%, significantly enhancing the $\cdot OH$ production. Moreover, a 22-fold increase in the reaction rate for pollutant removal was obtained compared to the sole photocatalytic process. *In situ* electrochemical tests further proved that introducing O_3 to the photocatalytic reaction changed the $\cdot OH$ production route from the conventional three-electron one to the single-electron one, thereby significantly improving the $CB-e^-$ utilization [17]. In addition, mass transfer efficiency plays a crucial in photo- O_3 systems. Hydrophilic g- C_3N_4 is not favorable for O_3 adsorption and thus impact the mass transfer efficiency because of the hydrophobicity of O_3 . Hydrophobic sites can be constructed by doping halogens (F, Cl, Br, I) into the framework of g- C_3N_4 . The hydrophobic carbon-halogen bonds enhance the mass transfer of O_3 and increase the utilization of O_3 . Meanwhile, due to the different electronegativities, the introduction of halogens can redistribute the electrons on g- C_3N_4 , allowing carriers to be

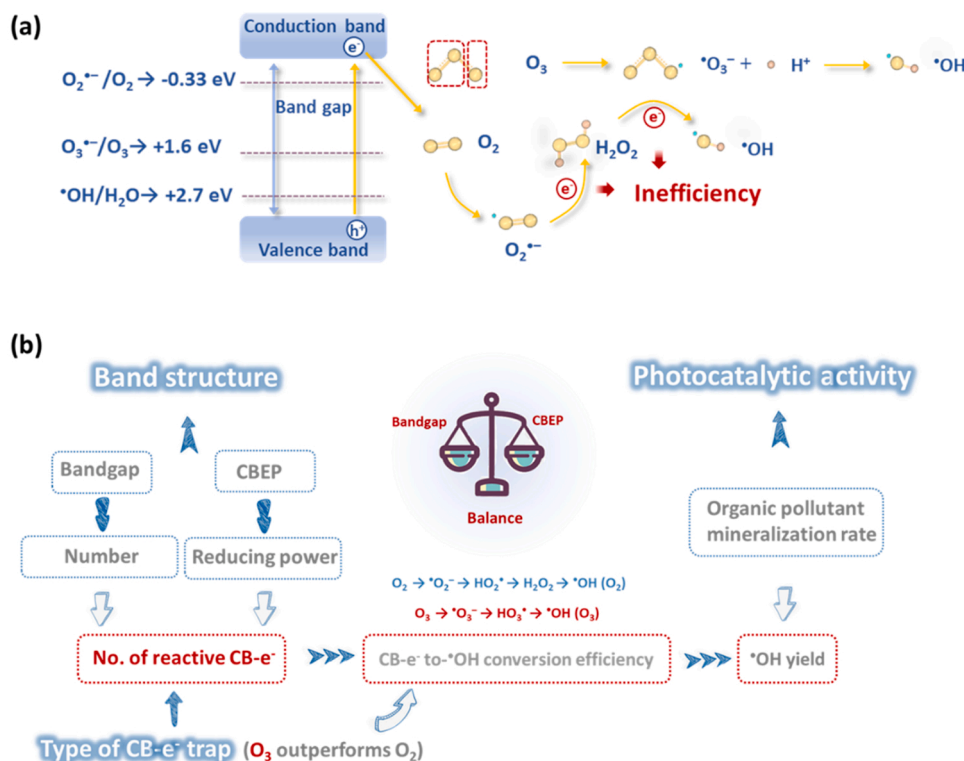


Fig. 10. (a) Schematic illustration of direct electron transfer regime in the photo- O_3 reaction; (b) Relationship among band structure, type of $CB-e^-$ trap, and photocatalytic activity. Adapted with permission from ref. [24]. Copyright 2020, American Chemical Society.

transferred between the s-type triazine rings and thus reducing their recombination rates [144].

To date, most of the studies on photocatalytic ozonation rely on the ultraviolet-light as the irradiation source, while only a few focus on the visible-light-induced reactions because of the low quantum yield of materials and the low utilization rate of sunlight. In the subsequent research, it is imperative to develop visible-light response semiconductors and construct the adsorptive/active sites for O_3 reactions. Meanwhile, the in-depth mechanistic insights into the synergistic effects between the photo-generated charge carriers and the O_3 -induced ROS should be clarified.

3.1.4. Photocatalysis coupled with other peroxides

Sodium percarbonate (SPC), as a solid carrier of H_2O_2 , has received increasing research attention in wastewater decontamination because of its convenience in storage and transportation and wide working pH [145]. In heterogeneous photo-SPC coupled system, SPC can be activated to generate $\bullet OH$ by photo-excited electrons on the catalyst surface via direct electron transfer regime. Li et al. found that SPC can be more easily activated than H_2O_2 to produce $\bullet OH$ by the photo-excited $CB-e^-$ from protonated g- C_3N_4 under visible light irradiation. G- C_3N_5 is a novel carbon nitride with a smaller bandgap (1.98 eV) compared to g- C_3N_4 , also receiving extensive attention in the environmental remediation field. In ultrathin g- C_3N_5 (U-g- C_3N_5)/SPC/Vis system, the performance of U-g- C_3N_5 was superior than that of g- C_3N_4 and g- C_3N_5 due to its excellent charge carrier separation ability. Therefore, SPC is a promising alternative to H_2O_2 in photocatalytic water treatment processes [130]. Also, periodate (PI) has emerged as a powerful peroxide for rapid pollution removal because it can be activated to generate strong oxidative species *in situ*, such as iodine radicals (IO_3^\bullet and IO_4^\bullet), $\bullet OH$, O_2^\bullet and 1O_2 . It was reported that PI can directly react with the photo-excited $CB-e^-$ from g- C_3N_4 to produce free radicals in g- C_3N_4 /PI/Vis system (Eqs. 12–13) [130].



3.2. Indirect electron transfer regime

In metal-modified g- C_3N_4 catalysts, the metal species which are anchored on or encapsulated in the g- C_3N_4 structure can directly activate the peroxy bonds within the peroxides by transferring their d orbital electrons into the O 2p orbitals of the peroxides. These metal species will be subsequently oxidized into the high-valence states. Nevertheless, the high-valence metal species are recalcitrant to be

reduced back into the low-valence states in the highly oxidative environment for the continuous peroxide activation and thus become the rate-determining steps. In peroxide-coupled photocatalytic process, the photo-excited $CB-e^-$ can activate the surface-adsorbed peroxides via the direct electron transfer process. Also, photo-excited $CB-e^-$ can react with high-valence metal species and reduce them back to their low-valence states for activity regeneration (Fig. 11). This indirect electron transfer regime between photo-excited electrons and the high-valence metal species ensures the continuous activation of the peroxides. In addition, the transition metal species as electron acceptors can inhibit recombination of the photo-excited charge carriers. Utilization efficiency of the photo-excited $CB-e^-$ in indirect electron transfer regime might be lower than that in the direct electron transfer regime because the electrons might be dissipated by the other electron acceptor or trapped within the defective structures in the catalysts during migrating across the catalyst surface. Furthermore, competitive reactions occur to the electrons between peroxides and the high valence metal species depending on their reaction rates as well as the affinities of the peroxides with catalyst surface and catalytic sites. Table 2 summarizes some of the reported indirect electron transfer mechanisms.

3.2.1. Photo-Fenton reaction

In photo-Fenton reactions governed by indirect electron transfer regime, the photo-excited $CB-e^-$ from the semiconductors reduces the high-valence Fe^{3+} into Fe^{2+} apart from directly activating H_2O_2 [131]. This redox reaction achieves the continuous supply of Fe^{2+} species, which guarantees the high H_2O_2 activation efficiency for $\bullet OH$ production and overcomes rate-determining step for Fe species regeneration [151,156,162]. Additionally, the optimum pH range for the reaction solution can be widely broadened with the participation of $CB-e^-$, and thus overcomes the technical bottlenecks of the conventional Fenton process. For g- C_3N_4 catalyzed photo-Fenton reaction, the lone-pair electrons of the N atoms of the triazine ring skeleton within the g- C_3N_4 structure offer ideal places to anchor metal species [147]. The anchored metal species then becomes the active sites for continuously activating H_2O_2 to produce ROS with the aid of photo-excited $CB-e^-$ [152,155]. Zhan et al. synthesized a single Fe atom doped g- C_3N_4 , in which Fe was fixed at the nitrogen vacancies of g- C_3N_4 . Under light illumination, photo-excited $CB-e^-$ was trapped by the engineered nitrogen vacancies, which was then accumulated at Fe single-atom sites. The formation of a highly concentrated electron density at the Fe single-atom sites significantly improved the H_2O_2 activation for $\bullet OH$ generation [157].

The adsorption and activation of H_2O_2 on g- C_3N_4 surface are two key factors influencing the reactivity of photo-Fenton reactions. Constructing bimetal oxide loading by tuning their loading density can achieve the optimal adsorption and activation of H_2O_2 and thus high reactivity

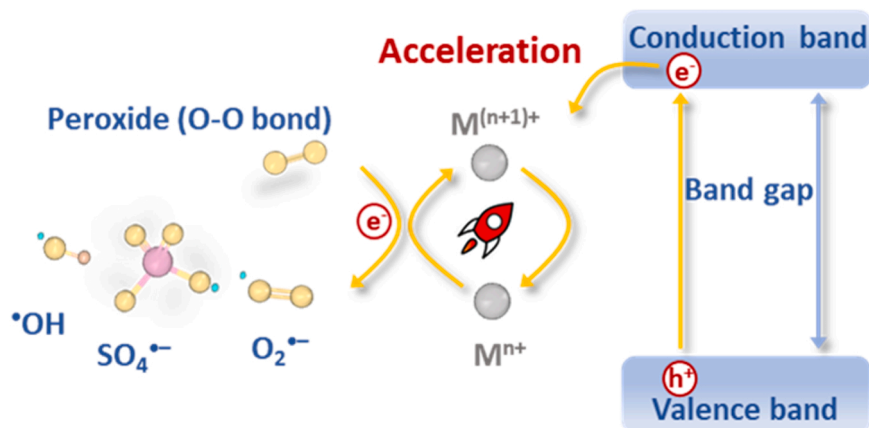


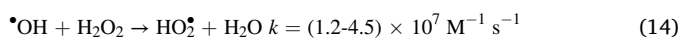
Fig. 11. Schematic illustration of indirect electron transfer regime.

Table 2

Summary of indirect electron transfer regime in carbon nitride-triggered photocatalysis coupled with peroxides.

Catalysts name	Main active species	Target pollutant	Peroxide dose	degradation efficiency	Activation system	Ref
Cu-HNCN	$\bullet\text{OH}$, h^+ , O_2^-	tetracycline 10 mg/L	20 mM	50 min 96%	Vis/ H_2O_2 /g- C_3N_4	[146]
Fe-g- C_3N_4	$\bullet\text{OH}$	rhodamine B 10 mg/L tetracycline 20 mg/L	30 wt%	60 min 98.2% 120 min 98.7%	Vis/ H_2O_2 /g- C_3N_4	[147]
FeOOH QDs/g- C_3N_4	$\bullet\text{OH}$	methylene orange 20 mg/L	10 mM	60 min 100%	Vis/ H_2O_2 /g- C_3N_4	[148]
Fe_3O_4 @ β -CD/g- C_3N_4	$\bullet\text{OH}$	polychlorinated biphenyls 0.5 mg/L	30 wt%	55 min 77%-98%	Vis/ H_2O_2 /g- C_3N_4	[149]
Fe-CN/P	$\bullet\text{OH}$	tetracycline hydrochloride 20 mg/L	5 mM	60 min 98.0%	Vis/ H_2O_2 /g- C_3N_4	[150]
MLD/CN/ Fe_3O_4	$\bullet\text{OH}$	tetracycline 20 mg/L	80 mM	80 min 95.8%	Vis/ H_2O_2 /g- C_3N_4	[118]
Fe-g- C_3N_4 /WO ₃	$\bullet\text{OH}$	p-nitrophenol 10 mg/L	5 mM	4 h 91.0%	Vis/ H_2O_2 /g- C_3N_4	[151]
Fe-g- C_3N_4	$\bullet\text{OH}$	phenol 20 mg/L	8 mM	50 min 100%	Vis/ H_2O_2 /g- C_3N_4	[152]
SA-TM/PN-g- C_3N_4	$\bullet\text{OH}$	bisphenol A 10 mg/L	165 μM	70 min 74.4-99.5%	Vis/ H_2O_2 /g- C_3N_4	[153]
Bio-SA-Fe/g- C_3N_4	O_2^- , $\bullet\text{OH}$	sulfamethoxazole 20 mg/L	20 mM	40 min 99.6%	Vis/ H_2O_2 /g- C_3N_4	[154]
Fe-POM/CNNS- N_{vac}	$\bullet\text{OH}$, O_2^- , $^1\text{O}_2$	tetracycline hydrochloride 20 mg/L	10 mM	18 min 96.5%	Vis/ H_2O_2 /g- C_3N_4	[155]
U-g- C_3N_4 /Fe-POMs	$\bullet\text{OH}$	methyl blue 10 mg/L	30 mM	80 min 100%	Vis/ H_2O_2 /g- C_3N_4	[156]
Fe ₁ -Nv/CN	$\bullet\text{OH}$	ciprofloxacin 10 mg/L	10 μL	60 min 91%	Vis/ H_2O_2 /g- C_3N_4	[157]
Fe-g- C_3N_4 /Bi ₂ WO ₆	O_2^- , $^1\text{O}_2$	tetracycline 10 mg/L	1 mM	120 min 93.9%	Vis/ H_2O_2 /g- C_3N_4	[108]
Zn _{1-1.5x} Fe _x S/g- C_3N_4	$\bullet\text{OH}$	p-nitrophenol 10 mg/L	1 mM	60 min 96%	Vis/ H_2O_2 /g- C_3N_4	[109]
g- C_3N_4 /PDI/Fe	O_2^- , $\bullet\text{OH}$	p-nitrophenol 10 mg/L	-	1 h 80%	Vis/ H_2O_2 /g- C_3N_4	[158]
UPCN/FeOOH	O_2^- , $\bullet\text{OH}$	oxytetracycline 20 mg/L	-	120 min 86.23%	Vis/ H_2O_2 /g- C_3N_4	[159]
R-gCPF	$\bullet\text{OH}$	benzoic acid 10 mg/L	-	3 h 100%	Vis/ H_2O_2 /g- C_3N_4	[160]
OPCN	$\bullet\text{OH}$	2,4-dichlorophenol 5 mg/L	-	60 min 98.37%	Vis/ H_2O_2 /g- C_3N_4	[161]
F-BN	O_2^- , $\bullet\text{OH}$	Amoxicillin 20 mg/L	-	30 min 93%	Vis/ H_2O_2 /g- C_3N_4	[162]
g- C_3N_4 /ZnFe ₂ O ₄ /Bi ₂ S ₃	$\bullet\text{OH}$, O_2^- , $\text{SO}_4^{\bullet-}$, h^+	2,4,6-trichlorophenol 50 mg/L	1 g/L	60 min 98.9%	Vis/PMS/g- C_3N_4	[163]
MCN	O_2^- , $^1\text{O}_2$	tetracycline 20 mg/L	0.2 g/L	30 min 86.7%	Vis/PMS/g- C_3N_4	[90]
g- C_3N_4	$\text{SO}_4^{\bullet-}$	acid orange 7 10 mg/L	0.4 g/L	25 min 100%	Vis/PMS/g- C_3N_4	[164]
SA-Co-CN/g- C_3N_4	$\bullet\text{OH}$	norfloxacin 20 mg/L	0.4 g/L	30 min 100%	Vis/PMS/g- C_3N_4	[85]
Ag/AgCl@ZIF-8/g- C_3N_4	O_2^- , $\text{SO}_4^{\bullet-}$, h^+	levofloxacin 10 mg/L	2 mM	60 min 87.3%	Vis/PMS/g- C_3N_4	[165]
CNC	O_2^- , $^1\text{O}_2$, h^+	paracetamol 10 mg/L	0.5 mM	40 min 100%	Vis/PDS/g- C_3N_4	[166]
CN-CeO ₂	h^+	bisphenol A 0.1 mM	0.2 mM	60 min 94.2%	Vis/PDS/g- C_3N_4	[167]
g- C_3N_4	O_2^- , $\text{SO}_4^{\bullet-}$, h^+	sulfamethoxazole 10 μL	0.5 mM	60 min 98.4%	Vis/PDS/g- C_3N_4	[168]
N-CQDs/g- C_3N_4	O_2^- , $\text{SO}_4^{\bullet-}$, h^+	tetracycline hydrochloride 20 mg / L	0.6 g/L	60 min 90%	Vis/PDS/g- C_3N_4	[169]
CuFe ₂ O ₄ /g- C_3N_4	$\bullet\text{OH}$, O_2^- , $\text{SO}_4^{\bullet-}$, h^+	propranolol 0.02 mM	0.2 mM	120 min 56.5%	Vis/PDS/g- C_3N_4	[129]
CCN	Co(IV)	sulfamethoxazole 10 μM	02 mM	30 min ~100%	Vis/PAA/g- C_3N_4	[170]

[171]. Liu et al. integrated Cu-Fe bi-metal oxides on g- C_3N_4 and used it as photo-Fenton catalyst for tetracycline degradation. Both experimental and DFT simulation results revealed that the involvement of CuO_x upshifted the d band center of the pristine g- C_3N_4 . The elevated antibonding energy level enhanced the adsorption strength of H_2O_2 , while Fe sites promoted the activation of H_2O_2 . Additionally, the accelerated electron transfer by the bi-metal loading facilitated the transport of the photo-excited charge carriers. The achieved synergies of adsorption-catalytic degradation and photocatalysis-Fenton oxidation resulted in a significant improvement in pollutant removal efficiency. Noted that H_2O_2 will be protonated when the solution pH is too low (<2), which will act as a scavenger of $\bullet\text{OH}$ and inhibit the reaction rate (Eq. 14) [172]. The elevated pH will transform Fe^{2+} into ferrous hydroxide with low solubility, resulting in declined performances in photo-Fenton reactions [173].



3.2.2. In situ photo-Fenton (without H_2O_2 addition) reaction

The CB potential of g- C_3N_4 surpasses oxygen reduction potential

(-1.3 vs. -0.33 V_{NHE}) and allows the H_2O_2 evolution via the two-step single electron transfer process (Eqs. 2–3) or a single-step two electron transfer process (Eq. 15) during visible light irradiation [160,174]. Moreover, the mild VB potential (+1.4 V_{NHE}) of g- C_3N_4 prevents the further oxidation of H_2O_2 . Thus, the *in situ* generated H_2O_2 can be accumulated and consumed by metal species anchored on or encapsulated in g- C_3N_4 via photo-Fenton reactions for ROS generation (Fig. 12) [109,175,176]. Although the amount of *in situ* generated H_2O_2 by g- C_3N_4 -induced photocatalytic reactions might be insufficient to trigger fast degradation kinetics, the utilization efficiency of the dissolved ground-state stable O_2 can be significantly improved by exciting it into ROS for pollutants removal [153,159].



Pristine g- C_3N_4 obtains a low yield of H_2O_2 by photocatalytic conversion because of its narrow light absorption range, rapid charge carrier recombination, and the sluggish surface reaction rates [177–179]. Surface engineering has been applied to g- C_3N_4 to increase the H_2O_2 yield to solve the as-mentioned issues, such as bandgap regulation, light path optimization, morphology tuning, defect engineering, and hybridization with other semiconductors [180–182], yet the low selectivity

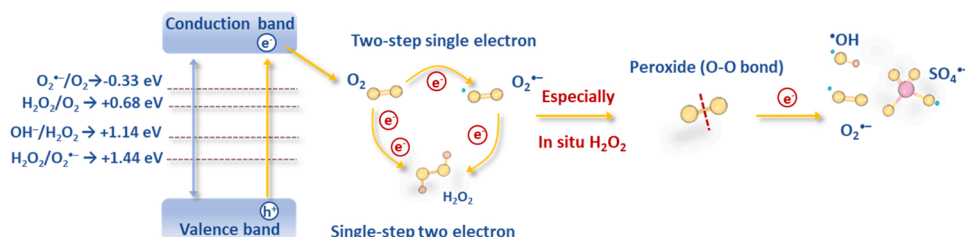
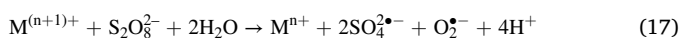
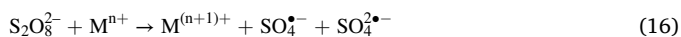


Fig. 12. Schematic illustration of *in situ* generated H_2O_2 and subsequent reactions.

of the O₂ reduction and the fast H₂O₂ self-consuming are still the main bottlenecks affecting the photocatalytic H₂O₂ production efficiency. In future studies, it is promising to regulate the *in situ* H₂O₂ production route from the two-step single electron O₂ reduction to the single-step two electron transfer one by enhancing the utilization efficiency of CB-e⁻ [58].

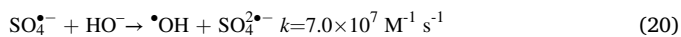
3.2.3. Photo-persulfate reaction

Similar to photo-Fenton reactions, transition metal doping has been acknowledged as a promising strategy to enhance the reactivity of g-C₃N₄ in photo-persulfate reaction via the indirect electron transfer regime (Eqs. 16–17) [129,183]. Transition metals with empty d orbitals and proper atomic radius are favorable to be integrated within g-C₃N₄ to induce a boost in catalytic activity. Integration of transition metal species increases the separation efficiency of charge carriers and activates persulfates by injecting d orbital electrons of the metal species, while the photo-excited CB-e⁻ ensures the fast redox cycle of Mⁿ⁺¹/Mⁿ⁺, achieving fast kinetics for persulfate activation [184].



Carbon nitrides integrated with metal-SACs have recently emerged as the efficient catalysts and can greatly enhance the activities because of the maximized atomic exposure of the active sites [85]. Moreover, the biased distribution of electron density and accelerated electron transfer further promote the adsorption of the peroxides and their subsequent activation. Zhao et al. synthesized a highly efficient single-atom Fe-dispersed g-C₃N₄ catalyst (SAFe-MCN) with Fe-N₄ as the dominant coordination structure for visible-light PMS activation [185]. During the reaction, PMS was activated at the ≡Fe(II) site of SAFe-MCN to generate SO₄^{•-}. Meanwhile, photo-excited VB-h⁺ further oxidized the O₂^{•-} as the reaction intermediate to form ¹O₂. The turnover frequency (TOF) of this SAFe-MCN induced photo-PMS reaction for sulfamethoxazole degradation was 5.27 min⁻¹, which was 2–6 orders of magnitude higher than normal Fe-containing catalysts for SMX degradation. Similarly, cobalt and phosphorus co-doped g-C₃N₄ enhanced the light absorption, charge separation, and the adsorption of PDS compared to pristine g-C₃N₄. The d-π conjugated structure via coupling the d orbital of cobalt with the large π electrons in the tris-s-triazine ring of g-C₃N₄ accelerated the redox cycle of Co³⁺/Co²⁺. The chemical-catalytic driven PDS activation was thus promoted by the rapid regeneration of Co²⁺ [84].

Concentration of dissolved oxygen (DO) can also affect the pathway for persulfate activation. At a low DO concentration range (~0.5 mg/L), PMS activation favored the direct electron transfer pathway to receive electrons from the photo-excited CB-e⁻. However, DO in high concentration (~8 mg/L) would compete against PMS for CB-e⁻ consumption. Therefore, a large amount of O₂^{•-} was formed which hindered the direct electron transfer pathway for PMS activation. The produced O₂^{•-} could further react with PMS for SO₄^{•-} to initiate an indirect electron transfer pathway for PMS activation (Eqs. 7, 18–20) [124].



3.2.4. Photocatalysis coupled with other peroxides

Peracetic acid (PAA) can be indirectly activated by electrons generated from the redox cycle of the transition metal species anchored on g-C₃N₄. PAA can be activated via the Fenton-like mechanism [186]. However, similar to the Fenton reactions, the reduction rate of the high-valence metal to the low valence one is usually slow and hinders the rapid and continuous production of free radicals [187]. The

involvement of photo-excited CB-e⁻ greatly accelerates the reduction of the high-valence metal species and promotes the redox recycle of the transition metals for providing continuous electrons for PAA activation. Liu et al. fixed Co(II) species into the nitrogen pots of g-C₃N₄ for photocatalytic PAA activation. They revealed that the PAA molecules could be firmly adsorbed on Co(II) sites and converted Co(II) into Co(IV) through a unique two electron transfer mechanism, enabling the highly electrophilic high-valent cobalt-oxo species [Co(IV)] as the dominant non-radical species for degradation of various sulfonamides [170]. The as-produced non-radical Co(IV) species endowed this catalytic system with excellent anti-interference capacity and achieves satisfactory decontamination performance in practical water treatment scenarios.

3.3. External electrons injection regime

3.3.1. Dye sensitization effect

Dye sensitization has been widely applied as a strategy to extent light-absorbing ability of the semiconductors with the aid of organic dyes [188]. The anchored dye molecules receive visible and even near-infrared light and electrons can be excited from their highest occupied molecular orbital (HOMO) to the lowest unoccupied molecular orbital (LUMO) (Fig. 13). These photo-excited electrons will experience cascaded electron transfer process from LUMO of the excited dye to CB of the semiconductor when CBM of semiconductor is positioned lower than LUMO of the dye. The positively charged dye molecules can be then regenerated by accepting electrons from the sacrificed electron donor or be degraded. In this way, electrons excited from the dye molecules play critical roles in ROS generation while the semiconductor acts as a medium facilitating the migration of electrons.

For g-C₃N₄-based catalysts, although their relatively small bandgaps can absorb visible light (2.7 eV, λ < 460 nm), most of the visible-near-infrared (vis-NIR) photons in the solar spectrum cannot be utilized. Therefore, attaching dye molecules that are photosensitive to vis-NIR photons to the g-C₃N₄-based catalysts is a promising strategy to extend the light absorption ability. Moreover, the extra photo-excited electrons from the dye sensitization effect can also be used to induce the direct electron transfer process. Metal-phthalocyanine composites, especially the Fe-phthalocyanines, obtain intrinsic broad spectral response in the red/near-infrared and visible-light regions, which have been applied widely in the photocatalytic applications. Wu et al. employed iron hexadecachlorophthalocyanine (FePcCl₁₆) to coordinate with g-C₃N₄ and used for photo-persulfate activation for degradation of pharmaceuticals. Compared to the pristine g-C₃N₄, the FePcCl₁₆-modified g-C₃N₄ extended the spectral response over the entire visible light region. Upon visible light irradiation, the photo-excited electrons from the excited state of FePcCl₁₆ (*FePcCl₁₆) migrated to CB of g-C₃N₄, which were further captured by PMS for SO₄^{•-} and •OH formation. Meanwhile, it was found that *Fe(II) ions in FePcCl₁₆ were axially coordinated with O atoms in PMS. The cleavage of the peroxy bonds resulted in the formation of highly active nonradical Fe(IV)=O species, which also contributed to the degradation of organic pollutants [189]. In an effective dye sensitization process, the intimate contact between the dye molecules and the surface of the semiconductor is of vital significance to maximize the interfacial electron transfer rate. The short lifetime of the photo-excited electrons from the HOMO of photosensitizers will be recombined before the dye molecules diffuse onto the surface of the semiconductor in a loose contact system. The negatively charged N and C vacancies within g-C₃N₄ structures can attract the positively charged dye such as ruthenium tris (bipyridine) and polypyridine complexes through electrostatic force [190,191]. The pH of the aqueous reaction solution as well as its ionic strength brought by the existence of inorganic anions can affect the dye adsorption stability by affecting the electrostatic force, hydrogen bonding, and/or physical entrapment [192]. In actual practice, the usage of the dye sensitization effect to boost the reactivity might be limited by the environmental parameters.

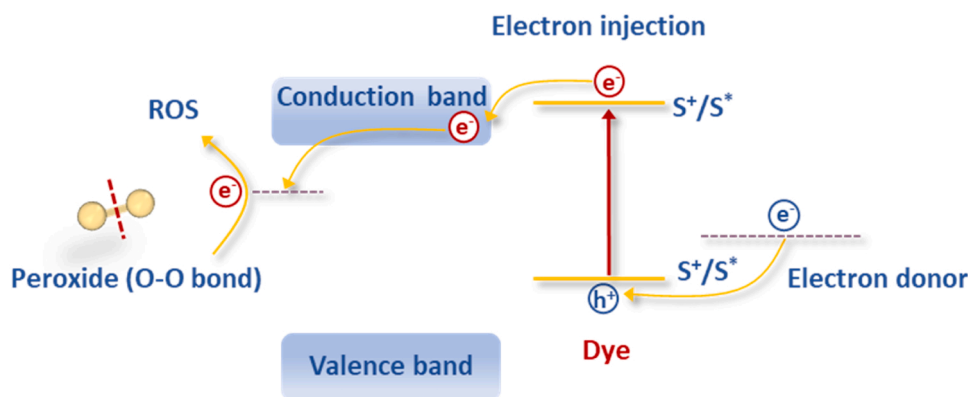


Fig. 13. Schematic illustration of dye sensitization effect in peroxide-coupled photocatalysis.

3.3.2. Quantum dot confinement effect

Like dye sensitization, hybridization of quantum dots (QDs) on g-C₃N₄ can also broaden its light absorption ability and provide the extra photo-excited electrons for ROS generation owing to the quantum confinement effect [193,194]. In addition, the band structure of the QDs can be easily manipulated by adjusting the QD size to fit the attached semiconductors. To induce a cascaded electron transfer process and increase the utilization efficiency of photo-generated electrons, CB of the QDs is preferably situated above the CBM of the attached semiconductors (Fig. 14). The unique up-conversion performance and the large number of coordination unsaturated N sites of g-C₃N₄ provide the ideal hosts for anchoring quantum dots. Both metal-based and metal-free quantum dots have been successfully anchored on g-C₃N₄ and used for peroxide-coupled photocatalytic process for pollutants decontamination [195–197]. For example, Du and coworkers found that the integration of Fe₂O₃ quantum dots with a diameter of 2 nm on g-C₃N₄ nanosheets greatly extended visible light absorption ability from 450 to 1000 nm [198]. In addition, the strong interfacial coupling between the Fe₂O₃ quantum dots and g-C₃N₄ constructed a highway for electron transportation, which greatly shortened the charge transition distance and accelerated the separation and transfer of the photo-generated charge carriers [199,200]. As a result, the composite photocatalysts obtained high activities in p-nitrophenol degradation because of the promoted the synergy between the photocatalytic and chemical activation of H₂O₂.

3.3.3. Localized surface plasmon resonance (LSPR) effect

Integrating metal nanoparticles with LSPR effect is another strategy to mitigate the limited visible light absorption of wide bandgap photocatalysts [201,202]. LSPR effect is an optical phenomenon occurring in the noble metal species, in which a sharp spectral absorption together

with the intense electric fields will be generated when the frequency of incident photons matches resonance of the electron cloud on metal nanoclusters [203]. Under light illumination, the localized electromagnetic energy created by the generated resonant surface plasmons can excite the hybridized semiconductor to produce the charge carriers and the excited electron/hole pairs formed in the near-surface region of the semiconductor shorten the diffusion length (Fig. 15a) [204]. Furthermore, the contact potential difference at metal nanocluster/semiconductor interfaces drives the mobility of the charges. Noble metals such as Au and Ag have been integrated with g-C₃N₄ to induce the LSPR effect to boost the generation of charge carriers and achieved satisfied peroxide activation efficiency [205]. However, the high cost and the low light absorption ability of the noble metals hinders their broad application. Recently, 0D Cu_{2-x}S nanodots were hybridized with g-C₃N₄ nanosheets (CSCNNs) by a one-step hydrothermal method. Compared with Ag and Au hybridized counterparts, CSCNNs obtained a more intensive LSPR effect in NIR region, which greatly promoted the charge separation and transfer (Fig. 15b) [206]. The photo-excited CB-e⁻ can transfer O₂ into O₂^{•-}, then H₂O₂ would form with the further reduction of O₂^{•-}. Afterwards, H₂O₂ decomposes to [•]OH in the presence of electrons and participates in the degradation of pollutants.

3.3.4. Ligand-metal charge transfer effect

Different from the dye sensitization in which dye molecules absorb light, the ligands themselves do not absorb visible light. On the contrary, these ligands can adsorb on the catalyst surface by forming photosensitive ligand-metal complexes, which absorb light and produce photo-excited electrons [207]. This ligand-metal charge transfer (LMCT) process ensures the rapid regeneration of photosensitive metals and the continuous production of ROS by the photo-excited electrons from the HOMO of the metal-ligand complex (Fig. 16a) [208]. Additionally, a

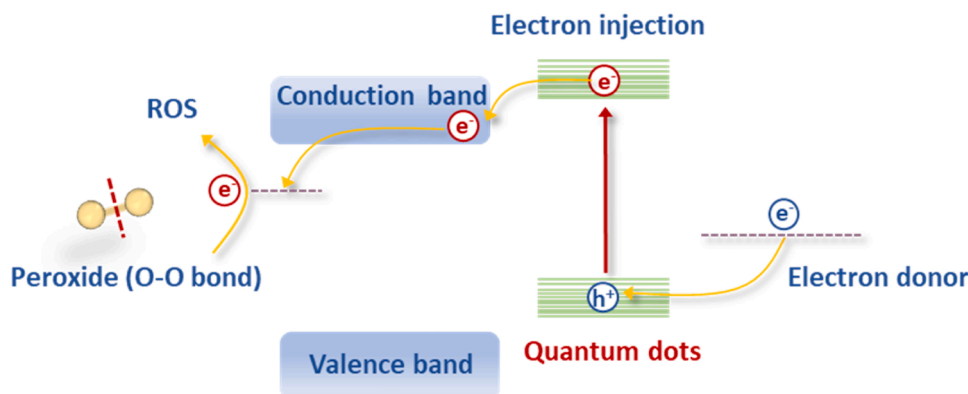


Fig. 14. Schematic illustration of quantum dot confinement effect in peroxide-coupled photocatalysis.

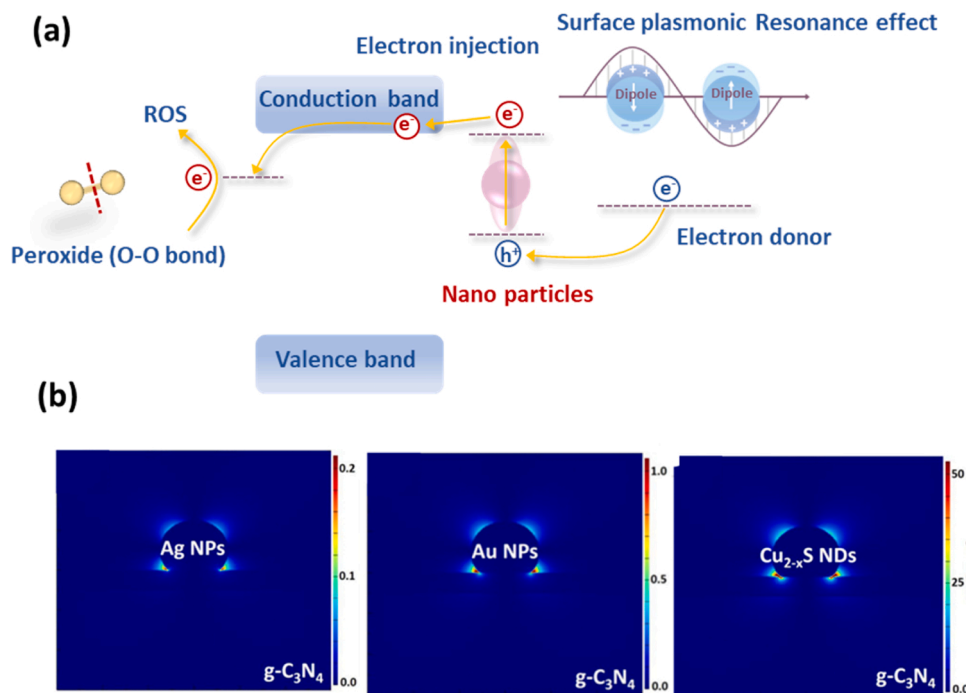


Fig. 15. (a) Schematic illustration of localized surface plasmon resonance effect in peroxide-coupled photocatalysis; (b) Electromagnetic field intensity distributions images of Ag nanoparticle-loaded g-C₃N₄ nanosheets (AgCNNs-8), Au nanoparticle-loaded g-C₃N₄ nanosheets (AuCNNs-8) and 0D/2D plasmonic Cu_{2-x}S/g-C₃N₄ nanosheets (CSCNNs-8) simulated by finite-difference time-domain analysis. Cited with permission from ref. [206]. Copyright 2019, Elsevier.

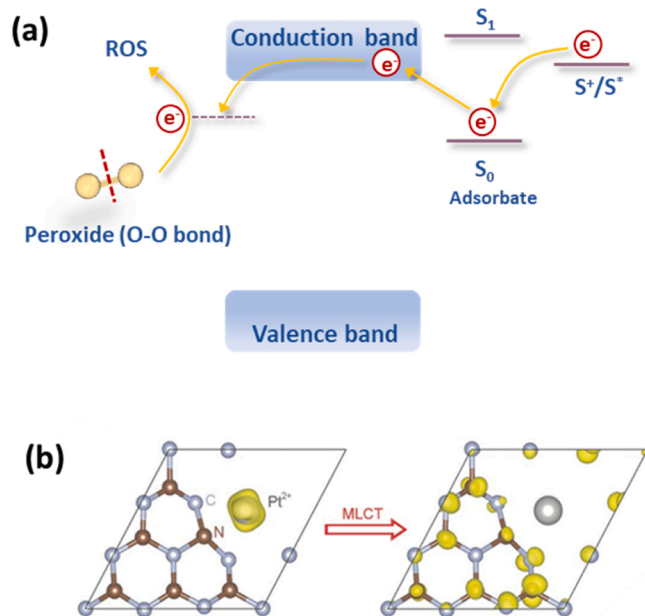
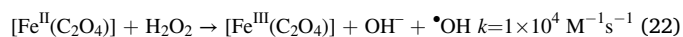
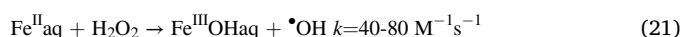


Fig. 16. (a) Schematic illustration of ligand-metal charge transfer effect in peroxide-coupled photocatalysis; (b) Photoexcited charge density transition from the Pt²⁺-induced hybrid HOMO to the LUMO of g-C₃N₄-Pt²⁺. Cited with permission from ref. [210]. Copyright 2016, Wiley-VCH.

variety of organic or inorganic compounds (even cannot absorb visible light) with an appropriate HOMO level can serve as potential LMCT sensitizers because electrons transfer from HOMO of the attached ligand to CB of the semiconductor (Fig. 16b) [209,210]. Theoretically, the LMCT process constructs a directional electron transfer channel between g-C₃N₄ and metal atoms and redistributes the localized electrons during the charge transfer process, thus affecting the reaction kinetics of charge

carriers. Mao et al. prepared Fe-doped g-C₃N₄ and used for photo-Fenton oxidation of Rhodamine B [211]. The visible light induced LMCT process transferred the photo-excited CB-e⁻ from g-C₃N₄ to Fe (III)-N moieties and reduced them to Fe(II)-N moieties, which facilitated the H₂O₂ activation. In addition, the presence of complexing agents limits Fe(III) precipitation at near neutral pH [212,213]. Thus, no acidification is required for the complement of Fenton-like water treatment. Apart from the additionally added complexing agents, the anchored functional groups on g-C₃N₄-based semiconductors (such as -NH₂) can also trigger LMCT effect to boost the generation of excited electrons [208]. The formed metal-ligand complexes can also enhance the activation of the peroxides. Formation of FeII(C₂O₄) complex by adding oxalic acid as the complexing agent can greatly accelerate the reaction rate with H₂O₂ for •OH production (Eqs. 21–22) [214].



In an effective external injected electron transfer regime, the intimate contact between the exogenic semiconductors and the surface of the g-C₃N₄ is of vital significance to maximize interfacial electron transfer rate. In actual practice, the usage of the dye sensitization effect to boost the reactivity might be limited by the environmental parameters. Table 3 summarizes some of the reported peroxide-coupled heterogeneous photocatalysis in external electrons injection regime.

Fig. 17 lists the comparison of these three electron transfer regimes possibly occurring in peroxide-coupled heterogeneous photocatalytic reactions and the design principles of the active functional g-C₃N₄ semiconductors towards these types of reaction regimes. Direct electron transfer regime is an effective pathway for peroxide activation with high electron utilization efficiencies. The surface adsorbed peroxides can directly receive the photo-excited electrons and evolve into ROS for pollutants degradation. And their fast reaction kinetics further achieve the efficient separation of the photo-excited charge carriers and boost their production. These require the construction of the surface active sites on g-C₃N₄ for tight peroxides adsorption by doping/vacancy

Table 3

Summary of external electrons injection regime in carbon nitride-triggered photocatalysis coupled with peroxides.

Catalysts name	Main active species	Target pollutant	Peroxide dose	degradation efficiency	Activation system	Ref
Dye sensitization						
D35-TiO ₂ /g-C ₃ N ₄	[•] OH	bis-phenol A 10 mg/L	2 mM	15 min 100%	Vis/PMS/g-C ₃ N ₄	[215]
FeCN	O ₂ ^{•−} , ¹ O ₂	sulfamethoxazole 10 mg/L	1 mM	35 min 90.94%	Vis/PMS/g-C ₃ N ₄	[188]
g-C ₃ N ₄ -IMA-FePcCl ₁₆	O ₂ ^{•−} , ¹ O ₂	carbamazepine 25 μM	0.3 mM	25 min 94%	Vis/PMS/g-C ₃ N ₄	[216]
Quantum dot confinement						
Fe ₂ O ₃ QD/g-C ₃ N ₄	[•] OH	p-nitrophenol 20 mg/L	30 wt%	10 min 100%	Vis/H ₂ O ₂ /g-C ₃ N ₄	[206]
BPTCN	O ₂ ^{•−} , h ⁺	oxytetracycline hydrochloride 10 mg/L	-	60 min 81.05%	Vis/H ₂ O ₂ /g-C ₃ N ₄	[193]
CD-rGO-O-g/C ₃ N ₄	O ₂ ^{•−}	lincomycin 100 mg/L	-	90 min 99%	Vis/H ₂ O ₂ /g-C ₃ N ₄	[217]
CuFeO QDs/CNNSs	O ₂ ^{•−} , ¹ O ₂	tetracycline 50 mg/L	100 mM	25 min 99.8%	Vis/H ₂ O ₂ /g-C ₃ N ₄	[171]
MM SC-QDs	O ₂ ^{•−} , ¹ O ₂ , h ⁺	norfloxacin 10 mg/L	15 mM	20 min 99.9%	Vis/H ₂ O ₂ /g-C ₃ N ₄	[218]
NCDs/TCN	O ₂ ^{•−} , h ⁺	sulfamethoxazole 5 mg/L	1 g/L	60 min 100%	Vis/PMS/g-C ₃ N ₄	[219]
Ag/CNQDs@Fe ₃ O ₄	SO ₄ ^{•−} , [•] OH	capecitabine 5-fluorouracil 50 μM	0.5 mM	60 min 97.6%/99.5%	Vis/PMS/g-C ₃ N ₄	[194]
Localized surface plasmon resonance						
Ag/CNQDs@Fe ₃ O ₄	SO ₄ ^{•−} , [•] OH	capecitabine 5-fluorouracil 50 μM	0.5 mM	60 min 97.6%/99.5%	Vis/PMS/g-C ₃ N ₄	[194]
Ag/mpg-C ₃ N ₄	O ₂ ^{•−} , h ⁺ , SO ₄ ^{•−}	bisphenol A 20 mg/L	1 mM	60 min 100%	Vis/PMS/g-C ₃ N ₄	[205]
Ag@U-g-C ₃ N ₄ -NS	O ₂ ^{•−} , h ⁺	methylene blue phenol 10 mg/L	-	40 min 88.5% 80 min 89%	Vis/H ₂ O ₂ /g-C ₃ N ₄	[220]
Ligand-metal charge transfer						
g-C ₃ N ₄	SO ₄ ^{•−} , [•] OH, O ₂ ^{•−} , ¹ O ₂	metronidazole 0.02 mM	1 mM	18 min 74.2%	Vis/PMS/g-C ₃ N ₄	[207]
FeSA/CN	O ₂ ^{•−} , [•] OH	oxytetracycline 10 mg/L	-	60 min 78.7%	Vis/H ₂ O ₂ /g-C ₃ N ₄	[221]
g-C ₃ N ₄ /PDI@MOF	[•] OH	tetracycline 50 mg/L	10 mM	60 min 90%	Vis/H ₂ O ₂ /g-C ₃ N ₄	[222]
g-C ₃ N ₄ /NH ₂ -MIL-88B(Fe)	[•] OH	methylene blue 60 mg/L	100 μL	120 min 100%	Vis/H ₂ O ₂ /g-C ₃ N ₄	[208]

engineering or heterojunction formation. Additionally, a high valence band edge position of functional g-C₃N₄ is favorable to thermodynamically accelerate the redox reactions between photo-excited electrons and the adsorbed peroxides. In indirect electron transfer regime relying on the incorporated transition metal species on g-C₃N₄ as the mediators for peroxide activation, photo-excited electrons reduce the high-valence metal species after peroxide activation to ensure the continuous catalytic production of ROS rather than directly reacting with the peroxides. However, photo-excited electrons can be dissipated by other electron acceptors or trapped in defective structures in g-C₃N₄ and result in a low electron utilization efficiency. Therefore, indirect electron transfer regime demands the integration of highly active transition metal species in single-atom, nanocluster, or heterojunction forms on g-C₃N₄ to induce the redox reactions with the photo-excited electrons. Moreover, high stability of the incorporated transition metal species is necessary to avoid the secondary pollution caused by metal leaching issues. For external electron injection regime, photo-excited electrons are generated on the semiconducting ligands or organics that are closely fitted on the g-C₃N₄ and are cascade transported to the valence band of the g-C₃N₄ for peroxide activation. To achieve fast and efficient electron transfer, sophisticated catalyst design for the perfect match of the band structures is required to achieved the cascade electron transfer from the anchored semiconductive species to the g-C₃N₄. Nevertheless, the electrons might be trapped and dissipated in the electron-accepting structures of the functional g-C₃N₄ during transportation. Moreover, the pH and background substances such as inorganic anions and NOMs in wastewater can weaken the tight interaction between the anchored semiconducting materials and the g-C₃N₄. Noteworthy that in actual

peroxide-coupled heterogeneous photocatalytic reaction, the as-mentioned three electron transfer regime may co-exist because of the complexity of the catalyst structures.

4. Conclusions and future outlooks

In summary, this review focuses on introducing different engineering strategies to enhance the activity of g-C₃N₄-based materials and clarifying possible electron transfer regimes existed for peroxide activation and ROS generation in peroxide-coupled photocatalytic reactions. Depending on the electron transportation pathways and the sources of the photo-excited electrons, electron transfer regimes for peroxide activation towards ROS production are categorized into direct electron transfer regime, indirect electron transfer regime, and external electron injection regime. And to achieve the optimal electron transfer rate, regulation strategies such as morphology and defect control, heteroatom doping, heterojunction engineering, and organic compound hybridization can be applied to the pristine g-C₃N₄. Although some inspiring outcomes have been achieved in catalysts design and mechanistic investigation, challenges and opportunities for the future research still exist in the aspects of the optimization of the activity and stability of the g-C₃N₄-based materials, in-depth mechanistic study, and practical applications. Based on recent progress, some critical views, and suggestions for future research opportunities in the peroxide-coupled photocatalytic system are listed as follows.

(1) To modulate the redox potential of the photo-excited charge carriers and to achieve their spatial separation, various S-scheme heterojunctions have been constructed by hybridizing metal-based

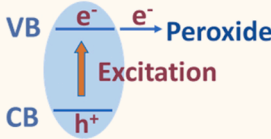
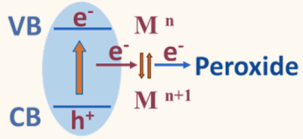
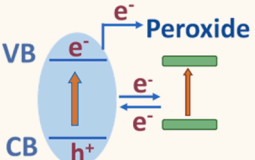
Electron Transfer Regime	Engineering Strategies	Pros and Cons
Direct electron transfer 	Increasing Surface Active Site (Porous/Exfoliation/Defects)	<div>pros</div> <ul style="list-style-type: none"> ● Avoidance of transformation of metal species in different valence states ● Fast reaction kinetics <div>cons</div> <ul style="list-style-type: none"> ● Fast carrier recombination
Indirect electron transfer 	Integrating Transition Metal Species (Doping)	<div>pros</div> <ul style="list-style-type: none"> ● Transition metal species as electron acceptors can inhibit electron-hole recombination ● Relies on redox cycles of transition metal species ● Possible secondary contamination <div>cons</div>
External electrons injection 	Compositing Other Semiconductor (Hybridizing Organic Compound)	<div>pros</div> <ul style="list-style-type: none"> ● High-speed electron transfer ● Complex structures may reduce electron utilization ● Complex structures may be affected by water quality conditions <div>cons</div>

Fig. 17. Comparisons of different electron transfer regimes in peroxide-coupled photocatalysis.

semiconductors with $g\text{-C}_3\text{N}_4$. In these heterojunctions, the highly reductive CB-e^- is enriched on the side of $g\text{-C}_3\text{N}_4$, while the oxidative VB-h^+ is accumulated on the hybridized semiconductor. Defect engineering is often performed on these hybridized metal-based semiconductors to increase the activity with peroxides. However, the average valence state of the metal atoms in the ambient of defective sites is lower than that in the bulk structure, making these metal atoms act as the electron donor and highly vulnerable to be oxidized by the produced VB-h^+ and the peroxides. Furthermore, high concentration of structural defects can trap the charge carriers and break the structural robustness. Additionally, the diffusion of the peroxide from the solution bulk onto the catalyst surface is much slower than the surface migration of the VB-h^+ . In this manner, the photo-excited VB-h^+ with high oxidation potential can be quickly consumed by the defective sites, rather than direct oxidizing the pollutants or for hydroxyl radical generation. Therefore, to make full use of the photo-excited charge carriers with high redox potentials, prudent surface engineering should be performed on the $g\text{-C}_3\text{N}_4$ for tailoring the compositing semiconductors and optimizing the defect concentrations.

(2) DFT-guided optimization has been recognized as an effective strategy to guide the synthesis of active $g\text{-C}_3\text{N}_4$ based materials, interpretation of the structure-performance relationship, and unveiling the underlying mechanisms of catalytic reactions by scrutinizing the band structure, electron density distribution, orbital overlap/hybridizing, bonding behaviors, and reaction intermediates in an intuitive and mechanistic way. On the other hand, machine learning (ML) has recently aroused great research interest and demonstrated significant potential for catalyst design and activity enhancement relying on the established qualitative structural activity relationships (QSARs). ML can help optimize the types and content of hybridized metal-based

semiconductors and/or to tune the forms and density of the active sites on the photocatalysts. Combining DFT simulation with ML is promising to maximize the efficiency for catalysts design and establish the relationships between descriptors and catalytic properties. However, a large open-source QSAR database for ML model training is indispensable for its efficient and successful application.

(3) In-depth mechanistic investigations are still required. The synergistic interactions of the peroxide molecules with the charge carriers at the reaction interfaces are quite complex. Additionally, the reaction intermediates and their evolutions into the ROS are elusive. It is suggested that the synergism of the peroxide-coupled heterogeneous photocatalytic reaction can be clarified after the influences of material physiochemical properties on photocatalytic and catalytic Fenton reactions are elucidated. Additionally, *in situ/operando* characterization techniques such as *in situ* XANES, *in situ* Raman spectroscopy, and *in situ* electrochemical tests develop can be combined with the isotopic tracing method to elucidate interactions between the peroxide and the interfacial active sites, the generation and evolution of the ROS, and better differentiate the types of the electron transfer regime.

(4) Although inspiring breakthroughs have been achieved in design of the active photocatalysts and reactivities of the peroxide-coupled photocatalysis at the laboratory scale, there are still problematic issues that have to be tackled such as the large-scale synthesis and long-term stability of the photocatalysts, operating costs and flexibility, and suitability of the coupled process to the treated solution before the application at the practical scale even at the pilot scale. Moreover, attentions have to be paid on the influence of water matrix parameters such as the dissolved organic materials, inorganic anions, and complexing agents on the efficiency of the peroxide-coupled photocatalytic process during the practical operation.

CRediT authorship contribution statement

Wang Yuxian: Writing – review & editing, Supervision, Resources, Funding acquisition, Conceptualization. **Duan Xiaoguang:** Writing – review & editing, Supervision. **Chen Chunmao:** Writing – review & editing, Supervision, Funding acquisition. **Chen Peihan:** Writing – original draft. **Liu Ya:** Writing – review & editing, Conceptualization. **Zhou Menghan:** Writing – original draft. **Bofeng Li:** Writing – review & editing.

Declaration of Competing Interest

The authors declare the following financial interests/personal relationships which may be considered as potential competing interests: Yuxian Wang reports financial support was provided by National Natural Science Foundation of China. Yuxian Wang reports financial support was provided by Science Foundation of China University of Petroleum Beijing. Yuxian Wang reports financial support was provided by Young Elite Scientists Sponsorship Program by BAST. If there are other authors, they declare that they have no known competing financial interests or personal relationships that could have appeared to influence the work reported in this paper.

Data Availability

No data was used for the research described in the article.

Acknowledgements

The authors greatly appreciate the financial supports from the National Natural Science Foundation of China (No. 21978324 and 22278436), Science Foundation of China University of Petroleum-Beijing (No. 2462021QNXZ009), and Young Elite Scientists Sponsorship Program by BAST (No. 1101020370359).

References

- [1] J. Wang, R. Zhuan, Degradation of antibiotics by advanced oxidation processes: an overview, *Sci. Total Environ.* 701 (2020) 135023, <https://doi.org/10.1016/j.scitotenv.2019.135023>.
- [2] C. Feng, L. Tang, Y. Deng, J. Wang, Y. Liu, X. Ouyang, H. Yang, J. Yu, J. Wang, A novel sulfur-assisted annealing method of g-C₃N₄ nanosheet compensates for the loss of light absorption with further promoted charge transfer for photocatalytic production of H₂ and H₂O₂, *Appl. Catal. B-Environ.* 281 (2021) 119539, <https://doi.org/10.1016/j.apcatb.2020.119539>.
- [3] H. Sun, P. Qin, J. Guo, Y. Jiang, Y. Liang, X. Gong, X. Ma, Q. Wu, J. Zhang, L. Luo, Enhanced electron channel via the interfacial heterotropic electric field in dual S-scheme g-C₃N₄/WO₃/ZnS photocatalyst for year-round antibiotic degradation under sunlight, *Chem. Eng. J.* 470 (2023) 144217, <https://doi.org/10.1016/j.cej.2023.144217>.
- [4] D.B. Miklos, C. Remy, M. Jekel, K.G. Linden, J.E. Drewes, U. Hübner, Evaluation of advanced oxidation processes for water and wastewater treatment – A critical review, *Water Res* 139 (2018) 118–131, <https://doi.org/10.1016/j.watres.2018.03.042>.
- [5] K. Wang, C. Han, Z. Shao, J. Qiu, S. Wang, S. Liu, Perovskite oxide catalysts for advanced oxidation reactions, *Adv. Funct. Mater.* 31 (2021) 2102089, <https://doi.org/10.1002/adfm.202102089>.
- [6] H. Sun, F. Guo, J. Pan, W. Huang, K. Wang, W. Shi, One-pot thermal polymerization route to prepare N-deficient modified g-C₃N₄ for the degradation of tetracycline by the synergistic effect of photocatalysis and persulfate-based advanced oxidation process, *Chem. Eng. J.* 406 (2021) 126844, <https://doi.org/10.1016/j.cej.2020.126844>.
- [7] V. Hasija, V.H. Nguyen, A. Kumar, P. Raizada, V. Krishnan, A.A.P. Khan, P. Singh, E. Lichtfouse, C. Wang, P. Thi Huong, Advanced activation of persulfate by polymeric g-C₃N₄ based photocatalysts for environmental remediation: a review, *J. Hazard. Mater.* 413 (2021) 125324, <https://doi.org/10.1016/j.jhazmat.2021.125324>.
- [8] J. Yang, M. Zhu, D.D. Dionysiou, What is the role of light in persulfate-based advanced oxidation for water treatment? *Water Res* 189 (2021) 116627, <https://doi.org/10.1016/j.watres.2020.116627>.
- [9] O. Iqbal, H. Ali, N. Li, M.Z. Ansari, A.I. Al-Sulami, K.F. Alshammari, H.S. Abd-Rabbah, Y. Al-Hadeethi, T. Taha, A. Zada, A review on the synthesis, properties, and characterizations of graphitic carbon nitride (g-C₃N₄) for energy conversion and storage applications, *Mat. Today Phys.* 34 (2023) 101080, <https://doi.org/10.1016/j.mphys.2023.101080>.
- [10] W.J. Ong, L.L. Tan, Y.H. Ng, S.T. Yong, S.P. Chai, Graphitic carbon nitride (g-C₃N₄)-based photocatalysts for artificial photosynthesis and environmental remediation: are we a step closer to achieving sustainability? *Chem. Rev.* 116 (2016) 7159–7329, <https://doi.org/10.1021/acs.chemrev.6b00075>.
- [11] L. Wang, S. Karuturi, L. Zan, Bi₂S₃-In₂S₃ heterostructures for efficient photoreduction of highly toxic Cr⁶⁺ enabled by facet-coupling and Z-Scheme structure, *Small* 17 (2021) 2101833, <https://doi.org/10.1002/sml.202101833>.
- [12] P. Zhou, I.A. Navid, Y. Ma, Y. Xiao, P. Wang, Z. Ye, B. Zhou, K. Sun, Z. Mi, Solar-to-hydrogen efficiency of more than 9% in photocatalytic water splitting, *Nature* 613 (2023) 66–70, <https://doi.org/10.1038/s41586-022-05399-1>.
- [13] S.M. Abu-Sari, W.M.A.W. Daud, M.F.A. Patah, B.C. Ang, A review on synthesis, modification method, and challenges of light-driven H₂ evolution using g-C₃N₄-based photocatalyst, *Adv. Colloid Interface Sci.* 307 (2022) 102722, <https://doi.org/10.1016/j.cis.2022.102722>.
- [14] Y. Ren, J.J. Foo, D. Zeng, W.-J. Ong, ZnIn₂S₄-based nanostructures in artificial photosynthesis: insights into photocatalytic reduction toward sustainable energy production, *Small Struct.* 3 (2022) 2200017, <https://doi.org/10.1002/ssstr.202200017>.
- [15] C. Dai, B. Liu, Conjugated polymers for visible-light-driven photocatalysis, *Energy Environ. Sci.* 13 (2020) 24–52, <https://doi.org/10.1039/C9EE01935A>.
- [16] S.K. Loeb, P.J.J. Alvarez, J.A. Brame, E.L. Cates, W. Choi, J. Crittenden, D. Dionysiou, Q. Li, G. Li-Puma, X. Quan, D.L. Sedlak, T. David Waite, P. Westerhoff, J.-H. Kim, The technology horizon for photocatalytic water treatment: sunrise or sunset? *Environ. Sci. Technol.* 53 (2019) 2937–2947, <https://doi.org/10.1021/acs.est.8b05041>.
- [17] Y.X. Wang, X. Li, S.N. Liu, Y. Liu, T. Kong, H.Y. Zhang, X.G. Duan, C.M. Chen, S. B. Wang, Roles of catalyst structure and gas surface reaction in the generation of hydroxyl radicals for photocatalytic oxidation, *ACS Catal.* 12 (2022) 2770–2780, <https://doi.org/10.1021/acscatal.1c05447>.
- [18] L.L. Liu, F. Chen, J.H. Wu, M.K. Ke, C. Cui, J.J. Chen, H.Q. Yu, Edge electronic vacancy on ultrathin carbon nitride nanosheets anchoring O₂ to boost H₂O₂ photoproduction, *Appl. Catal. B-Environ.* 302 (2022) 120845, <https://doi.org/10.1016/j.apcatb.2021.120845>.
- [19] J. Xiao, J. Rabeah, J. Yang, Y. Xie, H. Cao, A. Brückner, Fast electron transfer and •OH formation: key features for high activity in visible-light-driven ozonation with C₃N₄ catalysts, *ACS Catal.* 7 (2017) 6198–6206, <https://doi.org/10.1021/acscatal.7b02180>.
- [20] B. Zhu, B. Cheng, L. Zhang, J. Yu, Review on DFT calculation of s-triazine-based carbon nitride, *Carbon Energy* 1 (2019) 32–56, <https://doi.org/10.1002/cey2.1>.
- [21] B. Zhu, L. Zhang, B. Cheng, J. Yu, First-principle calculation study of tri-s-triazine-based g-C₃N₄: a review, *Appl. Catal. B-Environ.* 224 (2018) 983–999, <https://doi.org/10.1016/j.apcatb.2017.11.025>.
- [22] J. Wang, S. Wang, A critical review on graphitic carbon nitride (g-C₃N₄)-based materials: preparation, modification and environmental application, *Coord. Chem. Rev.* 453 (2022) 214338, <https://doi.org/10.1016/j.ccr.2021.214338>.
- [23] J. Lin, W. Tian, Z. Guan, H. Zhang, X. Duan, H. Wang, H. Sun, Y. Fang, Y. Huang, S. Wang, Functional carbon nitride materials in photo-Fenton-like catalysis for environmental remediation, *Adv. Funct. Mater.* 32 (2022) 2201743, <https://doi.org/10.1002/adfm.202201743>.
- [24] J. Xiao, Y. Xie, J. Rabeah, A. Bruckner, H. Cao, Visible-light photocatalytic ozonation using graphitic C₃N₄ catalysts: a hydroxyl radical manufacturer for wastewater treatment, *Acc. Chem. Res.* 53 (2020) 1024–1033, <https://doi.org/10.1021/acs.accounts.9b00624>.
- [25] H. Wang, B. Liu, Q. Si, S. Wacławek, Y. Wu, W. Jia, T. Xie, W. Guo, N. Ren, Developing functional carbon nitride materials for efficient peroxymonosulfate activation: from interface catalysis to irradiation synergy, *EFM* 1 (2022) 21–33, <https://doi.org/10.1016/j.efmat.2022.05.007>.
- [26] Y. Xiao, G. Tian, W. Li, Y. Xie, B. Jiang, C. Tian, D. Zhao, H. Fu, Molecule self-assembly synthesis of porous few-layer carbon nitride for highly efficient photoredox catalysis, *J. Am. Chem. Soc.* 141 (2019) 2508–2515, <https://doi.org/10.1021/jacs.8b12428>.
- [27] T. Liu, W. Zhu, N. Wang, K. Zhang, X. Wen, Y. Xing, Y. Li, Preparation of structure vacancy defect modified diatomic-layered g-C₃N₄ nanosheet with enhanced photocatalytic performance, *Adv. Sci.* 10 (2023) 2302503, <https://doi.org/10.1002/advs.202302503>.
- [28] X. Zhang, X. Xie, H. Wang, J. Zhang, B. Pan, Y. Xie, Enhanced photoresponsive ultrathin graphitic-phase C₃N₄ nanosheets for bioimaging, *J. Am. Chem. Soc.* 135 (2013) 18–21, <https://doi.org/10.1021/ja308249k>.
- [29] X. Du, G. Zou, Z. Wang, X. Wang, A scalable chemical route to soluble acidified graphitic carbon nitride: an ideal precursor for isolated ultrathin g-C₃N₄ nanosheets, *Nanoscale* 7 (2015) 8701–8706, <https://doi.org/10.1039/C5NR00665A>.
- [30] Y. Wang, L. Liu, T. Ma, Y. Zhang, H. Huang, 2D graphitic carbon nitride for energy conversion and storage, *Adv. Funct. Mater.* 31 (2021) 2102540, <https://doi.org/10.1002/adfm.202102540>.
- [31] G.Z.S. Ling, S.F. Ng, W.J. Ong, Tailor-engineered 2D cocatalysts: Harnessing electron-hole redox center of 2D g-C₃N₄ photocatalysts toward solar-to-chemical conversion and environmental purification, *Adv. Funct. Mater.* 32 (2022) 2111875, <https://doi.org/10.1002/adfm.202111875>.
- [32] Q. Han, B. Wang, J. Gao, Z. Cheng, Y. Zhao, Z. Zhang, L. Qu, Atomically thin mesoporous nanomesh of graphitic C₃N₄ for high-efficiency photocatalytic hydrogen evolution, *ACS Nano* 10 (2016) 2745–2751, <https://doi.org/10.1021/acsnano.5b07831>.
- [33] W. Feng, P. Long, Y. Feng, Y. Li, Two-dimensional fluorinated graphene: synthesis, structures, properties and applications, *Adv. Sci.* 3 (2016) 1500413, <https://doi.org/10.1002/advs.201500413>.

- [34] X. Wang, Q. Li, L. Gan, X. Ji, F. Chen, X. Peng, R. Zhang, 3D macropore carbon-vacancy $\text{g-C}_3\text{N}_4$ constructed using polymethylmethacrylate spheres for enhanced photocatalytic H_2 evolution and CO_2 reduction, *J. Energy Chem.* 53 (2021) 139–146, <https://doi.org/10.1016/j.jchem.2020.05.001>.
- [35] Y. Li, Z. Ruan, Y. He, J. Li, K. Li, Y. Jiang, X. Xu, Y. Yuan, K. Lin, In situ fabrication of hierarchically porous $\text{g-C}_3\text{N}_4$ and understanding on its enhanced photocatalytic activity based on energy absorption, *Appl. Catal. B-Environ.* 236 (2018) 64–75, <https://doi.org/10.1016/j.apcatb.2018.04.082>.
- [36] Y. Li, X. Li, H. Zhang, Q. Xiang, Porous graphitic carbon nitride for solar photocatalytic applications, *Nanoscale Horiz.* 5 (2020) 765–786, <https://doi.org/10.1039/D0NH00046A>.
- [37] J. Xiao, Y. Xie, F. Nawaz, Y. Wang, P. Du, H. Cao, Dramatic coupling of visible light with ozone on honeycomb-like porous $\text{g-C}_3\text{N}_4$ towards superior oxidation of water pollutants, *Appl. Catal. B-Environ.* 183 (2016) 417–425, <https://doi.org/10.1016/j.apcatb.2015.11.010>.
- [38] Y. Zou, K. Xiao, Q. Qin, J. Shi, T. Heil, Y. Markushyna, L. Jiang, M. Antonietti, A. Savateev, Enhanced organic photocatalysis in confined flow through a carbon nitride nanotube membrane with conversions in the millisecond regime, *ACS Nano* 15 (2021) 6551–6561, <https://doi.org/10.1021/acsnano.0c09661>.
- [39] Q. Li, Y. Zhang, Y. Zeng, M. Ding, Ordered porous nitrogen-vacancy carbon nitride for efficient visible-light hydrogen evolution, *J. Colloid Interface Sci.* 642 (2023) 53–60, <https://doi.org/10.1016/j.jcis.2023.03.128>.
- [40] W. Li, X. Chu, F. Wang, Y. Dang, X. Liu, X. Wang, C. Wang, Enhanced cocatalyst-support interaction and promoted electron transfer of 3D porous $\text{g-C}_3\text{N}_4/\text{GO-M}$ (Au, Pd, Pt) composite catalysts for hydrogen evolution, *Appl. Catal. B-Environ.* 288 (2021) 120034, <https://doi.org/10.1016/j.apcatb.2021.120034>.
- [41] Y. Tian, L. Zhou, Q. Zhu, J. Lei, L. Wang, J. Zhang, Y. Liu, Hierarchical macro-mesoporous $\text{g-C}_3\text{N}_4$ with an inverse opal structure and vacancies for high-efficiency solar energy conversion and environmental remediation, *Nanoscale* 11 (2019) 20638–20647, <https://doi.org/10.1039/C9NR06802C>.
- [42] Y. Shi, C. Liu, L. Fu, F. Yang, Y. Lv, B. Yu, Hierarchical assembly of polystyrene/graphitic carbon nitride/reduced graphene oxide nanocomposites toward high fire safety, *Compos. B. Eng.* 179 (2019) 107541, <https://doi.org/10.1016/j.compositesb.2019.107541>.
- [43] D. Guo, Y. Wang, C. Chen, J. He, M. Zhu, J. Chen, C. Zhang, A multi-structural carbon nitride co-modified by Co, S to dramatically enhance mineralization of Bisphenol in the photocatalysis-PMS oxidation coupling system, *Chem. Eng. J.* 422 (2021) 130035, <https://doi.org/10.1016/j.cej.2021.130035>.
- [44] S. Kang, L. Zhang, M. He, Y. Zheng, L. Cui, D. Sun, B. Hu, Alternated cooling and heating" strategy enables rapid fabrication of highly-crystalline $\text{g-C}_3\text{N}_4$ nanosheets for efficient photocatalytic water purification under visible light irradiation, *Carbon* 137 (2018) 19–30, <https://doi.org/10.1016/j.carbon.2018.05.010>.
- [45] X. Wang, Q. Liu, Q. Yang, Z. Zhang, X. Fang, Three-dimensional $\text{g-C}_3\text{N}_4$ aggregates of hollow bubbles with high photocatalytic degradation of tetracycline, *Carbon* 136 (2018) 103–112, <https://doi.org/10.1016/j.carbon.2018.04.059>.
- [46] X. Dong, F. Cheng, Recent development in exfoliated two-dimensional $\text{g-C}_3\text{N}_4$ nanosheets for photocatalytic applications, *J. Mater. Chem. A* 3 (2015) 23642–23652, <https://doi.org/10.1039/c5ta07374j>.
- [47] J. Dong, Y. Zhang, M. Hussain, W. Zhou, Y. Chen, L. Wang, $\text{G-C}_3\text{N}_4$: properties, pore modifications, and photocatalytic applications, *Nanomaterials* 12 (2022) 121, <https://doi.org/10.3390/nano12010121>.
- [48] P. Praus, L. Řeháček, J. Čížek, A. Smýkalová, M. Koštein, J. Pavlovský, M. Filip Edelmannová, K. Kočí, Synthesis of vacant graphitic carbon nitride in argon atmosphere and its utilization for photocatalytic hydrogen generation, *Sci. Rep.* 12 (2022) 13622, <https://doi.org/10.1038/s41598-022-17940-3>.
- [49] X. Wang, J. Meng, X. Zhang, Y. Liu, M. Ren, Y. Yang, Y. Guo, Controllable approach to carbon-deficient and oxygen-doped graphitic carbon nitride: robust photocatalyst against recalcitrant organic pollutants and the mechanism insight, *Adv. Funct. Mater.* 31 (2021) 2010763, <https://doi.org/10.1002/adfm.202010763>.
- [50] X. Liu, W. Kang, W. Zeng, Y. Zhang, L. Qi, F. Ling, L. Fang, Q. Chen, M. Zhou, Structural, electronic and photocatalytic properties of $\text{g-C}_3\text{N}_4$ with intrinsic defects: a first-principles hybrid functional investigation, *Appl. Surf. Sci.* 499 (2020) 143994, <https://doi.org/10.1016/j.apsusc.2019.143994>.
- [51] F. Li, Z. Lu, P. Zhang, Y. Jin, T. Li, C. Hu, Boosting the extra generation of superoxide radicals on graphitic carbon nitride with carbon vacancies by the modification of pollutant adsorption for high-performance photocatalytic degradation, *Environ. Sci. Technol.* 2 (2022) 1296–1305, <https://doi.org/10.1021/acsestengg.1c00459>.
- [52] B. Gao, M. Dou, J. Wang, S. Li, D. Wang, L. Ci, Y. Fu, Efficient persulfate activation by carbon defects $\text{g-C}_3\text{N}_4$ containing electron traps for the removal of antibiotics, resistant bacteria and genes, *Chem. Eng. J.* 426 (2021) 123713, <https://doi.org/10.1016/j.cej.2021.131677>.
- [53] I.F. Silva, I.F. Teixeira, R.D.F. Rios, G.M. do Nascimento, I. Binatti, H.F. V. Victoriae, K. Krambrock, L.A. Cury, A.P.C. Teixeira, H.O. Stumpf, Amoxicillin photodegradation under visible light catalyzed by metal-free carbon nitride: an investigation of the influence of the structural defects, *J. Hazard. Mater.* 401 (2021) 10, <https://doi.org/10.1016/j.jhazmat.2020.123713>.
- [54] J. Li, J. Huang, G. Zeng, C. Zhang, H. Yu, Q. Wan, K. Yi, W. Zhang, H. Pang, S. Liu, S. Li, W. He, Efficient photosynthesis of H_2O_2 via two-electron oxygen reduction reaction by defective $\text{g-C}_3\text{N}_4$ with terminal cyano groups and nitrogen vacancies, *Chem. Eng. J.* 463 (2023) 142512, <https://doi.org/10.1016/j.cej.2023.142512>.
- [55] W. Tu, Y. Xu, J. Wang, B. Zhang, T. Zhou, S. Yin, S. Wu, C. Li, Y. Huang, Y. Zhou, Z. Zou, J. Robertson, M. Kraft, R. Xu, Investigating the role of tunable nitrogen vacancies in graphitic carbon nitride nanosheets for efficient visible-light-driven H_2 evolution and CO_2 reduction, *ACS Sustain. Chem. Eng.* 5 (2017) 7260–7268, <https://doi.org/10.1021/acssuschemeng.7b01477>.
- [56] S. Hou, X. Gao, S. Wang, X. Yu, J. Liao, D. Su, Precise defect engineering on graphitic carbon nitrides for boosted solar H_2 production, *Small* n/a 2302500, <https://doi.org/10.1002/smll.202302500>.
- [57] H. Lan, Q. Tang, Z. Hou, K. Zhu, X. An, H. Liu, J. Qu, Hydrogen-induced defective crystalline carbon nitride with enhanced bidirectional charge migration for persulfate photoactivation, *Environ. Sci. Technol.* 3 (2023) 580–589, <https://doi.org/10.1021/acsestengg.2c00365>.
- [58] S. Li, G. Dong, R. Hailili, L. Yang, Y. Li, F. Wang, Y. Zeng, C. Wang, Effective photocatalytic H_2O_2 production under visible light irradiation at $\text{g-C}_3\text{N}_4$ modulated by carbon vacancies, *Appl. Catal. B-Environ.* 190 (2016) 26–35, <https://doi.org/10.1016/j.apcatb.2016.03.004>.
- [59] X. Zhan, Z. Peng, H. Huang, H. Zhang, Z. Liu, X. Ou, F. Yang, Z. Liu, Photoelectrochemical performance enhancement of low-energy Ar^+ irradiation modified TiO_2 , *Appl. Surf. Sci.* 541 (2021) 148527, <https://doi.org/10.1016/j.apsusc.2020.148527>.
- [60] X. Wang, L. Wu, Z. Wang, H. Wu, X. Zhou, H. Ma, H. Zhong, Z. Xing, G. Cai, C. Jiang, F. Ren, C/N vacancy Co-enhanced visible-light-driven hydrogen evolution of $\text{g-C}_3\text{N}_4$ nanosheets through controlled He^+ ion irradiation, *Sol. Rrl.* 3 (2019) 9, <https://doi.org/10.1002/solr.201800298>.
- [61] X. Wang, L. Wu, Z. Wang, H. Wu, X. Zhou, H. Ma, H. Zhong, Z. Xing, G. Cai, C. Jiang, F. Ren, C/N vacancy Co-enhanced visible-light-driven hydrogen evolution of $\text{g-C}_3\text{N}_4$ nanosheets through controlled He^+ ion irradiation, *Sol. Rrl.* 3 (2019) 1800298, <https://doi.org/10.1002/solr.201800298>.
- [62] D. Zhao, C. Dong, B. Wang, C. Chen, Y. Huang, Z. Diao, S. Li, L. Guo, S. Shen, Synergy of dopants and defects in graphitic carbon nitride with exceptionally modulated band structures for efficient photocatalytic oxygen evolution, *Adv. Mater.* 31 (2019) 1903545, <https://doi.org/10.1002/adma.201903545>.
- [63] H. Katsumata, F. Higashi, Y. Kobayashi, I. Tateishi, M. Furukawa, S. Kaneco, Dual-defect-modified graphitic carbon nitride with boosted photocatalytic activity under visible light, *Sci. Rep.* 9 (2019) 14873, <https://doi.org/10.1038/s41598-019-49949-6>.
- [64] W. Wang, L. Du, R. Xia, R. Liang, T. Zhou, H.K. Lee, Z. Yan, H. Luo, C. Shang, D. L. Phillips, Z. Guo, In situ protonated-phosphorus interstitial doping induces long-lived shallow charge trapping in porous $\text{C}_3\text{-xN}_4$ photocatalysts for highly efficient H_2 generation, *Environ. Sci. Technol.* 16 (2023) 460–472, <https://doi.org/10.1039/D2EE02680E>.
- [65] L. Jiang, X. Yuan, Y. Pan, J. Liang, G. Zeng, Z. Wu, H. Wang, Doping of graphitic carbon nitride for photocatalysis: a review, *Appl. Catal. B-Environ.* 217 (2017) 388–406, <https://doi.org/10.1016/j.apcatb.2017.06.003>.
- [66] M. Cui, K. Cui, X. Liu, X. Chen, Z. Guo, Y. Chen, C. Li, Insights into the photocatalytic peroxymonosulfate activation over defective boron-doped carbon nitride for efficient pollutants degradation, *J. Hazard. Mater.* 418 (2021) 126338, <https://doi.org/10.1016/j.jhazmat.2021.126338>.
- [67] M. Jing, H. Zhao, L. Jian, C. Pan, Y. Dong, Y. Zhu, Coral-like B-doped $\text{g-C}_3\text{N}_4$ with enhanced molecular dipole to boost photocatalysis-self-Fenton removal of persistent organic pollutants, *J. Hazard. Mater.* 449 (2023) 131017, <https://doi.org/10.1016/j.jhazmat.2023.131017>.
- [68] Y. Gao, Y. Zhu, L. Lyu, Q. Zeng, X. Xing, C. Hu, Electronic structure modulation of graphitic carbon nitride by oxygen doping for enhanced catalytic degradation of organic pollutants through peroxymonosulfate activation, *Environ. Sci. Technol.* 52 (2018) 14371–14380, <https://doi.org/10.1021/acs.est.8b05246>.
- [69] F. Chen, L. Liu, J. Chen, W. Li, Y. Chen, Y. Zhang, J. Wu, S. Mei, Q. Yang, H. Yu, Efficient decontamination of organic pollutants under high salinity conditions by a nonradical peroxymonosulfate activation system, *Water Res* 191 (2021) 116799, <https://doi.org/10.1016/j.watres.2020.116799>.
- [70] B. Yan, C. Du, G. Yang, Constructing built-in electric field in ultrathin graphitic carbon nitride nanosheets by N and O codoping for enhanced photocatalytic hydrogen evolution activity, *Small* 16 (2020) 1905700, <https://doi.org/10.1002/smll.201905700>.
- [71] J. Tan, Z. Li, J. Li, Y. Meng, X. Yao, Y. Wang, Y. Lu, T. Zhang, Visible-light-assisted peroxymonosulfate activation by metal-free bifunctional oxygen-doped graphitic carbon nitride for enhanced degradation of imidacloprid: Role of non-photochemical and photocatalytic activation pathway, *J. Hazard. Mater.* 423 (2022) 127048, <https://doi.org/10.1016/j.jhazmat.2021.127048>.
- [72] Y. Shi, J. Li, D. Wan, J. Huang, Y. Liu, Peroxymonosulfate-enhanced photocatalysis by carbonyl-modified $\text{g-C}_3\text{N}_4$ for effective degradation of the tetracycline hydrochloride, *Sci. Total Environ.* 749 (2020) 142313, <https://doi.org/10.1016/j.scitotenv.2020.142313>.
- [73] Y. Zhou, L. Zhang, J. Liu, X. Fan, B. Wang, M. Wang, W. Ren, J. Wang, M. Li, J. Shi, Brand new P-doped $\text{g-C}_3\text{N}_4$: enhanced photocatalytic activity for H_2 evolution and Rhodamine B degradation under visible light, *J. Mater. Chem. A* 3 (2015) 3862–3867, <https://doi.org/10.1039/C4TA05292G>.
- [74] P. Zhang, Y. Tong, Y. Liu, J.J.M. Vequizo, H. Sun, C. Yang, A. Yamakata, F. Fan, W. Lin, X. Wang, W. Choi, Heteroatom dopants promote two-electron O_2 reduction for photocatalytic production of H_2O_2 on polymeric carbon nitride, *Angew. Chem. Int. Ed.* 59 (2020) 16209–16217, <https://doi.org/10.1002/anie.202006747>.
- [75] K. Lin, Z. Zhang, Degradation of Bisphenol A using peroxymonosulfate activated by one-step prepared sulfur-doped carbon nitride as a metal-free heterogeneous catalyst, *Chem. Eng. J.* 313 (2017) 1320–1327, <https://doi.org/10.1016/j.cej.2016.11.025>.

- [76] B. Zhu, J. Zhang, C. Jiang, B. Cheng, J. Yu, First principle investigation of halogen-doped monolayer g-C₃N₄ photocatalyst, *Appl. Catal. B-Environ.* 207 (2017) 27–34, <https://doi.org/10.1016/j.apcatb.2017.02.020>.
- [77] Y. Tan, W. Chen, G. Liao, X. Li, J. Wang, Y. Tang, L. Li, Strategy for improving photocatalytic ozonation activity of g-C₃N₄ by halogen doping for water purification, *Appl. Catal. B-Environ.* 306 (2022) 121133, <https://doi.org/10.1016/j.apcatb.2022.121133>.
- [78] X. Fan, Z. Wang, T. Lin, D. Du, M. Xiao, P. Chen, S.A. Monny, H. Huang, M. Lyu, M. Lu, L. Wang, Coordination chemistry engineered polymeric carbon nitride photoanode with ultralow onset potential for water splitting, *Angew. Chem. Int. Ed.* 61 (2022) e202204407, <https://doi.org/10.1002/anie.202204407>.
- [79] R. Shakir, H. Komsa, A. Sinha, J. Karthikeyan, Electronic origin of enhanced selectivity through the halogenation of a single Mn atom on graphitic C₃N₄ for electrocatalytic reduction of CO₂ from first-principles calculations, *J. Phys. Chem. C.* 127 (2023) 14694–14703, <https://doi.org/10.1021/acs.jpcc.3c00597>.
- [80] X. Hai, S. Xi, S. Mitchell, K. Harrath, H. Xu, D.F. Akl, D. Kong, J. Li, Z. Li, T. Sun, H. Yang, Y. Cui, C. Su, X. Zhao, J. Li, J. Pérez-Ramírez, J. Lu, Scalable two-step annealing method for preparing ultra-high-density single-atom catalyst libraries, *Nat. Nanotechnol.* 17 (2022) 174–181, <https://doi.org/10.1038/s41565-021-01022-y>.
- [81] G. Vilé, D. Albani, M. Nachtgaal, Z. Chen, D. Dontsova, M. Antonietti, N. López, J. Pérez-Ramírez, A stable single-site palladium catalyst for hydrogenations, *Angew. Chem. Int. Ed.* 54 (2015) 11265–11269, <https://doi.org/10.1002/anie.201505073>.
- [82] C. Hu, J. Hu, Z. Zhu, Y. Lu, S. Chu, T. Ma, Y. Zhang, H. Huang, Orthogonal charge transfer by precise positioning of silver single atoms and clusters on carbon nitride for efficient piezocatalytic pure water splitting, *Angew. Chem. Int. Ed.* 61 (2022) e202212397, <https://doi.org/10.1002/anie.202212397>.
- [83] P. Gan, Z. Zhang, Y. Hu, Y. Li, J. Ye, M. Tong, J. Liang, Insight into the role of Fe in the synergetic effect of persulfate/sulfite and Fe₂O₃@g-C₃N₄ for carbamazepine degradation, *Sci. Total Environ.* 819 (2022) 152787, <https://doi.org/10.1016/j.scitotenv.2021.152787>.
- [84] X. Liu, Y. Li, X. Fan, F. Zhang, G. Zhang, W. Peng, Photo-accelerated Co³⁺/Co²⁺ transformation on cobalt and phosphorus co-doped g-C₃N₄ for Fenton-like reaction, *J. Mater. Chem. A* 9 (2021) 22399–22409, <https://doi.org/10.1039/D1TA06026K>.
- [85] M. Qian, X. Wu, M. Lu, L. Huang, W. Li, H. Lin, J. Chen, S. Wang, X. Duan, Modulation of charge trapping by island-like single-atom cobalt catalyst for enhanced photo-Fenton-like reaction, *Adv. Funct. Mater.* 33 (2023) 2208688, <https://doi.org/10.1002/adfm.202208688>.
- [86] Y. Li, B. Li, D. Zhang, L. Cheng, Q. Xiang, Crystalline carbon nitride supported copper single atoms for photocatalytic CO₂ reduction with nearly 100% CO selectivity, *ACS Nano* 14 (2020) 10552–10561, <https://doi.org/10.1021/acsnano.0c04544>.
- [87] F. Chen, L. Liu, J. Wu, X. Rui, J. Chen, Y. Yu, Single-atom iron anchored tubular g-C₃N₄ catalysts for ultrafast Fenton-like reaction: roles of high-valency iron-oxo species and organic radicals, *Adv. Mater.* 34 (2022) 2202891, <https://doi.org/10.1002/adma.202202891>.
- [88] X. Xiao, L. Zhang, H. Meng, B. Jiang, H. Fu, Single metal atom decorated carbon nitride for efficient photocatalysis: synthesis, structure, and applications, *Sol. Rrl.* 5 (2021) 2000609, <https://doi.org/10.1002/solr.202000609>.
- [89] T. Tong, B. He, B. Zhu, B. Cheng, L. Zhang, First-principle investigation on charge carrier transfer in transition-metal single atoms loaded g-C₃N₄, *Appl. Surf. Sci.* 459 (2018) 385–392, <https://doi.org/10.1016/j.apsusc.2018.08.007>.
- [90] H. Shi, Y. He, Y. Li, P. Luo, Unraveling the synergy mechanism between photocatalysis and peroxymonosulfate activation on a Co/Fe bimetal-doped carbon nitride, *ACS Catal.* 13 (2023) 8973–8986, <https://doi.org/10.1021/acscatal.3c01496>.
- [91] S. Ji, Y. Yang, Z. Zhou, X. Li, Y. Liu, Photocatalysis-Fenton of Fe-doped g-C₃N₄ catalyst and its excellent degradation performance towards RhB, *J. Water Process. Eng.* 40 (2021) 101804, <https://doi.org/10.1016/j.jwpe.2020.101804>.
- [92] H. Cao, J. Wang, J.-H. Kim, Z. Guo, J. Xiao, J. Yang, J. Chang, Y. Shi, Y. Xie, Different roles of Fe atoms and nanoparticles on g-C₃N₄ in regulating the reductive activation of ozone under visible light, *Appl. Catal. B-Environ.* 296 (2021) 120362, <https://doi.org/10.1016/j.apcatb.2021.120362>.
- [93] X. Peng, J. Wu, Z. Zhao, X. Wang, H. Dai, L. Xu, G. Xu, Y. Jian, F. Hu, Activation of peroxymonosulfate by single-atom Fe-g-C₃N₄ catalysts for high efficiency degradation of tetracycline via nonradical pathways: Role of high-valent iron-oxo species and Fe-Nx sites, *Chem. Eng. J.* 427 (2022) 130803, <https://doi.org/10.1016/j.cej.2021.130803>.
- [94] T. Xiong, W. Cen, Y. Zhang, F. Dong, Bridging the g-C₃N₄ interlayers for enhanced photocatalysis, *ACS Catal.* 6 (2016) 2462–2472, <https://doi.org/10.1021/acscatal.5b02922>.
- [95] P. Deng, J. Xiong, S. Lei, W. Wang, X. Ou, Y. Xu, Y. Xiao, B. Cheng, Nickel formate induced high-level in situ Ni-doping of g-C₃N₄ for a tunable band structure and enhanced photocatalytic performance, *J. Mater. Chem. A* 7 (2019) 22385–22397, <https://doi.org/10.1039/c9ta04559g>.
- [96] Y. Li, M. Zhou, B. Cheng, Y. Shao, Recent advances in g-C₃N₄-based heterojunction photocatalysts, *J. Mater. Sci. Technol.* 56 (2020) 1–17, <https://doi.org/10.1016/j.jmst.2020.04.028>.
- [97] J. Fu, Q. Xu, J. Low, C. Jiang, J. Yu, Ultrathin 2D/2D WO₃/g-C₃N₄ step-scheme H₂-production photocatalyst, *Appl. Catal. B-Environ.* 243 (2019) 556–565, <https://doi.org/10.1016/j.apcatb.2018.11.011>.
- [98] P. Xia, S. Cao, B. Zhu, M. Liu, M. Shi, J. Yu, Y. Zhang, Designing a 0D/2D S-scheme heterojunction over polymeric carbon nitride for visible-light photocatalytic inactivation of bacteria, *Angew. Chem. Int. Ed.* 59 (2020) 5218–5225, <https://doi.org/10.1002/anie.201916012>.
- [99] M. Tan, Y. Ma, C. Yu, Q. Luan, J. Li, C. Liu, W. Dong, Y. Su, L. Qiao, L. Gao, Q. Lu, Y. Bai, Boosting photocatalytic hydrogen production via interfacial engineering on 2D ultrathin Z-scheme ZnIn₂S₄/g-C₃N₄ heterojunction, *Adv. Funct. Mater.* 32 (2022) 2111740, <https://doi.org/10.1002/adfm.202111740>.
- [100] H. Tran Huu, M.D.N. Thi, V.P. Nguyen, L.N. Thi, T.T.T. Phan, Q.D. Hoang, H. H. Luc, S.J. Kim, V. Vo, One-pot synthesis of S-scheme MoS₂/g-C₃N₄ heterojunction as effective visible light photocatalyst, *Sci. Rep.* 11 (2021) 14787, <https://doi.org/10.1038/s41598-021-94129-0>.
- [101] D. Kim, K. Yong, Boron doping induced charge transfer switching of a C₃N₄/ZnO photocatalyst from Z-scheme to type II to enhance photocatalytic hydrogen production, *Appl. Catal. B-Environ.* 282 (2021) 119538, <https://doi.org/10.1016/j.apcatb.2020.119538>.
- [102] D.S. Vavilapalli, R.G. Peri, R.K. Sharma, U.K. Goutam, B. Muthuraaman, M. S. Ramachandra Rao, S. Singh, G-C₃N₄/Ca₂Fe₂O₅ heterostructures for enhanced photocatalytic degradation of organic effluents under sunlight, *Sci. Rep.* 11 (2021) 19639, <https://doi.org/10.1038/s41598-021-99020-6>.
- [103] J. Low, C. Jiang, B. Cheng, S. Wageh, A.A. Al-Ghamdi, J. Yu, A review of direct Z-scheme photocatalysts, *Small Methods* 1 (2017) 21, <https://doi.org/10.1002/smt.201700080>.
- [104] J. Low, J. Yu, M. Jaroniec, S. Wageh, A.A. Al-Ghamdi, Heterojunction photocatalysts, *Adv. Mater.* 29 (2017) 20, <https://doi.org/10.1002/adma.201601694>.
- [105] Y. Li, Z. Xia, Q. Yang, L. Wang, Y. Xing, Review on g-C₃N₄-based S-scheme heterojunction photocatalysts, *J. Mater. Sci. Technol.* 125 (2022) 128–144, <https://doi.org/10.1016/j.jmst.2022.02.035>.
- [106] J. Fu, J. Yu, C. Jiang, B. Cheng, G-C₃N₄-based heterostructured photocatalysts, *Adv. Energy Mater.* 8 (2018) 31, <https://doi.org/10.1002/aenm.201701503>.
- [107] L. Sun, Y. Qi, C. Jia, Z. Jin, W. Fan, Enhanced visible-light photocatalytic activity of g-C₃N₄/Zn₂GeO₄ heterojunctions with effective interfaces based on band match, *Nanoscale* 6 (2014) 2649–2659, <https://doi.org/10.1039/c3nr06104c>.
- [108] C. Liu, H. Dai, C. Tan, Q. Pan, F. Hu, X. Peng, Photo-Fenton degradation of tetracycline over Z-scheme Fe-g-C₃N₄/Bi₂WO₆ heterojunctions: Mechanism insight, degradation pathways and DFT calculation, *Appl. Catal. B-Environ.* 310 (2022) 121326, <https://doi.org/10.1016/j.apcatb.2022.121326>.
- [109] Q. Wang, P. Wang, P. Xu, Y. Li, J. Duan, G. Zhang, L. Hu, X. Wang, W. Zhang, Visible-light-driven photo-Fenton reactions using Zn_{1-1.5}Fe_{0.5}S/g-C₃N₄ photocatalyst: degradation kinetics and mechanisms analysis, *Appl. Catal. B-Environ.* 266 (2020) 118653, <https://doi.org/10.1016/j.apcatb.2020.118653>.
- [110] Q. Xu, D. Ma, S. Yang, Z. Tian, B. Cheng, J. Fan, Novel g-C₃N₄/g-C₃N₄ S-scheme isotype heterojunction for improved photocatalytic hydrogen generation, *Appl. Surf. Sci.* 495 (2019) 143555, <https://doi.org/10.1016/j.apsusc.2019.143555>.
- [111] Y. Ling, H. Liu, B. Li, B. Zhang, Y. Wu, H. Hu, D. Yu, S. Huang, Efficient photocatalytic ozonation of azithromycin by three-dimensional g-C₃N₄ nanosheet loaded magnetic Fe-MCM-48 under simulated solar light, *Appl. Catal. B-Environ.* 324 (2023) 122208, <https://doi.org/10.1016/j.apcatb.2022.122208>.
- [112] B. Zhu, G. Jiang, S. Chen, F. Liu, Y. Wang, C. Zhao, Multifunctional Cl-S double-doped carbon nitride nanotube unit in catalytic ozone oxidation synergistic photocatalytic system: Generation of ROS-rich region and effective treatment of organic wastewater, *Chem. Eng. J.* 430 (2022) 132843, <https://doi.org/10.1016/j.cej.2021.132843>.
- [113] X. Liu, Q. Zhang, D. Ma, Advances in 2D/2D Z-scheme heterojunctions for photocatalytic applications, *Sol. Rrl.* 5 (2021) 32, <https://doi.org/10.1002/solr.202000397>.
- [114] C. Cheng, B. He, J. Fan, B. Cheng, S. Cao, J. Yu, An inorganic/organic S-scheme heterojunction H₂-production photocatalyst and its charge transfer mechanism, *Adv. Mater.* 33 (2021) 8, <https://doi.org/10.1002/adma.202100317>.
- [115] H.S. Moon, K. Hsiao, M. Wu, Y. Yun, Y. Hsu, K. Yong, Spatial separation of cocatalysts on Z-scheme organic/inorganic heterostructure hollow spheres for enhanced photocatalytic H₂ evolution and in-depth analysis of the charge-transfer mechanism, *Adv. Mater.* 35 (2023) 2200172, <https://doi.org/10.1002/adma.202200172>.
- [116] Y. Li, S. Wang, W. Chang, L. Zhang, Z. Wu, R. Jin, Y. Xing, Co-monomer engineering optimized electron delocalization system in carbon-bridging modified g-C₃N₄ nanosheets with efficient visible-light photocatalytic performance, *Appl. Catal. B-Environ.* 274 (2020) 119116, <https://doi.org/10.1016/j.apcatb.2020.119116>.
- [117] S. Chu, Y. Wang, Y. Guo, J. Feng, C. Wang, W. Luo, X. Fan, Z. Zou, Band structure engineering of carbon nitride: in search of a polymer photocatalyst with high photooxidation property, *ACS Catal.* 3 (2013) 912–919, <https://doi.org/10.1021/cs4000624>.
- [118] X. Zhang, B. Ren, X. Li, B. Liu, S. Wang, P. Yu, Y. Xu, G. Jiang, High-efficiency removal of tetracycline by carbon-bridge-doped g-C₃N₄/Fe₃O₄ magnetic heterogeneous catalyst through photo-Fenton process, *J. Hazard. Mater.* 418 (2021) 126333, <https://doi.org/10.1016/j.jhazmat.2021.126333>.
- [119] H. Xu, Y. Ma, J. Chen, W. Zhang, J. Yang, Electrocatalytic reduction of nitrate - a step towards a sustainable nitrogen cycle, *Chem. Soc. Rev.* 51 (2022) 2710–2758, <https://doi.org/10.1039/d1cs00857a>.
- [120] R. Yue, M. Saifur Rahman, Hydrophilic and underwater superoleophobic porous graphitic carbon nitride (g-C₃N₄) membranes with photo-Fenton self-cleaning ability for efficient oil/water separation, *J. Colloid Interface Sci.* 608 (2022) 1960–1972, <https://doi.org/10.1016/j.jcis.2021.10.162>.
- [121] Y. Li, Q. Zhang, Y. Lu, Z. Song, C. Wang, D. Li, X. Tang, X. Zhou, Surface hydroxylation of TiO₂/g-C₃N₄ photocatalyst for photo-Fenton degradation of

- tetracycline, *Ceram. Int.* 48 (2022) 1306–1313, <https://doi.org/10.1016/j.ceramint.2021.09.215>.
- [122] J. Zhang, X. Zhao, Y. Wang, Y. Gong, D. Cao, M. Qiao, Peroxymonosulfate-enhanced visible light photocatalytic degradation of bisphenol A by perylene imide-modified g-C₃N₄, *Appl. Catal. B-Environ.* 237 (2018) 976–985, <https://doi.org/10.1016/j.apcatb.2018.06.049>.
- [123] X. Du, X. Bai, L. Xu, L. Yang, P. Jin, Visible-light activation of persulfate by TiO₂/g-C₃N₄ photocatalyst toward efficient degradation of micropollutants, *Chem. Eng. J.* 384 (2020) 123245, <https://doi.org/10.1016/j.cej.2019.123245>.
- [124] Z. Cheng, L. Ling, J. Fang, C. Shang, Visible light-driven g-C₃N₄ peroxymonosulfate activation process for carbamazepine degradation: activation mechanism and matrix effects, *Chemosphere* 286 (2022) 131906, <https://doi.org/10.1016/j.chemosphere.2021.131906>.
- [125] H. Ming, P. Zhang, Y. Yang, Y. Zou, C. Yang, Y. Hou, K. Ding, J. Zhang, X. Wang, Tailored poly-heptazine units in carbon nitride for activating peroxymonosulfate to degrade organic contaminants with visible light, *Appl. Catal. B-Environ.* 311 (2022) 121341, <https://doi.org/10.1016/j.apcatb.2022.121341>.
- [126] T. Zeng, S. Jin, S. Li, J. Bao, Z. Jin, D. Wang, F. Dong, H. Zhang, S. Song, Covalent triazine framework with defective accumulation sites: exceptionally modulated electronic structure for solar-driven oxidative activation of peroxymonosulfate, *Environ. Sci. Technol.* 56 (2022) 9474–9485, <https://doi.org/10.1021/acs.est.2c00126>.
- [127] G. Liu, T. Zhang, T. Wang, H. Yamashita, Y. Zhao, X. Qian, Peroxydisulfate activation by photo-generated charges on mesoporous carbon nitride for removal of chlorophenols, *Appl. Catal. B-Environ.* 296 (2021) 120370, <https://doi.org/10.1016/j.apcatb.2021.120370>.
- [128] M. Dou, J. Wang, B. Gao, Z. Ma, X. Huang, A novel in-situ chemical oxidation channel – Selective pH-dependence of refractory β -lactam antibiotics in the synergistic mechanism of persulfate and g-C₃N₄ under visible light, *Chem. Eng. J.* 394 (2020) 124899, <https://doi.org/10.1016/j.cej.2020.124899>.
- [129] R. Li, M. Cai, Z. Xie, Q. Zhang, Y. Zeng, H. Liu, G. Liu, W. Lv, Construction of heterostructured CuFe₂O₄/g-C₃N₄ nanocomposite as an efficient visible light photocatalyst with peroxydisulfate for the organic oxidation, *Appl. Catal. B-Environ.* 244 (2019) 974–982, <https://doi.org/10.1016/j.apcatb.2018.12.043>.
- [130] D. Li, Y. Xiao, M. Pu, J. Zan, S. Zuo, H. Xu, D. Xia, A metal-free protonated g-C₃N₄ as an effective sodium percarbonate activator at ambient pH conditions: efficiency, stability and mechanism, *Mater. Chem. Phys.* 231 (2019) 225–232, <https://doi.org/10.1016/j.matchemphys.2019.04.016>.
- [131] F. Deng, H. Olvera-Vargas, M. Zhou, S. Qiu, I. Sirés, E. Brillás, Critical review on the mechanisms of Fe²⁺ regeneration in the electro-Fenton process: fundamentals and boosting strategies, *Chem. Rev.* 123 (2023) 4635–4662, <https://doi.org/10.1021/acs.chemrev.2c00684>.
- [132] J.M. Barazesh, T. Hennebel, J.T. Jasper, D.L. Sedlak, Modular advanced oxidation process enabled by cathodic hydrogen peroxide production, *Environ. Sci. Technol.* 49 (2015) 7391–7399, <https://doi.org/10.1021/acs.est.5b01254>.
- [133] K. Sharma, P. Raizada, A. Hosseini-Bandegharai, P. Thakur, R. Kumar, V. K. Thakur, V.H. Nguyen, S. Pardeep, Fabrication of efficient CuO / graphitic carbon nitride based heterogeneous photo-Fenton like catalyst for degradation of 2, 4 dimethyl phenol, *Process Saf. Environ.* 142 (2020) 63–75, <https://doi.org/10.1016/j.psep.2020.06.003>.
- [134] M. Liu, D. Zhang, J. Han, C. Liu, Y. Ding, Z. Wang, A. Wang, Adsorption enhanced photocatalytic degradation sulfadiazine antibiotic using porous carbon nitride nanosheets with carbon vacancies, *Chem. Eng. J.* 382 (2020) 123017, <https://doi.org/10.1016/j.cej.2019.123017>.
- [135] J. Ma, K. Wang, C. Wang, X. Chen, W. Zhu, G. Zhu, W. Yao, Y. Zhu, Photocatalysis-self-Fenton system with high-fluent degradation and high mineralization ability, *Appl. Catal. B-Environ.* 276 (2020) 119150, <https://doi.org/10.1016/j.apcatb.2020.119150>.
- [136] L. Zhang, B. Zhang, Y. Liu, Z. Wang, J. Hussain Shah, R. Ge, W. Zhou, S. Kubuki, J. Wang, Modulation of reaction pathway of Prussian blue analogues derived Zn-Fe double oxides towards organic pollutants oxidation, *Chem. Eng. J.* 454 (2023) 140103, <https://doi.org/10.1016/j.cej.2022.140103>.
- [137] S. Zhang, S. Song, P. Gu, R. Ma, D. Wei, G. Zhao, T. Wen, R. Jehan, B. Hu, X. Wang, Visible-light-driven activation of persulfate over cyano and hydroxyl group co-modified mesoporous g-C₃N₄ for boosting bisphenol A degradation, *J. Mater. Chem. A* 7 (2019) 5552–5560, <https://doi.org/10.1039/C9TA00339H>.
- [138] X. Liu, M. Cui, K. Cui, Y. Ding, X. Chen, C. Chen, X. Nie, Construction of Li/K dopants and cyano defects in graphitic carbon nitride for highly efficient peroxymonosulfate activation towards organic contaminants degradation, *Chemosphere* 294 (2022) 133700, <https://doi.org/10.1016/j.chemosphere.2022.133700>.
- [139] Y. Peng, Q. Zhang, W. Ren, X. Duan, L. Ding, Y. Jing, P. Shao, X. Xiao, X. Luo, Thermodynamic and kinetic behaviors of persulfate-based electron-transfer regime in carbocatalysis, *Environ. Sci. Technol.* (2023), <https://doi.org/10.1021/acs.est.3c02675>.
- [140] W. Ren, L. Xiong, G. Nie, H. Zhang, X. Duan, S. Wang, Insights into the electron-transfer regime of peroxydisulfate activation on carbon nanotubes: The role of oxygen functional groups, *Environ. Sci. Technol.* 54 (2020) 1267–1275, <https://doi.org/10.1021/acs.est.9b06208>.
- [141] W. Ren, L. Xiong, X. Yuan, Z. Yu, H. Zhang, X. Duan, S. Wang, Activation of peroxydisulfate on carbon nanotubes: Electron-transfer mechanism, *Environ. Sci. Technol.* 53 (2019) 14595–14603, <https://doi.org/10.1021/acs.est.9b05475>.
- [142] J. Xiao, Y. Xie, H. Cao, Organic pollutants removal in wastewater by heterogeneous photocatalytic ozonation, *Chemosphere* 121 (2015) 1–17, <https://doi.org/10.1016/j.chemosphere.2014.10.072>.
- [143] J. Xiao, Q. Han, H. Cao, J. Rabeah, J. Yang, Z. Guo, L. Zhou, Y. Xie, A. Brückner, Number of reactive charge carriers-a hidden linker between band structure and catalytic performance in photocatalysts, *ACS Catal.* 9 (2019) 8852–8861, <https://doi.org/10.1021/acscatal.9b02426>.
- [144] Y. Tan, W. Chen, G. Liao, X. Li, J. Wang, Y. Tang, L. Li, Strategy for improving photocatalytic ozonation activity of g-C₃N₄ by halogen doping for water purification, *Appl. Catal. B-Environ.* 306 (2022) 121133, <https://doi.org/10.1016/j.apcatb.2022.121133>.
- [145] C. Zhang, Y. Dong, B. Li, F. Li, Comparative study of three solid oxidants as substitutes of H₂O₂ used in Fe (III)-oxalate complex mediated Fenton system for photocatalytic elimination of reactive azo dye, *J. Clean. Prod.* 177 (2018) 245–253, <https://doi.org/10.1016/j.jclepro.2017.12.211>.
- [146] X. Zhang, B. Xu, S. Wang, X. Li, C. Wang, Y. Xu, R. Zhou, Y. Yu, H. Zheng, P. Yu, Y. Sun, Carbon nitride nanotubes anchored with high-density CuN_x sites for efficient degradation of antibiotic contaminants under photo-Fenton process: Performance and mechanism, *Appl. Catal. B-Environ.* 306 (2022) 121119, <https://doi.org/10.1016/j.apcatb.2022.121119>.
- [147] C. Ding, S. Kang, W. Li, W. Gao, Z. Zhang, L. Zheng, L. Cui, Mesoporous structure and amorphous Fe-N sites regulation in Fe-g-C₃N₄ for boosted visible-light-driven photo-Fenton reaction, *J. Colloid Interface Sci.* 608 (2022) 2515–2528, <https://doi.org/10.1016/j.jcis.2021.10.168>.
- [148] X. Qian, Y. Wu, M. Kan, M. Fang, D. Yue, J. Zeng, Y. Zhao, FeOOH quantum dots coupled g-C₃N₄ for visible light driving photo-Fenton degradation of organic pollutants, *Appl. Catal. B-Environ.* 237 (2018) 513–520, <https://doi.org/10.1016/j.apcatb.2018.05.074>.
- [149] H. Wang, C. Zhang, X. Zhang, S. Wang, Z. Xia, G. Zeng, J. Ding, N. Ren, Construction of Fe₃O₄@ β -CD/g-C₃N₄ nanocomposite catalyst for degradation of PCBs in wastewater through photodegradation and heterogeneous Fenton oxidation, *Chem. Eng. J.* 429 (2022) 132445, <https://doi.org/10.1016/j.cej.2021.132445>.
- [150] S. Mao, C. Liu, Y. Wu, M. Xia, F. Wang, Porous P, Fe-doped g-C₃N₄ nanostructure with enhanced photo-Fenton activity for removal of tetracycline hydrochloride: Mechanism insight, DFT calculation and degradation pathways, *Chemosphere* 291 (2022) 133039, <https://doi.org/10.1016/j.chemosphere.2021.133039>.
- [151] M. Yoon, Y. Oh, S. Hong, J.S. Lee, R. Boppella, S.H. Kim, F.M. Mota, S.O. Kim, D. H. Kim, Synergistically enhanced photocatalytic activity of graphitic carbon nitride and WO₃ nanohybrids mediated by photo-Fenton reaction and H₂O₂, *Appl. Catal. B-Environ.* 206 (2017) 263–270, <https://doi.org/10.1016/j.apcatb.2017.01.038>.
- [152] J. Hu, P. Zhang, W. An, L. Liu, Y. Liang, W. Cui, In-situ Fe-doped g-C₃N₄ heterogeneous catalyst via photocatalysis-Fenton reaction with enriched photocatalytic performance for removal of complex wastewater, *Appl. Catal. B-Environ.* 245 (2019) 130–142, <https://doi.org/10.1016/j.apcatb.2018.12.029>.
- [153] F. Chen, X. Wu, C. Shi, H. Lin, J. Chen, Y. Shi, S. Wang, X. Duan, Molecular engineering toward pyrrolic N-rich M-N₄ (M=Cr, Mn, Fe, Co, Cu) single-atom sites for enhanced heterogeneous Fenton-like reaction, *Adv. Funct. Mater.* 31 (2021) 2007877, <https://doi.org/10.1002/adfm.202007877>.
- [154] S. Liu, D. Liu, Y. Sun, P. Xiao, H. Lin, J. Chen, X. Wu, X. Duan, S. Wang, Enzyme-mimicking single-atom FeN₄ sites for enhanced photo-Fenton-like reactions, *Appl. Catal. B-Environ.* 310 (2022) 121327, <https://doi.org/10.1016/j.apcatb.2022.121327>.
- [155] J. Jiang, X. Wang, Y. Liu, Y. Ma, T. Li, Y. Lin, T. Xie, S. Dong, Photo-Fenton degradation of emerging pollutants over Fe-POM nanoparticle/porous and ultrathin g-C₃N₄ nanosheet with rich nitrogen defect: Degradation mechanism, pathways, and products toxicity assessment, *Appl. Catal. B-Environ.* 278 (2020) 119349, <https://doi.org/10.1016/j.apcatb.2020.119349>.
- [156] H. Lan, F. Wang, M. Lan, X. An, H. Liu, J. Qu, Hydrogen-bond-mediated self-assembly of carbon-nitride-based photo-Fenton-like membranes for wastewater treatment, *Environ. Sci. Technol.* 53 (2019) 6981–6988, <https://doi.org/10.1021/acs.est.9b00790>.
- [157] L. Su, P. Wang, X. Ma, J. Wang, S. Zhan, Regulating local electron density of iron single sites by introducing nitrogen vacancies for efficient photo-Fenton process, *Angew. Chem. Int. Ed.* 60 (2021) 21261–21266, <https://doi.org/10.1002/anie.202108937>.
- [158] Z. Xiong, Z. Wang, M. Muthu, Y. Zhang, Construction of an in-situ Fenton-like system based on a g-C₃N₄ composite photocatalyst, *J. Hazard. Mater.* 373 (2019) 565–571, <https://doi.org/10.1016/j.jhazmat.2019.03.114>.
- [159] W. Shi, W. Sun, Y. Liu, K. Zhang, H. Sun, X. Lin, Y. Hong, F. Guo, A self-sufficient photo-Fenton system with coupling in-situ production H₂O₂ of ultrathin porous g-C₃N₄ nanosheets and amorphous FeOOH quantum dots, *J. Hazard. Mater.* 436 (2022) 129141, <https://doi.org/10.1016/j.jhazmat.2022.129141>.
- [160] Z. Xiong, Y. Zhang, Construction of novel in-situ photo-Fenton system based on modified g-C₃N₄ composite photocatalyst, *Environ. Res.* 195 (2021) 110785, <https://doi.org/10.1016/j.envres.2021.110785>.
- [161] F. Wang, J. Xu, Z. Wang, Y. Lou, C. Pan, Y. Zhu, Unprecedentedly efficient mineralization performance of photocatalysis-self-Fenton system towards organic pollutants over oxygen-doped porous g-C₃N₄ nanosheets, *Appl. Catal. B-Environ.* 312 (2022) 121438, <https://doi.org/10.1016/j.apcatb.2022.121438>.
- [162] K.K. Das, S. Mansingh, R. Mohanty, D.P. Sahoo, N. Priyadarshini, K. Parida, ⁰D-²D Fe₂O₃/boron-doped g-C₃N₄ S-scheme exciton engineering for photocatalytic H₂O₂ production and photo-Fenton recalcitrant-pollutant detoxification: Kinetics, influencing factors, and mechanism, *J. Phys. Chem. C* 127 (2023) 22–40, <https://doi.org/10.1021/acs.jpcc.2c06369>.
- [163] P. Sarkar, S. De, S. Neogi, Microwave assisted facile fabrication of dual Z-scheme g-C₃N₄/ZnFe₂O₄/Bi₂S₃ photocatalyst for peroxymonosulfate mediated

- degradation of 2,4,6-Trichlorophenol: The mechanistic insights, *Appl. Catal. B-Environ.* 307 (2022) 121165, <https://doi.org/10.1016/j.apcatb.2022.121165>.
- [164] S. Kokate, S. Gupta, V.G. Kopuri, H. Prakash, Energy efficient photocatalytic activation of peroxymonosulfate by g-C₃N₄ under 400 nm LED irradiation for degradation of Acid Orange 7, *Chemosphere* 287 (2022) 132099, <https://doi.org/10.1016/j.chemosphere.2021.132099>.
- [165] J. Zhou, W. Liu, W. Cai, The synergistic effect of Ag/AgCl@ZIF-8 modified g-C₃N₄ composite and peroxymonosulfate for the enhanced visible-light photocatalytic degradation of levofloxacin, *Sci. Total Environ.* 696 (2019) 133962, <https://doi.org/10.1016/j.scitotenv.2019.133962>.
- [166] M. Shen, X. Zhang, S. Zhao, Y. Cai, S. Wang, A novel photocatalytic system coupling metal-free carbon/g-C₃N₄ catalyst with persulfate for highly efficient degradation of organic pollutants, *Chemosphere* 314 (2023) 137728, <https://doi.org/10.1016/j.chemosphere.2022.137728>.
- [167] Y. Xu, X. Tang, Y. Xiao, H. Tang, H. Lin, Y. Lv, H. Zhang, Persulfate promoted visible photocatalytic elimination of bisphenol A by g-C₃N₄-CeO₂ S-scheme heterojunction: the dominant role of photo-induced holes, *Chemosphere* 331 (2023) 138765, <https://doi.org/10.1016/j.chemosphere.2023.138765>.
- [168] Y. Song, L. Huang, X. Zhang, H. Zhang, L. Wang, H. Zhang, Y. Liu, Synergistic effect of persulfate and g-C₃N₄ under simulated solar light irradiation: implication for the degradation of sulfamethoxazole, *J. Hazard. Mater.* 393 (2020) 122379, <https://doi.org/10.1016/j.jhazmat.2020.122379>.
- [169] H. Chen, X. Zhang, L. Jiang, X. Yuan, J. Liang, J. Zhang, H. Yu, W. Chu, Z. Wu, H. Li, Y. Li, Strategic combination of nitrogen-doped carbon quantum dots and g-C₃N₄: efficient photocatalytic peroxodisulfate for the degradation of tetracycline hydrochloride and mechanism insight, *Sep. Purif. Technol.* 272 (2021) 118947, <https://doi.org/10.1016/j.seppur.2021.118947>.
- [170] B. Liu, W. Guo, W. Jia, H. Wang, Q. Si, Q. Zhao, H. Luo, J. Jiang, N. Ren, Novel nonradical oxidation of sulfonamide antibiotics with Co(II)-doped g-C₃N₄-activated peracetic acid: role of high-valent cobalt-oxo species, *Environ. Sci. Technol.* 55 (2021) 12640–12651, <https://doi.org/10.1021/acs.est.1c04091>.
- [171] M. Liu, H. Xia, W. Yang, X. Liu, J. Xiang, X. Wang, L. Hu, F. Lu, Novel Cu-Fe bi-metal oxide quantum dots coupled g-C₃N₄ nanosheets with H₂O₂ adsorption-activation trade-off for efficient photo-Fenton catalysis, *Appl. Catal. B-Environ.* 301 (2022) 120765, <https://doi.org/10.1016/j.apcatb.2021.120765>.
- [172] S. Merouani, A. Dehane, A. Belghit, O. Hamdaoui, Y.A. Tobba, C. Lahlou, M. P. Shah, Protonated hydroxylamine-assisted iron catalytic activation of persulfate for the rapid removal of persistent organics from wastewater, *Clean. (Weinh.)* 51 (2023) 2100304, <https://doi.org/10.1002/clen.202100304>.
- [173] Y. Gou, P. Chen, L. Yang, S. Li, L. Peng, S. Song, Y. Xu, Degradation of fluoroquinolones in homogeneous and heterogeneous photo-Fenton processes: a review, *Chemosphere* 270 (2021) 129481, <https://doi.org/10.1016/j.chemosphere.2020.129481>.
- [174] H. Hou, X. Zeng, X. Zhang, Production of hydrogen peroxide by photocatalytic processes, *Angew. Chem. Int. Ed.* 59 (2020) 17356–17376, <https://doi.org/10.1002/anie.201911609>.
- [175] D. Lei, J. Xue, X. Peng, S. Li, Q. Bi, C. Tang, L. Zhang, Oxalate enhanced synergistic removal of chromium(VI) and arsenic(III) over ZnFe₂O₄/g-C₃N₄: Z-scheme charge transfer pathway and photo-Fenton like reaction, *Appl. Catal. B-Environ.* 282 (2021) 119578, <https://doi.org/10.1016/j.apcatb.2020.119578>.
- [176] X. Xu, Y. Sui, W. Chen, W. Huang, X. Li, Y. Li, D. Liu, S. Gao, W. Wu, C. Pan, H. Zhong, H. Wen, M. Wen, The photocatalytic H₂O₂ production by metal-free photocatalysts under visible-light irradiation, *Appl. Catal. B-Environ.* 341 (2024) 123271, <https://doi.org/10.1016/j.apcatb.2023.123271>.
- [177] X. Xu, R. Sa, W. Huang, Y. Sui, W. Chen, G. Zhou, X. Li, Y. Li, H. Zhong, Conjugated organic polymers with anthraquinone redox centers for efficient photocatalytic hydrogen peroxide production from water and oxygen under visible light irradiation without any additives, *ACS Catal.* 12 (2022) 12954–12963, <https://doi.org/10.1021/acscatal.2c04085>.
- [178] X. Xu, H. Zhong, W. Huang, Y. Sui, R. Sa, W. Chen, G. Zhou, X. Li, D. Li, M. Wen, B. Jiang, The construction of conjugated organic polymers containing phenanthrenequinone redox centers for visible-light-driven H₂O₂ production from H₂O and O₂ without any additives, *Chem. Eng. J.* 454 (2023) 139929, <https://doi.org/10.1016/j.cej.2022.139929>.
- [179] X. Xu, K. Xie, J. Hu, S. Liu, H. Zhong, R. Wen, The metal-organic frameworks as unique platform for photocatalytic CO₂ conversion to liquid fuels, *J. Environ. Chem. Eng.* 11 (2023) 110424, <https://doi.org/10.1016/j.jece.2023.110424>.
- [180] L. Chen, C. Chen, Z. Yang, S. Li, C. Chu, B. Chen, Simultaneously tuning band structure and oxygen reduction pathway toward high-efficient photocatalytic hydrogen peroxide production using cyano-rich graphitic carbon nitride, *Adv. Funct. Mater.* 31 (2021) 2105731, <https://doi.org/10.1002/adfm.202105731>.
- [181] L. Zhou, J. Feng, B. Qiu, Y. Zhou, J. Lei, M. Xing, L. Wang, Y. Zhou, Y. Liu, J. Zhang, Ultrathin g-C₃N₄ nanosheet with hierarchical pores and desirable energy band for highly efficient H₂O₂ production, *Appl. Catal. B-Environ.* 267 (2020) 118396, <https://doi.org/10.1016/j.apcatb.2019.118396>.
- [182] X. Zhao, Y. You, S. Huang, Y. Wu, Y. Ma, G. Zhang, Z. Zhang, Z-scheme photocatalytic production of hydrogen peroxide over Bi₄O₃Br₂/g-C₃N₄ heterostructure under visible light, *Appl. Catal. B-Environ.* 278 (2020) 119251, <https://doi.org/10.1016/j.apcatb.2020.119251>.
- [183] X. Wang, W. Lu, Z. Zhao, H. Zhong, Z. Zhu, W. Chen, In situ stable growth of β-FeOOH on g-C₃N₄ for deep oxidation of emerging contaminants by photocatalytic activation of peroxymonosulfate under solar irradiation, *Chem. Eng. J.* 400 (2021) 125872, <https://doi.org/10.1016/j.cej.2020.125872>.
- [184] H. Shao, X. Zhao, Y. Wang, R. Mao, Y. Wang, M. Qiao, S. Zhao, Y. Zhu, Synergistic activation of peroxymonosulfate by Co₃O₄ modified g-C₃N₄ for enhanced degradation of diclofenac sodium under visible light irradiation, *Appl. Catal. B-Environ.* 218 (2017) 810–818, <https://doi.org/10.1016/j.apcatb.2017.07.016>.
- [185] G. Zhao, W. Li, H. Zhang, W. Wang, Y. Ren, Single atom Fe-dispersed graphitic carbon nitride (g-C₃N₄) as a highly efficient peroxymonosulfate photocatalytic activator for sulfamethoxazole degradation, *Chem. Eng. J.* 430 (2022) 132937, <https://doi.org/10.1016/j.cej.2021.132937>.
- [186] X. Ao, J. Eloranta, C. Huang, D. Santoro, W. Sun, Z. Lu, C. Li, Peracetic acid-based advanced oxidation processes for decontamination and disinfection of water: a review, *Water Res.* 188 (2021) 116479, <https://doi.org/10.1016/j.watres.2020.116479>.
- [187] J. Kim, T. Zhang, W. Liu, P. Du, J.T. Dobson, C. Huang, Advanced oxidation process with peracetic acid and Fe(II) for contaminant degradation, *Environ. Sci. Technol.* 53 (2019) 13312–13322, <https://doi.org/10.1021/acs.est.9b02991>.
- [188] K. Zhu, X. Chen, C. Yuan, C. Bai, Y. Sun, B. Zhang, F. Chen, Orientated construction of visible-light-assisted peroxymonosulfate activation system for antibiotic removal: Significant enhancing effect of Cl⁻, *J. Hazard. Mater.* 445 (2023) 130476, <https://doi.org/10.1016/j.jhazmat.2022.130476>.
- [189] F. Wu, H. Huang, T. Xu, W. Lu, N. Li, W. Chen, Visible-light-assisted peroxymonosulfate activation and mechanism for the degradation of pharmaceuticals over pyridyl-functionalized graphitic carbon nitride coordinated with iron phthalocyanine, *Appl. Catal. B-Environ.* 218 (2017) 230–239, <https://doi.org/10.1016/j.apcatb.2017.06.057>.
- [190] Y. Liu, H. Guo, M. Yu, C. Shen, A. Xu, Structure-dependent surface molecule-modified semiconductor photocatalysts: recent progress and future challenges, *ACS Sustain. Chem. Eng.* 10 (2022) 16476–16502, <https://doi.org/10.1021/acssuschemeng.2c05634>.
- [191] H. Agbe, E. Nyankson, N. Raza, D. Dodo-Arhin, A. Chauhan, G. Osei, V. Kumar, K. Kim, Recent advances in photoinduced catalysis for water splitting and environmental applications, *J. Ind. Eng. Chem.* 72 (2019) 31–49, <https://doi.org/10.1016/j.jiec.2019.01.004>.
- [192] J. Willkomm, K. Orchard, A. Reynal, E. Pastor, J. Durrant, E. Reisner, Dye-sensitised semiconductors modified with molecular catalysts for light-driven H₂ production, *Chem. Soc. Rev.* 45 (2016) 9–23, <https://doi.org/10.1039/C5CS00733J>.
- [193] W. Wang, Q. Niu, G. Zeng, C. Zhang, D. Huang, B. Shao, C. Zhou, Y. Yang, Y. Liu, H. Guo, W. Xiong, L. Lei, S. Liu, H. Yi, S. Chen, X. Tang, 1D porous tubular g-C₃N₄ capture black phosphorus quantum dots as 1D/0D metal-free photocatalysts for oxytetracycline hydrochloride degradation and hexavalent chromium reduction, *Appl. Catal. B-Environ.* 273 (2020) 119051, <https://doi.org/10.1016/j.apcatb.2020.119051>.
- [194] A. Wang, S. Guo, Z. Zheng, H. Wang, X. Song, H. Zhu, Y. Zeng, J. Lam, R. Qiu, K. Yan, Highly dispersed Ag and g-C₃N₄ quantum dots co-decorated 3D hierarchical Fe₃O₄ hollow microspheres for solar-light-driven pharmaceutical pollutants degradation in natural water matrix, *J. Hazard. Mater.* 434 (2022) 128905, <https://doi.org/10.1016/j.jhazmat.2022.128905>.
- [195] F. Wang, Y. Wu, Y. Wang, J. Li, X. Jin, Q. Zhang, R. Li, S. Yan, H. Liu, Y. Feng, G. Liu, W. Lv, Construction of novel Z-scheme nitrogen-doped carbon dots/{001} TiO₂ nanosheet photocatalysts for broad-spectrum-driven diclofenac degradation: Mechanism insight, products and effects of natural water matrices, *Chem. Eng. J.* 356 (2019) 857–868, <https://doi.org/10.1016/j.cej.2018.09.092>.
- [196] H. Gao, H. Yang, J. Xu, S. Zhang, J. Li, Strongly coupled g-C₃N₄ nanosheets-Co₃O₄ quantum dots as 2D/0D heterostructure composite for peroxymonosulfate activation, *Small* 14 (2018) 1801353, <https://doi.org/10.1002/sml.201801353>.
- [197] X. Wang, X. Zhang, Y. Zhang, Y. Wang, S. Sun, W. Wu, Z. Wu, Nanostructured semiconductor supported iron catalysts for heterogeneous photo-Fenton oxidation: a review, *J. Mater. Chem. A* 8 (2020) 15513–15546, <http://10.1039/D0TA04541A>.
- [198] J. Xi, H. Xia, X. Ning, Z. Zhang, J. Liu, Z. Mu, S. Zhang, P. Du, X. Lu, Carbon-intercalated 0D/2D hybrid of hematite quantum dots/graphitic carbon nitride nanosheets as superior catalyst for advanced oxidation, *Small* 15 (2019) 1902744, <https://doi.org/10.1002/sml.201902744>.
- [199] Q. Zhang, Y. Peng, Y. Lin, S. Wu, X. Yu, C. Yang, Bisphenol S-doped g-C₃N₄ nanosheets modified by boron nitride quantum dots as efficient visible-light-driven photocatalysts for degradation of sulfamethazine, *Chem. Eng. J.* 405 (2021) 126661, <https://doi.org/10.1016/j.cej.2020.126661>.
- [200] Y. Li, Y. Si, B. Zhou, T. Huang, W. Huang, W. Hu, A. Pan, X. Fan, G. Huang, Interfacial charge modulation: carbon quantum dot implanted carbon nitride double-deck nanoframes for robust visible-light photocatalytic tetracycline degradation, *Nanoscale* 12 (2020) 3135–3145, <https://doi.org/10.1039/C9NR09945J>.
- [201] M. Michalska, V. Matejka, J. Pavlovský, P. Praus, M. Ritz, J. Serenčíšová, L. Gembláková, M. Kormunda, K. Foniok, M. Reli, G. Simha Martynková, Effect of Ag modification on TiO₂ and melem/g-C₃N₄ composite on photocatalytic performances, *Sci. Rep.* 13 (2023) 5270, <https://doi.org/10.1038/s41598-023-32094-6>.
- [202] B. Gholipour, A. Zonouzi, M. Shokouhimehr, S. Rostamnia, Integration of plasmonic AgPd alloy nanoparticles with single-layer graphitic carbon nitride as Mott-Schottky junction toward photo-promoted H₂ evolution, *Sci. Rep.* 12 (2022) 13583, <https://doi.org/10.1038/s41598-022-17238-4>.
- [203] Q. Wang, K. Domen, Particulate photocatalysts for light-driven water splitting: mechanisms, challenges, and design strategies, *Chem. Rev.* 120 (2020) 919–985, <https://doi.org/10.1021/acs.chemrev.9b00201>.
- [204] D.B. Ingram, S. Linic, Water splitting on composite plasmonic-metal/semiconductor photoelectrodes: evidence for selective plasmon-induced formation of charge carriers near the semiconductor surface, *J. Am. Chem. Soc.* 133 (2011) 5202–5205, <https://doi.org/10.1021/ja200086g>.

- [205] Y. Wang, X. Zhao, D. Cao, Y. Wang, Y. Zhu, Peroxymonosulfate enhanced visible light photocatalytic degradation bisphenol A by single-atom dispersed Ag mesoporous g-C₃N₄ hybrid, *Appl. Catal. B-Environ.* 211 (2017) 79–88, <https://doi.org/10.1016/j.apcatb.2017.03.079>.
- [206] L. Zhou, Z. Liu, Z. Guan, B. Tian, L. Wang, Y. Zhou, Y. Zhou, J. Lei, J. Zhang, Y. Liu, 0D/2D plasmonic Cu_{2-x}S/g-C₃N₄ nanosheets harnessing UV–vis–NIR broad spectrum for photocatalytic degradation of antibiotic pollutant, *Appl. Catal. B-Environ.* 263 (2020) 118326, <https://doi.org/10.1016/j.apcatb.2019.118326>.
- [207] Y. Zhang, W. Chu, G-C₃N₄ induced acceleration of Fe³⁺/Fe²⁺ cycles for enhancing metronidazole degradation in Fe³⁺/peroxymonosulfate process under visible light, *Chemosphere* 293 (2022) 133611, <https://doi.org/10.1016/j.chemosphere.2022.133611>.
- [208] X. Li, Y. Pi, L. Wu, Q. Xia, J. Wu, Z. Li, J. Xiao, Facilitation of the visible light-induced Fenton-like excitation of H₂O₂ via heterojunction of g-C₃N₄/NH₂-iron terephthalate metal-organic framework for MB degradation, *Appl. Catal. B-Environ.* 202 (2017) 653–663, <https://doi.org/10.1016/j.apcatb.2016.09.073>.
- [209] G. Zhang, G. Kim, W. Choi, Visible light driven photocatalysis mediated via ligand-to-metal charge transfer (LMCT): an alternative approach to solar activation of titania, *Energy Environ. Sci.* 7 (2014) 954–966, <https://doi.org/10.1039/C3EE43147A>.
- [210] Y. Li, Implementing metal-to-ligand charge transfer in organic semiconductor for improved visible-near-infrared photocatalysis, *Adv. Mater.* 28 (2016) 6959–6965, <https://doi.org/10.1002/adma.201601960>.
- [211] W. Miao, Y. Liu, X. Chen, Y. Zhao, S. Mao, Tuning layered Fe-doped g-C₃N₄ structure through pyrolysis for enhanced Fenton and photo-Fenton activities, *Carbon* 159 (2020) 461–470, <https://doi.org/10.1016/j.carbon.2019.12.056>.
- [212] N. Klammer, S. Malato, A. Agüera, A. Fernández Alba, G. Mailhot, Treatment of municipal wastewater treatment plant effluents with modified photo-Fenton as a tertiary treatment for the degradation of micro pollutants and disinfection, *Environ. Sci. Technol.* 46 (2012) 2885–2892, <https://doi.org/10.1021/es204112d>.
- [213] Z. Ye, I. Sirés, H. Zhang, Y. Huang, Mineralization of pentachlorophenol by ferrioxalate-assisted solar photo-Fenton process at mild pH, *Chemosphere* 217 (2019) 475–482, <https://doi.org/10.1016/j.chemosphere.2018.10.221>.
- [214] A.V. Vorontsov, Advancing Fenton and photo-Fenton water treatment through the catalyst design, *J. Hazard. Mater.* 372 (2019) 103–112, <https://doi.org/10.1016/j.jhazmat.2018.04.033>.
- [215] L. Yang, X. Bai, J. Shi, X. Du, L. Xu, P. Jin, Quasi-full-visible-light absorption by D35-TiO₂/g-C₃N₄ for synergistic persulfate activation towards efficient photodegradation of micropollutants, *Appl. Catal. B-Environ.* 256 (2019) 117759, <https://doi.org/10.1016/j.apcatb.2019.117759>.
- [216] L. Dong, T. Xu, W. Chen, W. Lu, Synergistic multiple active species for the photocatalytic degradation of contaminants by imidazole-modified g-C₃N₄ coordination with iron phthalocyanine in the presence of peroxymonosulfate, *Chem. Eng. J.* 357 (2019) 198–208, <https://doi.org/10.1016/j.cej.2018.09.094>.
- [217] Y. Deng, J. Liu, Y. Huang, M. Ma, K. Liu, X. Dou, Z. Wang, S. Qu, Z. Wang, Engineering the photocatalytic behaviors of g-C₃N₄-based metal-free materials for degradation of a representative antibiotic, *Adv. Funct. Mater.* 30 (2020) 2002353, <https://doi.org/10.1002/adfm.202002353>.
- [218] Y. Tian, N. Jia, H. Ma, G. Liu, Z. Xiao, Y. Wu, L. Zhou, J. Lei, L. Wang, Y. Liu, J. Zhang, 0D/3D coupling of g-C₃N₄ QDs/hierarchical macro-mesoporous CuO-SiO₂ for high-efficiency norfloxacin removal in photo-Fenton-like processes, *J. Hazard. Mater.* 419 (2021) 126359, <https://doi.org/10.1016/j.jhazmat.2021.126359>.
- [219] X. Liu, J. Wang, D. Wu, Z. Wang, Y. Li, X. Fan, F. Zhang, G. Zhang, W. Peng, N-doped carbon dots decorated 3D g-C₃N₄ for visible-light driven peroxydisulfate activation: Insights of non-radical route induced by Na⁺ doping, *Appl. Catal. B-Environ.* 310 (2022) 121304, <https://doi.org/10.1016/j.apcatb.2022.121304>.
- [220] J. Cai, J. Huang, S. Wang, J. Iocozzia, Z. Sun, J. Sun, Y. Yang, Y. Lai, Z. Lin, Crafting mussel-inspired metal nanoparticle-decorated ultrathin graphitic carbon nitride for the degradation of chemical pollutants and production of chemical resources, *Adv. Mater.* 31 (2019) 1806314, <https://doi.org/10.1002/adma.201806314>.
- [221] M. Zhang, C. Lai, F. Xu, D. Huang, T. Hu, B. Li, D. Ma, S. Liu, Y. Fu, L. Li, L. Tang, L. Chen, Ultrahigh performance H₂O₂ generation by single-atom Fe catalysts with N/O bidentate ligand via oxalic acid and oxygen molecules activation, *Small* 19 (2023) 2301817, <https://doi.org/10.1002/smll.202301817>.
- [222] Y. Li, Y. Fang, Z. Cao, N. Li, D. Chen, Q. Xu, J. Lu, Construction of g-C₃N₄/PDI@MOF heterojunctions for the highly efficient visible light-driven degradation of pharmaceutical and phenolic micropollutants, *Appl. Catal. B-Environ.* 250 (2019) 150–162, <https://doi.org/10.1016/j.apcatb.2019.03.024>.